

ELF/VLF WAVE GENERATION BY MODULATED HF HEATING  
OF THE AURORAL ELECTROJET

A DISSERTATION  
SUBMITTED TO THE DEPARTMENT OF ELECTRICAL  
ENGINEERING  
AND THE COMMITTEE ON GRADUATE STUDIES  
OF STANFORD UNIVERSITY  
IN PARTIAL FULFILLMENT OF THE REQUIREMENTS  
FOR THE DEGREE OF  
DOCTOR OF PHILOSOPHY

Robert C. Moore

March 2007

© Copyright by Robert C. Moore 2007  
All Rights Reserved

I certify that I have read this dissertation and that, in my opinion, it is fully adequate in scope and quality as a dissertation for the degree of Doctor of Philosophy.

---

(Umran S. Inan) Principal Adviser

I certify that I have read this dissertation and that, in my opinion, it is fully adequate in scope and quality as a dissertation for the degree of Doctor of Philosophy.

---

(Timothy F. Bell)

I certify that I have read this dissertation and that, in my opinion, it is fully adequate in scope and quality as a dissertation for the degree of Doctor of Philosophy.

---

(Antony C. Fraser-Smith)

Approved for the University Committee on Graduate Studies.

*This dissertation is dedicated to my mother and father  
Pat and Tom  
and to my wife  
Minja*

# Abstract

The generation of electromagnetic waves in the Extremely Low Frequency (ELF, 3-3000 Hz) and Very Low Frequency (VLF, 3-30 kHz) bands by modulated High Frequency (HF, 3-30 MHz) heating of the auroral electrojet current system is investigated experimentally, and observations are compared against the predictions of a theoretical model.

Experimental evidence is presented to demonstrate the regular occurrence of ELF/VLF amplitude saturation as a function of peak HF power level. The observed ELF/VLF amplitude saturation is examined as a function of modulation frequency and as a function of time of day. For modulation depths less than 100%, the dependence of ELF/VLF amplitude on average HF power is investigated, yielding an optimal average HF power level which maximizes the observed ELF/VLF amplitude. Observations of ELF/VLF amplitude saturation under a large range of geomagnetic conditions indicate that the identified saturation process occurs on a regular basis. Furthermore, observations indicate that the spatial distribution of the modulated ionospheric conductivity can be remotely sensed using ground based measurements of the horizontal component of the generated ELF/VLF magnetic flux density.

Each of these experimental observations is interpreted in the context of an HF heating model which accounts for the Earth's magnetic field and for the altitudinal variation of several ionospheric constituents. This model indicates that the variation in ELF/VLF amplitude at low HF power levels is dominated by the HF self-absorption process, whereas the variation in ELF/VLF amplitude at high HF power levels results from the competition between the electron energy losses associated with the rotational excitation of molecular nitrogen and the vibrational excitation of molecular oxygen.

# Acknowledgements

It has been an honor to work as a graduate student and research assistant with the VLF group in the STAR Laboratory of Stanford University for the last eight years.

I would like to thank my advisor, Professor Umran Inan, for his guidance and encouragement during the course of this research. I am particularly grateful to him for the breadth of research projects to which I have been exposed over the last eight years. I would also like to thank Dr. Timothy Bell, who has proven to be very helpful during many late-night discussions regarding ionospheric heating. I am grateful to Professor Antony Fraser-Smith for providing sage advice, entertaining conversation, and the occasional opportunity for travel. I would especially like to thank Professor John Pauly for chairing my oral defense session.

I would like to express my appreciation for the VLF group staff who have enriched my experience at Stanford over the years. Bill Trabucco taught me how to assemble and deploy VLF receivers, and Jerry Yarbrough taught me how to interpret the data. Both provided many interesting stories along with pearls of wisdom prior to their retirement. Shaolan Min and Helen Niu have always helped me deal with the most important aspect of the job: reimbursement. Shaolan especially has helped to make my life easier on a number of stressful occasions.

Graduate students, past and present, have also contributed to this work. The installation of ELF/VLF receiver site at the Chistochina B&B in Chistochina, Alaska, could not have taken place without Tim Chevalier, Dr. Mike Chevalier, and Dr. Troy Wood. Ben Cotts, Morris Cohen, Mark Golkowski, and Dan Golden have kept the site running successfully over the years. Of course, the owners of the Chistochina B&B, Norma and Doyle Traw, always kept my belly full while on deployment to Alaska.

The operation of this flagship receiver site, the data from which is extensively used throughout this dissertation, would not have been possible without their enthusiastic support.

Dr. Nikolai Lehtinen, Joseph Payne, Ryan Said, and Charlie Wang have each helped with my interpretation of ionospheric HF heating over the course of many discussions, and I thank them for this fruitful interaction.

In addition to the members of the VLF group, the operators of the HAARP facility deserve credit for operating sometimes continuously around the clock for our experiments: Mike McCarrick, Helio Zwi, Dave Seafolk-Kopp, and Marty Karjala.

This work would not have been possible without the love and support of my parents, whom I love very dearly. My family, Tom and Lynnelle, Mike and Cynth, Steve and Laurie, Dave and Kim, and Lisa and Tom, stood beside me each step of the way, poking fun when needed and reminding me that there is still a ‘real’ world beyond the confines of the Packard Building basement. Scott and Michelle Robertson, two very close friends, have also always been there when I needed them.

My wife, Minja, has tolerated my strange working hours and has cared for me lovingly since the day we met. I could not have completed this process without her by my side. One simple paragraph cannot fully express my love and gratitude. Of course, the completion of this dissertation was greatly accelerated by the arrival of our son, Nikolas, who is arguably the most adorable baby boy in the whole wide world.

ROBB MOORE

*Stanford, California*

*March 20, 2007*

This work was supported by the High-frequency Active Auroral Research Program (HAARP), the Air Force Research Laboratory (AFRL), the Defense Advanced Research Programs Agency (DARPA), and the Office of Naval Research (ONR) via ONR grants N00014-00-1-0643, N00014-05-C-0308, and N00014-03-1-0630 to Stanford University.

# Contents

<b>Abstract</b>	<b>v</b>
<b>Acknowledgements</b>	<b>vi</b>
<b>1 Introduction</b>	<b>1</b>
1.1 Previous Observations of HF Heater-Induced ELF/VLF Waves . . . . .	2
1.1.1 Tromsø, Norway . . . . .	2
1.1.2 Arecibo, Puerto Rico . . . . .	4
1.1.3 HIPAS, Alaska . . . . .	5
1.1.4 HAARP, Alaska . . . . .	6
1.2 ELF/VLF Amplitude Dependence on HF Power . . . . .	7
1.3 Scientific Contributions . . . . .	12
<b>2 ELF/VLF Wave Generation Physics and the HF Heating Model</b>	<b>13</b>
2.1 General Overview . . . . .	13
2.2 Electron Temperature Modulation . . . . .	19
2.2.1 HF Ray Tracing . . . . .	22
2.2.2 HF Self-Absorption . . . . .	26
2.2.3 Ionospheric Recovery: Electron Energy Loss Rates . . . . .	28
2.3 Modulated Ionospheric Conductivity . . . . .	34
2.4 ELF/VLF Wave Generation . . . . .	37
<b>3 ELF/VLF Amplitude Saturation</b>	<b>40</b>
3.1 Description of the Experiment . . . . .	41

3.2	ELF/VLF Amplitude Saturation at 1225 Hz . . . . .	43
3.2.1	Experimental Observations . . . . .	43
3.2.2	Hard-Cap Approximation . . . . .	45
3.2.3	Extraction of the Saturation Function . . . . .	47
3.3	Average Saturation Levels . . . . .	50
3.4	Comparison with HF Heating Model . . . . .	53
3.4.1	The First Harmonic Amplitude . . . . .	55
3.4.2	The Second Harmonic Amplitude . . . . .	58
3.4.3	The Third Harmonic Amplitude . . . . .	61
<b>4</b>	<b>An Optimal HF Power Level (&lt;100% Modulation Depth)</b>	<b>65</b>
4.1	Description of the Experiment . . . . .	66
4.2	Experimental Observations . . . . .	67
4.3	Comparison with Full HF Heating Model . . . . .	72
<b>5</b>	<b>Statistical Analysis of ELF/VLF Amplitude Saturation</b>	<b>79</b>
5.1	Description of the Long-Term Experiments . . . . .	79
5.2	Occurrence of ELF/VLF Amplitude Saturation . . . . .	85
5.3	Spatial Distribution of the Source Region . . . . .	89
<b>6</b>	<b>Summary and Suggestions for Future Work</b>	<b>96</b>
6.1	Summary of Contributions . . . . .	96
6.2	Suggestions for Future Research . . . . .	98
6.2.1	Experiment: Same HF Beamwidth, Higher HF Power . . . . .	98
6.2.2	Experiment: Optimal HF Power versus HF Frequency . . . . .	99
6.2.3	Experiment: Saturation versus HF Beam Direction . . . . .	99

# List of Tables

2.1	HAARP parameters versus HF frequency . . . . .	24
5.1	March 2002: 1225 Hz amplitude statistics at Chistochina . . . . .	86
5.2	March 2002: 1225 Hz amplitude statistics at Crosswind Lake . . . . .	86
5.3	November 2002: 1225 Hz amplitude statistics at Chistochina . . . . .	89
5.4	November 2002: 1225 Hz amplitude statistics at Valdez . . . . .	89

# List of Figures

1.1	Sample HF transmission sequences for the power-step and constant modulation-depth experiments . . . . .	8
1.2	Power-dependent ELF/VLF wave generation at Tromsø . . . . .	9
1.3	Power-step experiment at Arecibo . . . . .	10
1.4	Power-law dependence of ELF/VLF amplitude on HF power (Tromsø)	11
2.1	Cartoon: Summary of ELF/VLF wave generation process . . . . .	14
2.2	Cartoon: HF self-absorption as a function of time and HF power level	28
2.3	Electron energy loss rates . . . . .	31
2.4	Cartoon: Temperature modulation and electron energy loss rates . . .	32
2.5	Model electron temperature variations . . . . .	34
2.6	Conductivity versus electron temperature . . . . .	37
3.1	HAARP transmission schedule for the power-step experiment. . . . .	42
3.2	Power-step observations for 1225 Hz modulation on 2 August 2004 . .	44
3.3	Average amplitude variations at 1225 Hz and harmonics . . . . .	45
3.4	Simple modeling: power-law versus hard-cap saturation . . . . .	47
3.5	Empirically-derived saturation function and application . . . . .	48
3.6	Modeling results: power-law versus empirical saturation function . . .	49
3.7	Average saturation functions . . . . .	51
3.8	Hall and Pedersen conductivity amplitude versus altitude . . . . .	52
3.9	Matching Hall and Pedersen conductivity variations with HF power .	54
3.10	Comparison of power-law variations with modeled Hall and Pedersen conductivity variations . . . . .	55

3.11	First harmonic: self-absorption versus loss rates . . . . .	56
3.12	First harmonic: dependence on loss rates . . . . .	57
3.13	Second harmonic: self-absorption versus loss rates . . . . .	59
3.14	Second harmonic: dependence on loss rates . . . . .	61
3.15	Third harmonic: self-absorption versus loss rates . . . . .	62
3.16	Third harmonic: dependence on loss rates . . . . .	63
4.1	Transmission schedule: constant modulation depth experiment . . . . .	66
4.2	Chistochina: 50% modulation depth, square-wave AM transmissions . . . . .	67
4.3	Constant modulation depth: Average ELF/VLF amplitude . . . . .	68
4.4	North-South amplitude versus average HF power . . . . .	69
4.5	East-West amplitude versus average HF power . . . . .	71
4.6	Hall and Pedersen conductivity modulation versus altitude . . . . .	73
4.7	Hall and Pedersen amplitude variations with average HF power . . . . .	74
4.8	Constant modulation depth: self-absorption versus loss rates . . . . .	76
4.9	Constant modulation depth: dependence on loss rates . . . . .	77
5.1	ELF/VLF receiver map: March and November 2002 . . . . .	80
5.2	HF heating at 75 km in relation to ground-based ELF/VLF receivers . . . . .	81
5.3	The ‘standard’ modulation frequency-time transmission format . . . . .	82
5.4	Natural activity at Chistochina and Crosswind Lake . . . . .	83
5.5	Example: Large-amplitude ELF/VLF signal generation . . . . .	84
5.6	Dominant HF beam directions: second-to-first harmonic ratio . . . . .	93
5.7	Cartoon: Saturation dependence on source location . . . . .	94
5.8	Spatial HF heating effects . . . . .	95

# Chapter 1

## Introduction

This dissertation addresses the generation of electromagnetic waves in the Extremely Low Frequency (ELF, 3-3000 Hz) and the Very Low Frequency (VLF, 3-30 kHz) bands by the nonlinear demodulation of High Frequency (HF, 3-30 MHz) signals propagating in the ionosphere in the presence of the auroral electrojet current system. The observations presented herein are limited to the  $\sim 1$ -5 kHz range, which, for the purposes of this work, we refer to as the ELF/VLF band since there is significant overlap into both frequency regimes.

The purposes of Stanford University research with the High-frequency Active Auroral Research Program (HAARP) ionospheric heater in Alaska in the field of ELF/VLF wave generation include: 1) to inject ELF/VLF waves into near-Earth space to probe the Earth's magnetosphere and radiation belts and to investigate ELF/VLF wave-particle interactions therein, 2) to excite ELF/VLF signals in the Earth-ionosphere waveguide for the remote-sensing of the *D*- and *E*-regions of the ionosphere, and 3) to probe the nonlinear aspects of the HF heating processes by which the ELF/VLF signals are created. This dissertation is concerned primarily with the third purpose: the detection and assessment of the nonlinear ionospheric heating processes involved in the creation of ELF/VLF waves. This introductory chapter places the contributions of this dissertation in the context of previous ELF/VLF wave generation studies, with a particular emphasis on the ELF/VLF amplitude dependence on HF power level.

## 1.1 Previous Observations of HF Heater-Induced ELF/VLF Waves

Modulated heating of the *D*-region ionosphere in the presence of high-altitude, naturally-forming electric currents, such as the auroral electrojet and mid-latitude dynamo currents, has been investigated since the 1970's as a means for the generation of electromagnetic waves in the ELF/VLF band [e.g., *Getmantsev et al.*, 1974; *Stubbe et al.*, 1982; *Ferraro et al.*, 1984; *Barr et al.*, 1991; *Villaseñor et al.*, 1996; *Papadopoulos et al.*, 2003; *Moore et al.*, 2007]. Periodic heating of the ionospheric region through which these currents flow with an HF transmitter modulates the conductivity of the region and, in turn, modulates these naturally-forming (and pre-existing) currents, constituting what amounts to a giant radiating antenna at  $\sim 60$ -100 km altitude. ELF/VLF waves artificially produced in this manner have been studied extensively at high power HF ionospheric heating facilities, such as the Tromsø, Arecibo, HIPAS, and HAARP observatories, the major results of which are discussed below.

### 1.1.1 Tromsø, Norway

The Tromsø HF ionospheric heating facility in Norway successfully produced electromagnetic waves using HF heating in the frequency range of 2.7-8.0 MHz [*Barr and Stubbe*, 1991a]. ELF/VLF signals were typically produced using square-wave amplitude modulation in the 200 Hz to 6.5 kHz frequency band and detected with amplitudes of  $\sim 1$  pT,  $\sim 0.1$  pT, and  $\sim 0.03$  pT, as measured on the ground at receiver distances of  $\sim 20$  km,  $\sim 200$  km and  $\sim 500$  km, respectively, from the HF transmitter [*Stubbe et al.*, 1982; *Barr et al.*, 1985]. Subsequent experiments successfully excited the Earth-ionosphere waveguide and, on several occasions, ELF/VLF waves of magnitude  $\sim 10$  femtotesla (fT,  $10^{-15}$  Tesla) were detected at more than 2000 km ground distance from the HF transmitter [*Barr et al.*, 1991].

At close distances (e.g.,  $\leq \sim 100$  km), the observed ELF/VLF amplitudes exhibited pronounced local (in frequency) maxima at and near multiples of  $\sim 2$  kHz dropping off by  $\sim 3$  dB at the lower end of the frequency range (i.e.,  $< 1$  kHz) [*Stubbe et al.*, 1982].

These pronounced peaks at multiples of 2 kHz were shown to result dominantly from Earth-ionosphere waveguide resonance effects [Stubbe *et al.*, 1982; Barr and Stubbe, 1984a; Rietveld *et al.*, 1989], although modeling results have not yet satisfactorily reproduced observed amplitude variations below  $\sim 500$  Hz [Rietveld and Stubbe, 2006]. At greater ground distances (i.e.,  $>500$  km), pronounced Earth-ionosphere waveguide effects, such as those associated with the first quasi-transverse electric (QTE) waveguide mode cutoff frequency, were readily observed in experimental data [Barr *et al.*, 1986].

The variations in ELF/VLF signal amplitude (as a function of time) have been correlated with geomagnetic activity, as assessed by the  $K_p$  index [Barr *et al.*, 1985]. ELF/VLF waves generated using X-mode polarization were typically more than 3 dB higher in amplitude than those generated using O-mode polarization, as measured both on the ground [Stubbe *et al.*, 1982; Barr *et al.*, 1999] and in space [James *et al.*, 1984]. Rietveld *et al.* [1983] compared measurements of the electrojet electric field with observations of ELF/VLF wave polarizations to show that the radiating element dominating Earth-ionosphere waveguide excitation was perpendicular to the driving electric field. Based on these observations, they concluded that the so-called Hall current dominates ground-based ELF/VLF observations. In order to fully explain the observed ELF/VLF wave polarizations, however, the received ELF/VLF signals were interpreted as the result of effective (height-integrated) Hall and Pedersen dipoles excited out of phase and radiating from different effective altitudes above the HF heating array [Stubbe *et al.*, 1977; Barr and Stubbe, 1984b,a; James *et al.*, 1984; James, 1985; Barr *et al.*, 1985; Rietveld *et al.*, 1986].

Measurements at locations distant from the HF transmitter were used to evaluate the ELF/VLF power radiated from the ionosphere. Far-field, ground-based observations within the Earth-ionosphere waveguide were consistent with a  $\sim 1$  Watt ELF/VLF source dipole located at the altitude of the maximum Hall conductivity modulation [Barr *et al.*, 1985]. On the other hand, space-based measurements were consistent with a  $\sim 30$  Watt ELF/VLF source dipole [James *et al.*, 1990]. Simultaneous measurements on the ground and in space on the Akebono (EXOS-D) satellite [Kimura *et al.*, 1994] observed different ELF/VLF source characteristics for the

ground-based and the space-based observations, indicating the possibility that different portions of the HF-heated region dominate the excitation of the Earth-ionosphere waveguide and the excitation of waves propagating upward to space. Investigation of the relationship between the ELF/VLF power radiated into space and that radiated into the Earth-ionosphere waveguide is an active current area of research [e.g, see *Platino et al.*, 2006].

### 1.1.2 Arecibo, Puerto Rico

Several ELF/VLF wave generation experiments have been performed at the Arecibo Observatory, in Puerto Rico, where the equatorial dynamo current is the naturally-forming current system to be modulated by HF heating. During these experiments, ELF/VLF waves were produced over the frequency range of 500 Hz to 5 kHz using a heater frequency of approximately 3 MHz and a total HF input power of 800 kW [*Ferraro et al.*, 1982]. The ELF/VLF signal amplitude at 2688 Hz was used to corroborate the fact that X-mode heating typically generated stronger ELF/VLF signal radiation than O-mode heating [*Ferraro et al.*, 1984]. *Ferraro et al.* [1984] also investigated the dependence of ELF/VLF amplitude on the duty cycle of the square-wave modulation employed. Results indicated that the ionospheric heating/cooling timescales affected the received amplitude as a function of duty cycle, and that a 48% duty cycle maximized ELF/VLF radiation efficiency [*Ferraro et al.*, 1984]. Although a 48% duty cycle was shown to maximize the ELF/VLF radiation efficiency, *Ferraro et al.* [1984] did not take the next step and quantify the ionospheric heating and cooling rates dominating the production of the observed ELF/VLF wave. This experiment was repeated at Tromsø for a number of modulation frequencies by *Barr and Stubbe* [1991b], who, unlike *Ferraro et al.* [1984], quantified the ionospheric heating and cooling timescales based on their observations at multiple modulation frequencies. Lastly, *Tomko* [1981] found that the generated ELF/VLF signal amplitude was largest during nighttime and decreased as noon approached, a diurnal variation opposite to that observed by *Getmantsev et al.* [1974].

### 1.1.3 HIPAS, Alaska

At the High-Power Auroral Stimulation (HIPAS) HF heater facility near Fairbanks, Alaska, *McCarrick et al.* [1990] successfully modulated the auroral electrojet using an array de-phasing technique to produce  $\sim 1$  pT signal levels in the 11-76 Hz range. *Li and Ferraro* [1990] demonstrated that HIPAS could be used to generate waves in the 1-5 kHz band, but did not provide an absolute calibration for their measurements. At the same time, *Lee et al.* [1990] demonstrated the ability to use the generated ELF/VLF signal (at  $\sim 1$  pT) to probe the ionosphere and detect geomagnetic pulsation events. *Villaseñor et al.* [1996] used the HF heater to create ELF/VLF waves through three different modulation techniques: 1) square-wave amplitude modulation, 2) the HF beam de-phasing technique employed by *McCarrick et al.* [1990], and 3) beat-frequency modulation, consisting of two separately-transmitted CW signals (in the HF range) spaced in frequency at the desired ELF/VLF frequency. Beat-frequency modulation is essentially equivalent to double-sideband, suppressed-carrier (DSSC) amplitude modulation when the two CW signals originate from the same HF transmitter. *Villaseñor et al.* [1996] determined that square-wave amplitude modulation appeared to be generally more efficient than both phase modulation (de-phasing) and beat-frequency modulation. *Rowland et al.* [1996] further analyzed the same three modulation schemes, showing that the beat-frequency modulation scheme produced no harmonics while the other two produced very many odd harmonics. This result is expected based on the harmonic content of the HF power density waveform. The ELF/VLF waves generated by HIPAS modulation have been detected in space by the Akebono satellite [*Kimura et al.*, 1991], and unlike the equivalent experiment performed using the Tromsø heater [*Kimura et al.*, 1994], ground-based observations were shown to be fairly consistent with the space-based measurements (within a factor of 3). As previously noted, the comparison between ground- and space-based measurements is an active current area of research.

### 1.1.4 HAARP, Alaska

ELF/VLF wave generation at HAARP has been carried out using varying HF frequency and polarization [Milikh *et al.*, 1999]. Results implied that the frequency and polarization of the heating HF waves could be used to control the polarization of the generated ELF wave. Using square wave modulation, Papadopoulos *et al.* [2003] linked the HF/ELF conversion efficiency to the timescale for electron collision frequency saturation in the *D*-region ionosphere, as a function of effective radiated power (ERP) and HF frequency. Observations agreed well with model calculations. At the same time, Papadopoulos *et al.* [2003] claimed that, in previous work in general, the amplitude of the harmonics relative to that of the fundamental are much higher than that expected by the Fourier analysis of the HF heating waveforms and that this observation is therefore not yet fully understood. In fact, measurements of the harmonics generated at HIPAS and presented by Rowland *et al.* [1996] show that this assertion is generally not true (e.g., in that case, relative harmonic amplitudes matched numerical simulations well). Other observations showing relatively higher harmonic content, such as those presented by James *et al.* [1984], have consistently been interpreted as the result of Earth-ionosphere waveguide resonances. Furthermore, the work by Barr and Stubbe [1993] demonstrated an approximate but elegant method to discount the waveguide resonance effects and to show that the relative harmonic amplitudes closely matched those expected from the Fourier analysis of the HF waveform. Although some assertions put forth by Papadopoulos *et al.* [2003] appear to be questionable, these authors do present excellent observations regarding the time-series waveforms of the generated ELF/VLF waves.

Stanford University involvement at HAARP has led to successful experiments involving the injection of ELF/VLF waves both upward into space and into the Earth-ionosphere waveguide. Platino *et al.* [2006] detected whistler-mode ELF/VLF waves from HAARP on the DEMETER satellite. For three out of four modulation frequencies, ground-based observations and satellite observations were almost perfectly consistent (within 10%) with radiated ELF/VLF power levels of  $\sim 3\text{--}4$  Watts. Ground-based measurements have also been used to demonstrate the successful injection of ELF/VLF waves into space. Inan *et al.* [2004] presented evidence of the

successful detection of the so-called multi-hop magnetospheric echoes of HAARP-induced ELF/VLF waves. The properties of the detected ELF/VLF waves exhibited evidence that they had been dispersed in the magnetosphere and had been amplified by wave-particle interactions near the geomagnetic equator, leading to the triggering of emissions.

Not only have HAARP-induced ELF/VLF waves been successfully injected into space, but they have also been successfully injected to great distances within the Earth-ionosphere waveguide. *Moore et al.* [2007] demonstrated the long-distance observation of ELF waves produced using the HAARP HF transmitter at a ground distance of  $\sim 4400$  km from the transmitter at Midway Atoll. Observations were shown to be consistent with a radiated ELF/VLF power of  $\sim 4$ -32 Watts from an ionospheric altitude of  $\sim 75$ -80 km [*Moore et al.*, 2007].

Other investigations at HAARP led to observations of saturation in the amplitude of ELF/VLF waves produced as a function of peak HF power level [*Moore et al.*, 2006], and this topic constitutes a large portion of this dissertation. In an effort to provide a context for the saturation observations presented herein, we now discuss previous investigations of the variation of ELF/VLF amplitude as a function of HF power level.

## 1.2 ELF/VLF Amplitude Dependence on HF Power

In comparison with the massive body of work that exists regarding ELF/VLF wave generation by modulated HF heating of the ionosphere in general, there are relatively few previous observations of the nonlinear variation of ELF/VLF amplitude with HF power level. The generation of ELF/VLF waves via HF heating is, in and of itself, nonlinear, in that the frequencies present in the output (i.e., the generated ELF/VLF signals) are not explicitly present in the system input (i.e., the spectrum of the transmitted HF signal). In addition to this primary nonlinearity, however, the dependence of the ELF/VLF amplitude on the intensity (or power) of the HF carrier

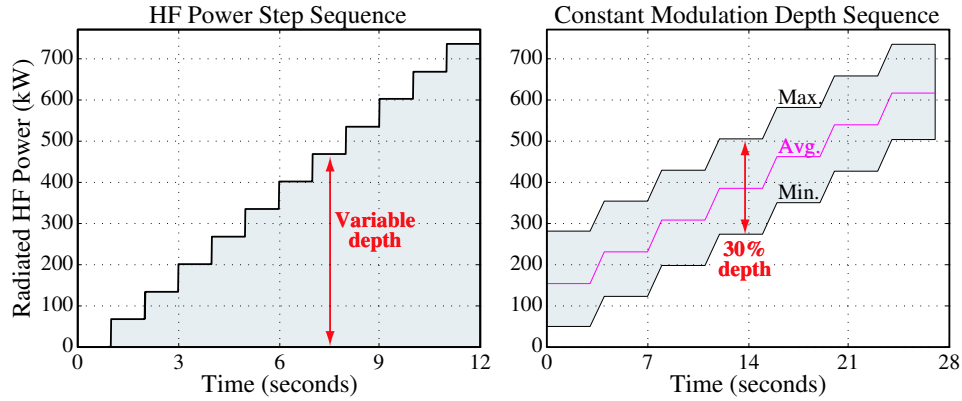


Figure 1.1: Sample HF transmission sequences for the two primary experiments presented in this dissertation: the power-step experiment and the modulation-depth experiment. The radiated power levels assume a 3.25 MHz HF frequency.

is also nonlinear. Two types of nonlinear variations of ELF/VLF amplitude with HF power are of interest to this dissertation: those resulting from the variation of peak HF power from zero to full power while keeping the minimum power at zero, and those resulting from the variation of the average HF power level between minimum and maximum levels while keeping the power modulation depth constant. Figure 1.1 graphically depicts a sample variation of HF power for each of these two types of modulation schemes. We address both of the associated nonlinearities in turn.

Observations of the first type of nonlinear effect were first reported by *Stubbe et al.* [1982], who measured ELF/VLF amplitudes generated at Tromsø using square-wave amplitude modulation, as shown in Figure 1.2. This nonlinearity was explored, albeit rather coarsely, by comparing the ELF/VLF amplitude produced by 0-50% power modulation to that produced by 0-100% power modulation (i.e., the left two panels of Figure 1.2). The ELF/VLF amplitude resulting from 0-50% power modulation was greater than half of the amplitude produced by the 0-100% transmission, indicating a degrading efficiency with increasing HF power. On the other hand, *Ferraro et al.* [1984] presented amplitude measurements of ELF/VLF wave generated at Arecibo using five different power levels, shown in Figure 1.3, which together indicated an approximately linear dependence of ELF/VLF amplitude on HF power. Subsequent theoretical developments presented by *Papadopoulos et al.* [1990] indicated that a

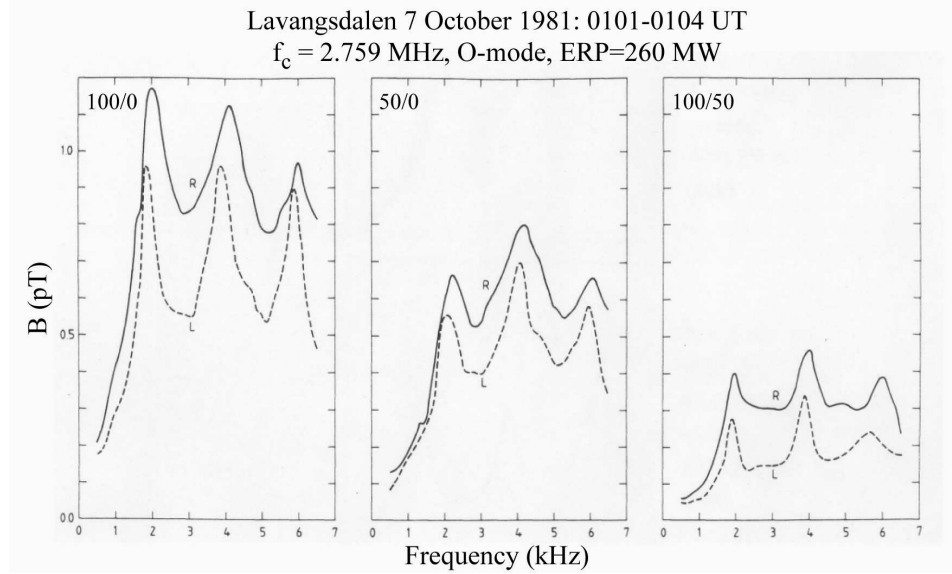


Figure 1.2: Experimental observations of ELF/VLF waves generated using the Tromsø HF heater presented by *Stubbe et al.* [1982]. Square-wave modulation was employed, using the maximum/minimum power levels (in percentage) listed in the upper left corner of each panel.

power-law dependence of ELF/VLF amplitude on HF power could explain both observations, a power-law variation with an exponent of 1 being the same as a linear variation. Ensuing observations at Tromsø reported by *Barr and Stubbe* [1991a], and shown here in Figure 1.4, indicated that ELF/VLF amplitude observations as a function of HF power level were consistent with a power-law dependence with exponent values varying between  $\sim 0.5$  and 1.1. At the same time, the conductivity saturation processes predicted by *Papadopoulos et al.* [1990] were not observed, despite the fact that the Tromsø “Super Heater” reached power densities more than ten times greater than the predicted saturation level [*Barr and Stubbe*, 1991a]. ELF/VLF amplitudes were shown to be essentially independent of the ERP of the HF antenna array, depending instead on the total HF power delivered to the ionosphere, which was  $\sim 1$  MW for the Tromsø heater [*Barr and Stubbe*, 1991a]. ELF/VLF waves generated during power-step experiments in 2004 using the HAARP HF heater indicated the onset of ELF/VLF amplitude saturation as a function of peak HF power level [*Moore et al.*, 2006]. The analysis of this observation at HAARP constitutes the bulk of Chapter 3

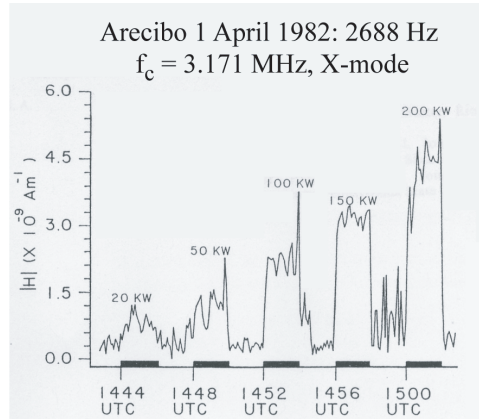


Figure 1.3: Experimental observations of ELF/VLF waves generated using different HF power levels at Arecibo and presented by *Ferraro et al.* [1984].

of this dissertation.

Observations of the second type of nonlinear effect were also first reported by *Stubbe et al.* [1982], who compared the ELF/VLF amplitude produced by 0-50% power modulation to that generated by 50-100% power modulation (i.e., both cases corresponding to 50% power modulation depth). The observations, shown in the right two panels of Figure 1.2, clearly indicated that ELF/VLF amplitudes produced using 0-50% power modulation were significantly stronger than those produced using 50-100% power modulation. In a system linearly dependent on HF power, these amplitudes would be equal because they have the same power modulation depth. However, the lower amplitudes at higher HF power levels may be explained by a power-law dependence of ELF/VLF amplitude on HF power level. This experiment was repeated with greater detail using the HAARP HF transmitter in August 2006, using a larger number of modulation depths and a larger number of average HF power levels. The observations associated with these HAARP transmissions are presented in Chapter 4 of this dissertation together with a numerical analysis of the results.

Although each of the previous studies analyzed the nonlinear dependence of the fundamental ELF/VLF amplitude on HF power, none of the past work investigated the dependence of the ELF/VLF harmonic amplitudes on the HF power level. In contrast, we use observations of the harmonic amplitudes as a function of HF power level

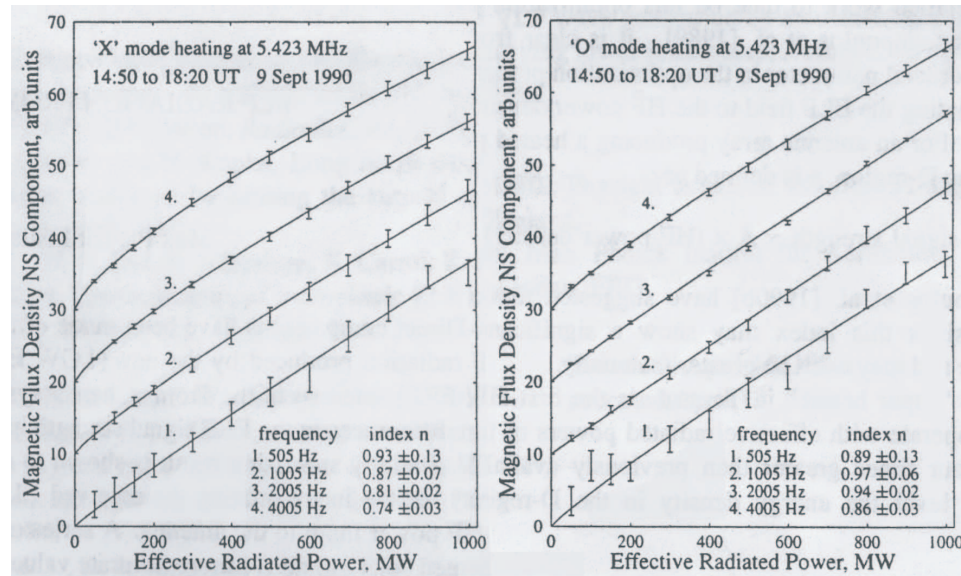


Figure 1.4: Experimental observations of ELF/VLF waves generated using the HF heater at Arecibo and presented by *Barr and Stubbe* [1991a]. A power-law dependence of ELF/VLF amplitude on HF power is evident.

throughout this dissertation in our quest to understand and quantify the nonlinear HF heating effects.

### 1.3 Scientific Contributions

The contributions to knowledge presented in this dissertation are as follows:

- The identification and quantification of amplitude saturation as a function of peak HF power in the generation of ELF/VLF waves by modulated HF heating of the auroral electrojet. In the context of an HF heating model, we demonstrate that the observed amplitude saturation results primarily from the non-linear dependence of the vibrational excitation of molecular oxygen on electron temperature.
- The identification of an optimal HF power level maximizing ELF/VLF signal amplitude for a <100% modulated signal. Modeling results indicate that the observed optimal HF power level results primarily from the competition between ionospheric self-absorption at low HF power levels, the vibrational excitation of molecular oxygen at mid-range HF power levels, and the rotational excitation of molecular nitrogen at high HF power levels.
- The establishment of the long-term variability of saturation effects. We demonstrate the regular occurrence of ELF/VLF amplitude saturation using a vast number of experimental observations. Further statistical analysis of this vast data set indicates that the spatial distribution of the ionospheric conductivity modulation can be detected at ground-based ELF/VLF receivers as a result of the described ELF/VLF amplitude saturation.

## Chapter 2

# ELF/VLF Wave Generation

# Physics and the HF Heating Model

The generation of ELF/VLF waves by modulated heating of the ionosphere in the presence of the auroral electrojet occurs as a combined result of several physical processes. In this dissertation, we employ a numerical model of the HF-induced ionospheric conductivity modulation to interpret the observations presented in Chapters 3 and 4, both of which discuss a type of ELF/VLF amplitude dependence on HF power. The numerical HF heating model is based on previous work and assumes that the electron energy distribution remains Maxwellian throughout the HF heating and ELF/VLF wave generation processes. In this chapter, we provide an overview of the background physics and the HF heating model employed and discuss the three primary nonlinearities involved in the calculations in order to provide a basis for the analyses presented throughout this dissertation.

### 2.1 General Overview

The ELF/VLF wave generation process is summarized in cartoon form in Figure 2.1. HF heating of the ionosphere heavily depends upon the ambient ionospheric conditions (i.e., electron density and electron-neutral collision frequency as a function of altitude). It is well known that the nighttime ionospheric parameters may vary

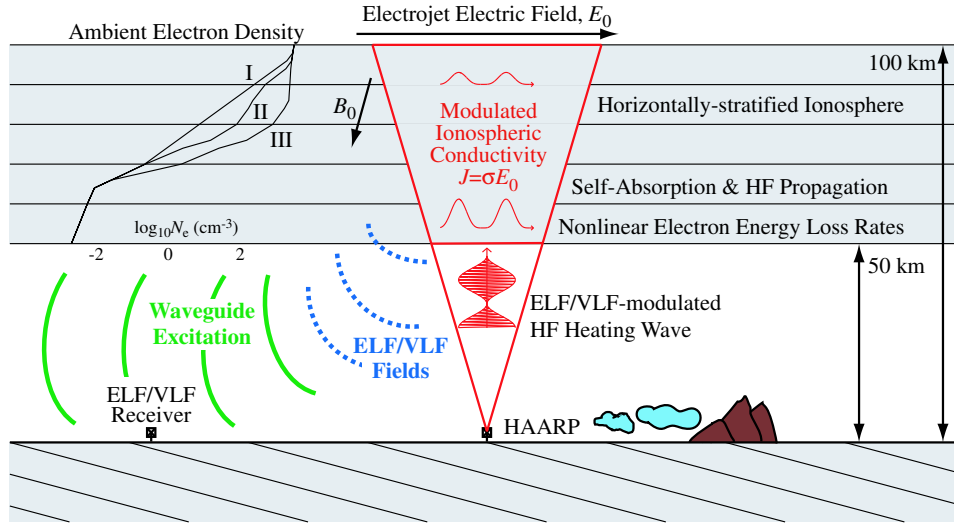


Figure 2.1: Cartoon: Summary of ELF/VLF wave generation process. The amplitude-modulated HF heating wave is absorbed by the ionospheric plasma, modulating the conductivity,  $\sigma$ . The current density,  $J = \sigma E_0$ , radiates electromagnetic waves at ELF/VLF frequencies which then couple to the Earth-ionosphere waveguide.

significantly over relatively short periods of time [e.g., see *Barr et al.*, 1991]. The upper-left portion of Figure 2.1 shows three nighttime electron density profiles that have been used in previous VLF propagation studies, such as those by *Lev-Tov et al.* [1995] and *Moore et al.* [2003], to represent tenuous (I) to dense (III) ionospheric conditions. We use these example profiles in this Chapter in the evaluation of the HF heating model described herein. Other ionospheric parameters also play a role in the HF heating process. The ambient electron temperature, together with the molecular nitrogen and molecular oxygen densities, are taken from the MSIS-E-90 Atmosphere Model provided by the Goddard Space Flight Center’s Space Physics Data Facility available on the Web at <http://modelweb.gsfc.nasa.gov/>. Although values for these different ionospheric parameters may be provided by models, the nighttime *D*-region ionosphere is highly variable, particularly at auroral and sub-auroral latitudes [e.g., *Cotton and Smith*, 1991; *Cummer et al.*, 1996]. The purpose of this HF heating model, therefore, is to provide a general zero-order basis for the interpretation of experimental observations as a function of HF power.

The modulated HF heating model developed herein to calculate the modulation

of ionospheric conductivity generally follows the work by *Rietveld et al.* [1986], with several notable differences. The electron energy loss rates used in our work are the same as those used by *Rodriguez* [1994], which are similar to, but different from, those used by *Rietveld et al.* [1986]. Another distinction is that we employ kinetic expressions to calculate the HF absorption and the DC conductivity modulation, assuming that the electron energy distribution is Maxwellian and that the collision frequency is proportional to electron energy [i.e.,  $\nu(v) \propto v^2$ ]. Unlike the work of *Rietveld et al.* [1986], but similar to the work of other authors, such as *Barr and Stubbe* [1984a] and *James* [1985], we calculate the complete temporal development of the electron temperature  $T_e$ . Fully kinetic codes, such as those developed by *Papadopoulos et al.* [1990] and *Zhou et al.* [1996], account for the evolution of the electron energy distribution as a function of time throughout the HF heating process. The deviation of the electron energy distribution from a Maxwellian shape during the HF heating process is not accounted for in our work.

Given the ionospheric parameters, an amplitude-modulated HF wave periodically heats the ionospheric plasma, as shown in the central section of Figure 2.1. This heating effect results from the absorption of the HF wave energy by collisional processes within the ionospheric plasma [*Ratcliffe*, 1959, p. 40]. The direction and magnitude of the Earth's magnetic field, shown as  $B_0$ , affects the absorption of the HF wave, which is determined by the refractive index of the ionospheric medium. The refractive index,  $n$ , for a weakly-ionized collisional magnetoplasma, such as the Earth's *D*-region ionosphere, is well-known from classical magneto-ionic theory [*Appleton*, 1932; *Ratcliffe*, 1959]:

$$n^2 = 1 - \frac{X}{1 - jZ - \frac{Y^2 \sin^2 \Theta}{2(1 - X - jZ)} \pm \sqrt{\frac{Y^4 \sin^4 \Theta}{4(1 - X - jZ)^2} + Y^2 \cos^2 \Theta}} \quad (2.1)$$

where '+' is for O-mode HF polarization, '-' is for X-mode HF polarization,  $\Theta$  is the angle between the HF wave normal and the Earth's magnetic field, and

$$X = \frac{\omega_{pe}^2}{\omega^2} \quad ; \quad Y = \frac{\omega_{ce}}{\omega} \quad ; \quad Z = \frac{\nu_{\text{eff}}}{\omega} \quad (2.2)$$

The quantity  $\omega_{pe}$  is known as the electron plasma frequency given by:

$$\omega_{pe} = \sqrt{\frac{N_e q_e^2}{\varepsilon_0 m_e}} \quad (2.3)$$

where  $N_e$  is the electron density,  $q_e$  is the charge of an electron,  $\varepsilon_0$  is the permittivity of free-space, and  $m_e$  is the mass of an electron.

The quantity  $\omega_{ce}$  is the electron cyclotron frequency given by:

$$\omega_{ce} = \frac{|q_e| B_0}{m_e} \quad (2.4)$$

where  $B_0$  is the magnitude of the Earth's magnetic field.

Lastly,  $\nu_{\text{eff}}$  is the effective momentum transfer electron-neutral collision frequency [e.g., see *Rodriguez, 1994*]. It is this magneto-ionic quantity,  $\nu_{\text{eff}}$ , that is the primary temperature-dependent electrical quantity modulated by HF heating. Strictly speaking, the temperature dependence of the electron-neutral collision frequency indicates a velocity dependence, and Equation (2.1) is derived for a velocity-independent collision frequency. In order to account for a velocity-dependent electron-neutral collision frequency, the Sen-Wyller formulae [*Sen and Wyller, 1960*], which constitute a kinetic derivation of Equation (2.1) for  $\nu(v) \propto v^2$ , may be used for our application [*Budden, 1985, p. 57*]. The average momentum transfer collision frequency  $\nu_{\text{av}}$  depends on the electron energy distribution, which is assumed to remain Maxwellian throughout the HF heating process, and this parameter is used in calculating the electron energy loss rates as well as other parameters throughout this dissertation. The effective momentum transfer collision frequency  $\nu_{\text{eff}}$  is the velocity-independent collision frequency that results in the same refractive index using Equation (2.1) as that computed using the velocity-dependent average collision frequency  $\nu_{\text{av}}$  in the Sen-Wyller formulae. For an HF wave propagating approximately along the Earth's magnetic field line (i.e., using the quasi-longitudinal approximation), and under the condition that  $\nu_{\text{av}} \ll |\omega \pm \omega_{ce}|$ , Equation (2.1) is consistent with the Sen-Wyller formulae if  $\nu_{\text{eff}} = \frac{5}{3} \nu_{\text{av}}$  [*Budden, 1965; Rodriguez, 1994*]. For the HF frequencies and the ionospheric profiles used in this work, this approximation of the Sen-Wyller derivation is

valid for altitudes greater than  $\sim 63$  km. We use this approximation and assume that the error accrued by applying it at altitudes below 63 km is negligible. Because the maximum HF absorption effects shown in this work are in the 70-80 km range (i.e., higher in altitude than  $\sim 63$  km), such an assumption appears to be reasonable. It should be noted that this same approximation, i.e.,  $\nu_{\text{eff}} = \frac{5}{3}\nu_{\text{av}}$ , to the Sen-Wyller equations is valid for  $\nu_{\text{av}} \ll \omega$  in the quasi-transverse case (for example corresponding to geomagnetic equatorial HF heating).

The resulting refractive index is in general complex,  $n = \mu - j\chi$ , and it determines the phase velocity ( $c/\mu$ ) and the rate of absorption,  $\chi$ , of the HF wave propagating through the ionospheric medium. The electrical conductivity of the HF-heated region also depends on the temperature-dependent electron-neutral collision frequency; thus, the amplitude-modulated HF signal periodically modifies the ionospheric conductivity  $\sigma$ . The modification of ionospheric conductivity, assuming the ionospheric electron energy distribution remains Maxwellian throughout the heating process, has been fully developed theoretically, although the specific physical processes included vary from author to author [e.g., *Stubbe et al.*, 1977; *Tomko et al.*, 1980; *James*, 1985; *Rietveld et al.*, 1986; *Rodriguez*, 1994]. Overall, results indicate that the plasma heating and cooling rates at ionospheric altitudes are such that modulation frequencies in the ELF/VLF range efficiently produce time-harmonic conductivity changes [e.g., *Stubbe et al.*, 1977; *Rietveld et al.*, 1986].

Modulation of the ionospheric conductivity does not by itself produce electromagnetic radiation. In the presence of a driving electric field, such as that associated with the auroral electrojet and labelled  $E_0$  in Figure 2.1, the modulated conductivity produces a current density  $J = \sigma E_0$  which is time-harmonic at integer multiples of the HF modulation frequency. This time-harmonic current density radiates electromagnetic waves at the modulation frequency and its harmonics, and these waves are subsequently detected at ground-based receivers. Other so-called loop-back currents may be formed in the ionosphere as a direct result of the charge transport induced by the primary currents [e.g., see *Zhou et al.*, 1996]. Although these loop-back currents may contribute to the absolute magnitude of the received ELF/VLF magnetic field on the ground, the strength of these loop-back currents likely varies with HF power

in the same manner as one or both of the primary currents. In this dissertation, we assume that such loop-back currents do not significantly change the calculated variation of ELF/VLF magnetic field amplitude with HF power, essentially neglecting charge transport, as has been common practice in previous ELF/VLF wave generation work [e.g., *Tripathi et al.*, 1982; *Barr and Stubbe*, 1984b,a; *James*, 1985; *Rietveld et al.*, 1986; *Rowland*, 1999; *Papadopoulos et al.*, 2003].

The generated electromagnetic waves may propagate toward the Earth and reflect several times between the Earth and the lower boundary of the ionosphere, as has been directly observed by *Papadopoulos et al.* [2005]. These waves have been shown to successfully excite propagation modes within the Earth-ionosphere waveguide [*Barr et al.*, 1986], as indicated in the lower left-hand portion of the cartoon. In our work, we assume that the effect of the boundary conditions imposed on the system by the Earth-ionosphere waveguide depends on the ambient ionospheric parameters, rather than the HF-modified ionospheric parameters. As a result, the amplitude of the generated ELF/VLF waves may be considered to be proportional to the amplitude of the HF-induced conductivity modulation, especially when considered as a function of HF power.

Although the physical mechanisms involved in the generation of ELF/VLF waves have been well-developed over the years, the relatively high variability of the *D*-region ionospheric parameters and the relatively few methods available for the experimental measurement of these parameters limits the predictive capabilities of any HF heating model. Although specific details of individual cases cannot be calculated without knowledge of ionospheric parameters in effect at the time, general trends can be effectively investigated with the HF heating model. In this work, the HF heating model is employed to examine the variation of conductivity modulation as a function of HF power for a range of ionospheric parameters. As we inspect the generation of ELF/VLF waves as a function of HF power, accounting for each of the previously mentioned effects, three primary nonlinearities are most important. The first two nonlinearities are involved in the modulation of the *D*-region ionospheric electron temperature. The third nonlinearity resides in the relationship between the electron temperature to the ionospheric conductivity. We now address the physical processes

modulating the electron temperature and then move on to the relationship between electron temperature and ionospheric conductivity.

## 2.2 Electron Temperature Modulation

Modification of the ionospheric conductivity results from the temperature dependence of the electron-neutral collision frequency. We therefore first calculate the variation of the ionospheric electron temperature with time. As indicated in Figure 2.1, the modification of electron temperature is modeled in this work using a horizontally-stratified ionosphere. Throughout the heating process, the electron temperature in each ionospheric slab is determined by a localized energy balance equation [Huxley and Ratcliffe, 1949; Maslin, 1974; Stubbe *et al.*, 1977; Tomko *et al.*, 1980; Rietveld *et al.*, 1986; Rodriguez, 1994]:

$$\frac{3}{2}N_e\kappa_B\frac{dT_e}{dt} = \underbrace{2k\chi(T_e)S}_{\text{HF absorption}} - \underbrace{L(T_e, T_0)(T_e - T_0)}_{\text{electron energy loss}} \quad (2.5)$$

where  $N_e$  is the altitude-dependent electron density,  $\kappa_B$  is Boltzmann's constant,  $T_e$  is the time-varying electron temperature in the ionospheric slab,  $k$  is the HF free-space propagation constant,  $\chi(T_e)$  is the temperature-dependent rate of absorption in the plasma (the imaginary part of the refractive index,  $n$ ),  $S$  is the time-varying power density of the HF wave, and  $L$  is the sum total of all electron energy loss rates, which depend in general on both the ambient electron temperature  $T_0$  and the time-varying electron temperature  $T_e$ . In this work, inelastic electron energy losses due to rotational and vibrational excitation of molecular oxygen and molecular nitrogen are accounted for, together with elastic collisional losses. It is evident from Equation (2.5) that the absorption of an HF wave increases the ionospheric electron temperature while the electron energy loss works to decrease the temperature.

There are two aspects to Equation (2.5) that deserve further discussion: the role of the electron density,  $N_e$ , and the role of HF absorption versus that of the electron energy loss rates. The electron density,  $N_e$ , is a function of electron temperature

through ionospheric chemical reactions and is therefore a function of the HF amplitude [Willis and Davis, 1973; Stubbe *et al.*, 1982]. However, the timescale for electron density change (i.e., the chemical rate of reaction) is much larger than the modulation periods employed in this dissertation [Willis and Davis, 1973; Stubbe *et al.*, 1982; Barr, 1998]. Accordingly, in our work we approximate the ionospheric electron density as a static function of time. Changes in electron density may result at altitudes where the electron temperature does not fully recover to the ambient value within each modulation period (i.e., the heating rate is greater than the cooling rate). The ionosphere at such altitudes is effectively heated continuously at a lower HF power level (one that would result in the minimum electron temperature experienced under modulated heating). ELF/VLF-modulated HF heating that persists for several minutes may thus create electron temperature changes at some altitudes that satisfy the timescales necessary to affect electron density change. Electron density changes related to such effects are neglected in this work.

The primary difference between the role of HF absorption and that of the electron energy loss rates is also not immediately clear from Equation (2.5). For a CW transmission, when  $dT_e/dt = 0$ , the modified steady-state electron temperature results from the exact balance of the HF absorption rate and the electron energy loss rates. At the same time, the rate at which the electron temperature adjusts toward this steady-state value is directly affected by the dependence on electron temperature of both the HF absorption rate and the electron energy loss rates. The rates of these processes thus couple to one another through the dependence on electron temperature. In this regard, the electron energy loss rates play the same role as the HF absorption rate, although one adds energy to the system while the other subtracts energy from the system. However, the local HF absorption rate at a given altitude also affects the variation of electron temperature at higher altitudes (i.e., not only on a local level) through the so-called self-absorption of the propagating HF wave. For an HF wave with no modulation, the power density may be expressed as [Tomko *et al.*, 1980]:

$$S(z) = S_0 \left( \frac{z_0}{z} \right)^2 \exp \left[ -2k \int_{z_0}^z \chi(z') dz' \right] \quad (2.6)$$

$$S_0 = \frac{P_T G}{4\pi z_0^2} \quad (2.7)$$

where  $P_T$  is the transmitter power,  $G$  is the antenna gain, and  $z$  is the altitude.  $S_0$  represents the power density at an altitude of  $z_0$ , which is taken to be the base of the ionosphere (the altitude at which free-space ends). If ionospheric reflections are neglected, the effects of the electron energy loss rates may only couple to higher altitudes via the HF absorption process. Using a horizontally-stratified ionosphere and calculating the absorption of the HF wave within each slab essentially approximates the absorption integral in Equation (2.6). In the case of ELF/VLF amplitude modulation, Equation (2.6) is complicated by the fact that at each altitude  $z'$ , each portion of the modulated waveform experiences a different rate of absorption due to the electron temperature dependence of the HF absorption rate. It should be noted here that Equation (2.6) is a simplification that results from approximating the ionospheric medium as slowly-varying over distances on the order of the HF wavelength (i.e., the so-called W.K.B. approximation) [e.g., see *Budden*, 1985, p. 170]. At HF frequencies, the conditions for using the W.K.B. approximation are easily satisfied in the *D*-region ionosphere [*Budden*, 1985, p. 177].

The HF absorption and the electron energy loss rates are the two primary processes with nonlinear dependencies on HF power that affect the modulation of the ionospheric electron temperature. In order to properly evaluate the dependence of ELF/VLF wave generation on each nonlinearity, it is imperative to evaluate Equation (2.5) while properly accounting for the coupling between each of the nonlinear terms. The general method for calculating the electron temperature variation as a function of time and altitude starts with the steady-state solution for the temperature modulation in the lowest altitude slab, subsequently propagates the HF wave through the modified slab, and repeats the procedure at the next ionospheric slab. In this context, we note that ‘steady-state’ for a modulated temperature waveform does not necessarily imply that  $dT_e/dt = 0$ , but instead implies that the waveform has attained a periodic state. This procedure is continued until calculations are complete for the highest ionospheric slab (i.e., until a periodic steady state is reached therein). In order to ensure that steady-state has been achieved, the modulated temperature

for one modulation period is compared against that from the previous modulation period and the average percent change is ensured to be below a set threshold value (typically 0.2%). In order to ensure the convergence of the approximation of the absorption integral in Equation (2.6), the slab width is iteratively halved in size until the resulting average percent change in temperature is less than another set threshold value (typically 0.1%). The threshold error rates are chosen to maximize calculation accuracy while allowing for manageable computational run-times.

The calculation of the power density waveform,  $S$ , as a function of altitude is also important to the proper evaluation of Equation (2.5). HF ray tracing must then be performed self-consistently with the HF heating calculations. The evaluation of ionospheric temperature modulation thus has three parts: the propagation of the HF wave to the ionospheric slab, the absorption of HF wave energy by the ionospheric plasma, and loss of energy from the ionospheric plasma by elastic and inelastic collisions between electrons and neutral molecules. These processes are coupled through their dependence on electron temperature. In the remainder of this section, we discuss each of these processes in turn.

### 2.2.1 HF Ray Tracing

We assume the HF signal propagates in free-space prior to reaching the first ionospheric slab. Upon reaching ionospheric altitudes, the radius of curvature of the HF wavefront is on the order of 40 km and is much larger than the HF wavelength ( $\sim 100$  m). As a result, we may calculate the HF power density at these altitudes using plane wave approximations. For the vertical propagation of a linearly polarized wave:

$$E_x(z, t) = \frac{A_0}{z} A_m \left( t - \frac{z}{v_g} \right) \cos(\omega_c t - k_c z) \quad (2.8)$$

$$H_y(z, t) = \frac{A_0}{\eta z} A_m \left( t - \frac{z}{v_g} \right) \cos(\omega_c t - k_c z) \quad (2.9)$$

$$\langle S(z, t) \rangle = \langle E \times H \rangle = \hat{\mathbf{z}} \frac{A_0^2}{2\eta z^2} A_m^2 \left( t - \frac{z}{v_g} \right) = \hat{\mathbf{z}} \frac{P_{\text{peak}}}{4\pi z^2} A_m^2 \left( t - \frac{z}{v_g} \right) \quad (2.10)$$

where  $\hat{\mathbf{z}}$  is the unit vector in the vertical direction,  $\hat{\mathbf{x}}$  and  $\hat{\mathbf{y}}$  are orthogonal unit vectors parallel to the ground,  $P_{\text{peak}}$  is the transmitter power times the antenna gain,  $A_m(t)$  is the amplitude modulation waveform, normalized between zero and one, and  $v_g$  is the group velocity of the HF signal. Equation (2.10) is similar to Equation (2.7), but accounts for the time-dependence of the modulation waveform.

In general, we desire to calculate the ionospheric heating along a ray path that starts at an angle,  $\alpha$ , from the center of the HF beam, and the center of the HF beam may be directed away from the vertical by an angle,  $\beta$ . We assume that the power density of the HF beam varies in a Gaussian manner with the angle  $\alpha$ . Half-power beamwidth information for the HAARP HF transmitter is given in Table 2.1 as a function of HF frequency. These values are calculated using data from the HAARP website performance calculator (<http://www.haarp.alaska.edu/haarp/calciri.html>). The beamwidth of the HAARP HF transmitter is different in the North-South and East-West directions, and in order to simplify calculations, we use the average 3-dB beamwidth that results in the same area as an ellipse with the given beamwidths (i.e.,  $\tan(\bar{\alpha}/2) = \sqrt{\tan(\alpha_{\text{ns}}/2) \tan(\alpha_{\text{ew}}/2)}$ ). Modifying Equation (2.10) to account for the Gaussian HF beam shape and for the off-vertical propagation of the HF wave results in the following general expression for the power density at the base of the ionosphere:

$$S_0 = \langle S(z_0, t) \rangle = \hat{\mathbf{r}} \frac{P_{\text{peak}}}{4\pi r_0^2} \left(\frac{1}{2}\right)^{4\alpha^2/\bar{\alpha}^2} A_m^2\left(t - \frac{r_0}{v_g}\right) \quad (2.11)$$

where  $r_0 = z_0/\cos(\beta)$  and  $z_0$  is the altitude of the base of the ionosphere. In this case,  $\hat{\mathbf{r}}$  is the direction of HF power flow (i.e., the HF ray path). Note that while the angle  $\bar{\alpha}$  represents the full (2-sided) 3-dB beamwidth of the HF transmission, the angle  $\alpha$  represents the angle between the k-vector and the center of the HF beam (1-sided).

The flow of the power density  $S$  through the ionosphere depends on a number of factors: the attenuation of the wave as it traverses each slab, the bending of the wave k-vector at slab boundaries, the bending of the ray, which may diverge from the direction of the k-vector in an anisotropic plasma, and the speed at which the amplitude envelope propagates across each slab (i.e., the altitude-dependent group velocity). In principle, each of these quantities is dependent on the amplitude of the HF wave,

Table 2.1: HAARP parameters versus HF frequency

Frequency (MHz)	Beamwidth ( $\bar{\alpha}$ , deg)	Effective Radiated Power ( $P_{\text{peak}}$ , dBW)
3.25	33.1	72.6
4.5	23.5	77.4
5.8	18.2	79.6
6.9	15.3	81.1
7.5	14.1	81.8

which modifies the electrical properties of the ionospheric plasma through electron heating. However, for the HF power levels used during the experiments presented in this dissertation, only the absorption of the HF wave is significantly affected by the HF modification of the ionospheric plasma. The bending of the k-vector, the deviation of the ray path, and the HF group velocity may each be accurately approximated throughout the modulated heating process using the ambient ionospheric parameters.

Because the ionospheric plasma is, in general, lossy as well as anisotropic, HF ray tracing should be performed using so-called ‘complex rays’ [Budden, 1985, p. 417], which may trace HF ray paths consisting of complex-valued spatial coordinates. Because the imaginary part of the refractive index,  $n = \mu - j\chi$ , in the *D*-region ionosphere is small (i.e.,  $|\tan^{-1}(\frac{\mu}{\chi})| < 10^\circ$ ) even under HF-heated conditions, the ‘complex ray’ equations may be dramatically simplified by using ‘real pseudo rays’: the real part of the refractive index,  $\mu$ , may be used to evaluate the bending of the k-vector (directly via Snell’s law of refraction), while the imaginary part of the refractive index,  $\chi$ , may be used to evaluate the absorption of the HF wave as it traverses the slab along its raypath [Budden, 1985, p. 422]. For each boundary within the horizontally-stratified ionosphere, the employed modified version of Snell’s law of refraction states:

$$\mu_1 \sin \theta_1 = \mu_2 \sin \theta_2 \quad (2.12)$$

where  $\mu$  is the real part of the refractive index,  $\theta$  is the angle between the k-vector and the normal to the boundary, and the subscripts, 1 and 2, refer each quantity to the ionospheric slabs on either side of the boundary. Snell’s law ensures the continuity of

the HF wave phase crests across the boundary plane, so that the direction of the k-vector component in the plane of the boundary is the same in both slabs. While Snell's law of refraction preserves the direction of the component of the wave k-vector in the plane of the boundary, the calculation is complicated by the presence of the Earth's magnetic field, which affects the refractive index on both sides of the boundary, as is evident from Equation (2.1). The Earth's magnetic field is generally not aligned with the slab boundary normal and thereby creates another axis of symmetry within each ionospheric slab. Snell's law of refraction must therefore be solved consistently by accounting for the effects of the Earth's magnetic field. In this work, we perform this calculation using numerical techniques.

In the magnetized plasma that is the ionosphere, the HF ray path (i.e., the path that the wave energy follows) is not necessarily aligned with the k-vector, due to the anisotropy created by the presence of the Earth's magnetic field within the weakly ionized medium. Due to the rotationally symmetric properties of this anisotropy, the deviation of the HF ray path from the k-vector direction is confined to the plane created by the wave k-vector and the direction of the Earth's magnetic field. The Earth's magnetic field changes the ray path by an angle  $\delta$  which is positive when the ray path is pulled closer to the direction of the magnetic field and negative when the ray path is pushed farther away from the magnetic field. The bending of the ray direction from the k-vector direction is calculated as shown by [Budden, 1985, p. 110]:

$$\tan \delta = \frac{1}{n} \frac{\partial n}{\partial \Theta} \quad (2.13)$$

where the refractive index  $n$  depends on the angle  $\Theta$  between the direction of the HF wave normal and the direction of the Earth's magnetic field, as indicated in Equation (2.1).

Just as important as the location of our heating HF beam is the timing, or phasing, of the HF beam as a function of altitude. The wave group velocity is the speed at which the modulation waveform (and wave energy) propagates through the ionosphere in the ray direction. The group velocity is important to the calculation of the relative timing between temperature modulations at different altitudes (i.e., relative phasing)

and therefore directly affects the ELF/VLF radiation observed on the ground. The group velocity is also calculated using the method shown by [Budden, 1985, p. 130]:

$$v_g = \left[ \frac{c}{\partial(\omega n)/\partial\omega} \right] \frac{1}{\cos \delta} \quad (2.14)$$

where  $\omega = 2\pi f_{\text{HF}}$  and  $\delta$  is as defined by Equation (2.13).

Close inspection of Equations 2.12–2.14 reveals significant computational complication in the case that HF heating significantly affects the k-vector direction, the ray direction, and the wave group velocity. In such a case, the bending of the wave normal at ionospheric slab boundaries changes direction as a function of HF amplitude (and therefore time). The deviation of the ray path from the wave normal (which varies with time) would then also be a function of time. Lastly, the speed at which the HF amplitude traverses the slab (in the time-varying direction of the ray path) would vary with HF amplitude, further increasing the spatial variation of HF energy absorption. For the *D*-region ionospheric electron density profiles (I-III) used in this work and shown in Figure 2.1, however, calculations indicate that the effects of HF heating (even using the future HAARP power level of 3600 kW) on each of these quantities is negligible and the use of ambient ionospheric parameters is sufficient for accurate tracing of the HF ray path.

While the ambient ionospheric parameters may be used to accurately solve for the bending of the k-vector, the deviation of the ray path, and the group velocity of the HF wave, the modified ionospheric parameters are needed in order to calculate the attenuation of the HF wave itself. Therefore, the variation of the power density waveform needs to be solved self-consistently with the HF heating of the slab. In the next subsection, we discuss the effects of this so-called HF self-absorption process.

### 2.2.2 HF Self-Absorption

HF self-absorption is one of the primary nonlinearities investigated in this dissertation. The effect is deemed “self-absorption” because the absorption of the HF wave by the ionospheric plasma subsequently modifies the rate of absorption of the same HF wave. The effect is manifested as a change in the rate of HF absorption as a function of

time. In addition to this time-dependent variation in absorption, the complicated nonlinear dependence of the refractive index (see Equation (2.1)) on the effective electron-neutral collision frequency  $\nu_{\text{eff}}$  indicates a nonlinear dependence on the HF power level. In this subsection, we briefly describe HF self-absorption both as a function of time and as a function of HF power.

HF self-absorption is most easily understood for the case of square-wave amplitude modulation. The cartoon in Figure 2.2 depicts the time-averaged HF power density both before and after propagation across an ionospheric slab for HF waves at two different power levels, labelled I and II. The input and output waveforms are normalized to the input waveform, so that the input waveform shown for the two different power levels is the same. When the HF wave turns ON, the initial rate of absorption for the HF wave at both power levels is the same, and that attenuation rate is based on the ambient ionospheric parameters. As the ionosphere absorbs energy from the HF wave, the rate of absorption itself changes as a function of time. Both the rate of change and the final magnitude of the change in attenuation rate depends on the HF power level, as shown in Figure 2.2. In the case depicted, the time-averaged HF power density decreases with time as a result of the increasing absorption rate, but this is not always the case – at lower altitudes, for instance, the rate of absorption may actually decrease with time.

It is important to note that Figure 2.2 is a cartoon that represents the self-absorption reaction to initial transmitter turn-on. At steady-state, the recovery rate of the ionospheric electron temperature during the transmitter OFF periods may be such that the electron temperature does not fully recover to its ambient value. In such a case, the initial rate of absorption is not the same for the HF signals at power levels I and II. This effect is dominated by the electron energy loss rates, as discussed in the next subsection, and is a primary means of coupling between the two different nonlinear effects.

Further analysis is performed in Chapters 3 and 4 using a linearized version of Equation (2.5) in order to delineate between linear and nonlinear effects of self-absorption. In order to linearize the effects of self-absorption, the following formula

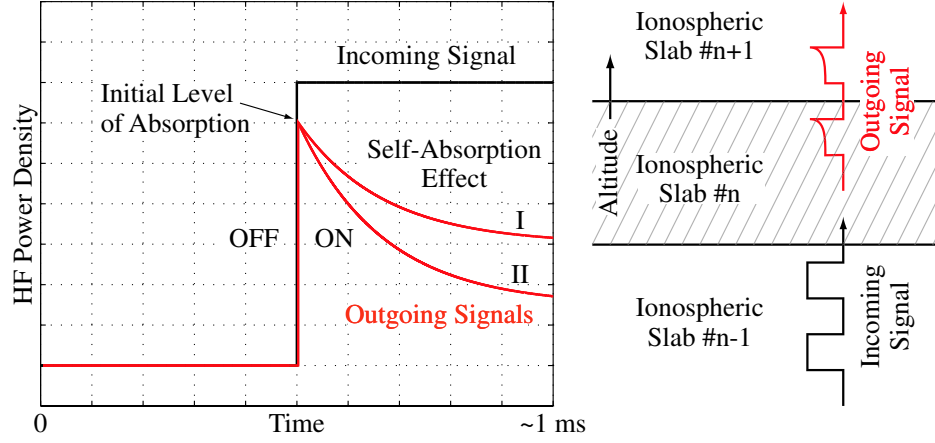


Figure 2.2: Cartoon: exaggerated effects of HF self-absorption as a function of time and HF power level (I and II).

is applied at each altitude instead of Equation (2.5):

$$\frac{3}{2}N_e\kappa_B\frac{dT_e}{dt} = 2k\overline{\chi(T_e)}S - L(T_e, T_0)(T_e - T_0) \quad (2.15)$$

where  $\overline{\chi(T_e)}$  is the average attenuation rate for the localized temperature range calculated using the full HF heating model employing Equation (2.5). This average attenuation rate  $\overline{\chi(T_e)}$  is still altitude-dependent. Equation (2.15) enacts a scenario in which the absorption of the HF wave no longer depends on the variation of the HF power with time. At the same time, the absorption parameters are not based solely on the ambient ionospheric parameters, but instead represent the average of the absorption parameters created under modulated HF heating conditions.

### 2.2.3 Ionospheric Recovery: Electron Energy Loss Rates

The nonlinear effects of ionospheric HF self-absorption are accompanied by the effects due to the nonlinear temperature dependence of the electron energy loss rates. Here we describe the temperature dependence of the electron energy loss rates and discuss the dependence on HF power level.

The electron energy loss rates used in this dissertation are effectively the same as

those employed by *Rodriguez* [1994]. These factors account for energy losses due to elastic collisions as well as those due to inelastic collisions caused by the excitation of rotational and vibrational modes in molecular nitrogen and molecular oxygen. The loss rate cross sections are empirical functions derived from laboratory measurements under the assumption that the electron energy distribution is Maxwellian [*Mentzoni and Row*, 1963]. Unlike the loss rates listed by *Rodriguez* [1994], however, the quantity  $(T_e - T_0)$  has been factored from the loss rates listed here so that the time-variation of the electron temperature recovery from disturbed conditions may be approximated as  $e^{-L(T_e, T_0)t}$ . While this factoring does not make a difference in the numerical evaluation of the loss rates [the term is re-introduced in Equation (2.5)], it does highlight the exponential nature of the electron temperature recovery from a modified state as well as its variation as a function of electron temperature. Hence, the units of the energy loss rates listed here are Watts per Kelvin.

The electron energy loss rates for elastic collisions are [*Rodriguez*, 1994, and references therein]:

$$L_{\text{elast}}(e, \text{N}_2) = 1.89 \times 10^{-44} N_e N_{\text{N}_2} (1 - 1.21 \times 10^{-4} T_e) T_e \quad \text{W/K} \quad (2.16)$$

$$L_{\text{elast}}(e, \text{O}_2) = 1.29 \times 10^{-43} N_e N_{\text{O}_2} (1 + 3.6 \times 10^{-2} T_e^{1/2}) T_e^{1/2} \quad \text{W/K} \quad (2.17)$$

where  $N_{\text{N}_2}$  is the number density of nitrogen molecules ( $\text{m}^{-3}$ ),  $N_{\text{O}_2}$  is the number density of oxygen molecules ( $\text{m}^{-3}$ ), and where we have assumed that the temperature of the oxygen and nitrogen molecules is the same as the ambient electron temperature,  $T_0$ . These equations directly result from the expressions for the respective momentum transfer collision frequencies [*Rodriguez*, 1994, and references therein]:

$$\nu_{\text{av}}(e, \text{N}_2) = 2.33 \times 10^{-17} N_{\text{N}_2} (1 - 1.21 \times 10^{-4} T_e) T_e \quad \text{s}^{-1} \quad (2.18)$$

$$\nu_{\text{av}}(e, \text{O}_2) = 1.82 \times 10^{-16} N_{\text{O}_2} (1 + 3.6 \times 10^{-2} T_e^{1/2}) T_e^{1/2} \quad \text{s}^{-1} \quad (2.19)$$

$$\nu_{\text{av}} = \nu_{\text{av}}(e, \text{N}_2) + \nu_{\text{av}}(e, \text{O}_2) \quad \text{s}^{-1} \quad (2.20)$$

The expression for the electron energy loss due to the excitation of rotational

modes are [*Rodriguez*, 1994, and references therein]:

$$L_{\text{rot}}(\text{e}, \text{N}_2) = 4.65 \times 10^{-39} N_e N_{\text{N}_2} T_e^{-1/2} \quad \text{W/K} \quad (2.21)$$

$$L_{\text{rot}}(\text{e}, \text{O}_2) = 1.11 \times 10^{-38} N_e N_{\text{O}_2} T_e^{-1/2} \quad \text{W/K} \quad (2.22)$$

The energy loss due to the vibrational excitation of molecular nitrogen may be described as [*Rodriguez*, 1994, and references therein]:

$$L_{\text{vib}}(\text{e}, \text{N}_2) = \frac{4.79 \times 10^{-37} N_e N_{\text{N}_2}}{T_e - T_0} \exp\left(f \frac{T_e - 2000}{2000 T_e}\right) \left[1 - \exp\left(-g \frac{T_e - T_0}{T_e T_0}\right)\right] \frac{\text{W}}{\text{K}} \quad (2.23)$$

where  $f$  is a dimensionless parameter given by:

$$f = 1.06 \times 10^4 + 7.51 \times 10^3 \tanh[0.0011(T_e - 1800)] \quad (2.24)$$

and  $g$  is a dimensionless parameter given by:

$$g = 3300 + 1.233(T_e - 1000) - 2.056 \times 10^{-4}(T_e - 1000)(T_e - 4000) \quad (2.25)$$

The expression for the electron energy loss due to the excitation of vibrational modes in molecular oxygen is [*Rodriguez*, 1994, and references therein]:

$$L_{\text{vib}}(\text{e}, \text{O}_2) = \frac{8.32 \times 10^{-38} N_e N_{\text{O}_2}}{T_e - T_0} \exp\left(f \frac{T_e - 700}{700 T_e}\right) \left[1 - \exp\left(-2700 \frac{T_e - T_0}{T_e T_0}\right)\right] \frac{\text{W}}{\text{K}} \quad (2.26)$$

where

$$f = 3300 - 839 \sin[0.000191(T_e - 2700)] \quad (2.27)$$

The analysis presented by *Rodriguez* [1994] examined the maximum electron temperature modification in the ionosphere using a VLF transmitter. The power radiated by the transmitter was taken to be either ON or OFF. That being the case, the total electron energy loss rate  $L(T_e, T_0)(T_e - T_0)$  played a major role in determining the maximum ionospheric temperature modification in Equation (2.5): for  $dT_e/dt = 0$ , the total electron energy loss rate exactly balances the energy absorbed from the

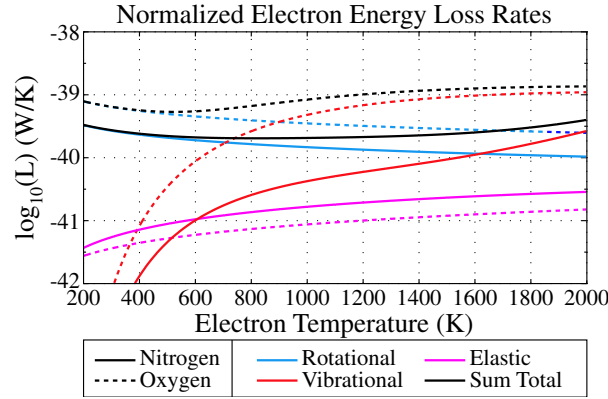


Figure 2.3: Electron energy loss rates due to elastic collisions as well as the rotational and vibrational excitation of molecular nitrogen and molecular oxygen.

heating electromagnetic wave. In the case of modulated heating, however, the actual temporal variation of the electron temperature (e.g., the rate of change of  $T_e$  with time) is very important for the calculation of the total change in conductivity as well as the relative magnitude of the harmonics generated.

The approximate rate of electron temperature recovery is determined by the loss rates per unit Kelvin as listed above. Figure 2.3 shows the normalized electron energy loss rates per unit Kelvin, assuming an ambient electron temperature of 200 K. The loss rates have been normalized by the electron density  $N_e$ , and the respective neutral density  $N_{N_2}$  or  $N_{O_2}$ . At low electron temperatures above the ambient value, the total electron energy loss rates decrease as the electron temperature increases, as indicated in Figure 2.3. This variation with electron temperature indicates that as the HF heating increases the electron temperature above the ambient value (but still below  $\sim 1000$  K), the rate of recovery toward ambient values during transmitter OFF times decreases. The end result is a less-effective modulation of the ionospheric electron temperature at altitudes where the recovery rates are not large enough for the electron temperature to fully recover to the ambient level during transmitter OFF periods. At higher electron temperatures, the electron energy loss rates begin to increase due to the effects of vibrational excitation of oxygen molecules. The higher electron energy loss rates indicate that the electron temperature may be more effectively modulated at certain altitudes due to the faster rate of electron temperature recovery. At the

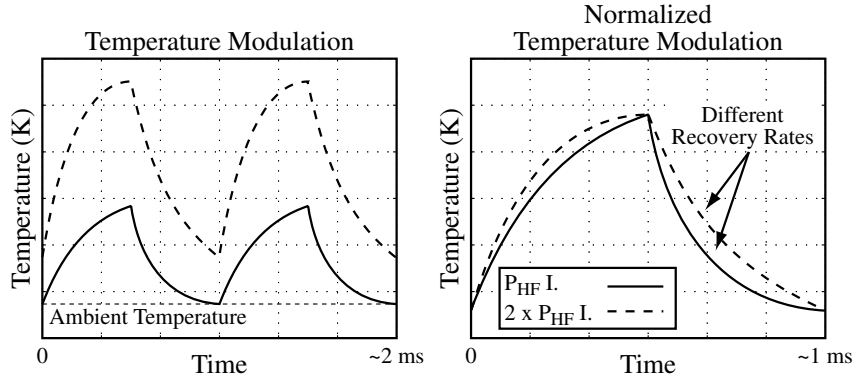


Figure 2.4: Cartoon: Electron energy loss rate effect on temperature modulation as a function of peak HF power level.

same time, a higher electron energy loss rate works against electron temperature enhancement during the heating portion of the modulation cycle, possibly resulting in some cases in an overall reduction of the magnitude of the temperature modulation.

While the HF power level dependence of the electron energy loss rates (via electron temperature) is apparent from Figure 2.3, it is not readily apparent how the electron energy loss rates may affect a change in the relative levels of the harmonic amplitudes as a function of HF power level. The modulated electron temperature resulting from HF heating at two different power levels, shown in Figure 2.4, indicates that although an increase in HF power level may increase the rise-time of the electron temperature waveform, the higher electron temperatures thus attained result in a decrease in the rate of recovery during the transmitter OFF period. Such a variation changes the relative magnitudes of the fundamental modulation frequency and its harmonics. The left-hand panel of Figure 2.4 also depicts the scenario in which doubling the peak HF power level results in less than doubling of the temperature modulation amplitude, due to a decrease in the electron energy loss rates at higher temperatures.

The analyses performed in Chapters 3 and 4 use a linearized version of Equation (2.5) in order to delineate between linear and nonlinear effects of the electron energy loss rates. Model runs evaluating the ionospheric response to HF heating using linearized electron energy loss rates are compared to those performed using linearized HF self-absorption effects in order to evaluate which effect dominates the nonlinear

variations observed. In order to linearize the effects of the electron energy loss rates, the following formula is applied at each altitude instead of Equation (2.5):

$$\frac{3}{2}N_e\kappa_B\frac{dT_e}{dt} = 2k\chi(T_e)S - \overline{L(T_e, T_0)}(T_e - T_0) \quad (2.28)$$

where  $\overline{L(T_e, T_0)}$  is the average energy loss rate for the localized temperature range calculated using the full HF heating model employing Equation (2.5). This average electron energy loss rate,  $\overline{L(T_e, T_0)}$ , is still altitude-dependent. Equation (2.28) enacts a scenario in which the recovery of the modified electron temperature depends linearly on the deviation of the electron temperature from the ambient value. Similar to the case of the linearized self-absorption effect, the electron energy loss factors are not based solely on the ambient ionospheric parameters, but instead represent the average energy loss rates created under modulated HF heating conditions. It is readily apparent that with a slight adjustment to Equation (2.28), each loss rate may be linearized individually. Model runs evaluating the ionospheric response using individually-linearized electron energy loss rates are also used in Chapters 3 and 4 to evaluate which among the six electron energy loss rates employed dominates the nonlinear variations observed.

The cumulative result of the effects described is the modulation of the electron temperature as illustrated in Figure 2.5, which shows the electron temperature as a function of altitude and time, using ambient electron density Profile III, an HF frequency of 3.25 MHz, and a peak HF power of 960 kW. Each colored trace represents a snapshot of the electron temperature as a function of altitude at an instant in time within the steady-state modulation period. The difference in time between each snapshot is  $1/18^{th}$  of the 0.5 ms modulation period. Also shown are the ambient electron temperature as a function of altitude and the HF-modified electron temperature under unmodulated (DC) heating conditions. The modulated electron temperatures that result from sinusoidal amplitude modulation at 2 kHz clearly lie between the ambient and unmodulated heating traces. At lower altitudes (i.e., below  $\sim 70$  km), the modified electron temperature fully recovers to its ambient value during each modulation cycle. At higher altitudes, however, the electron energy loss rates have decreased

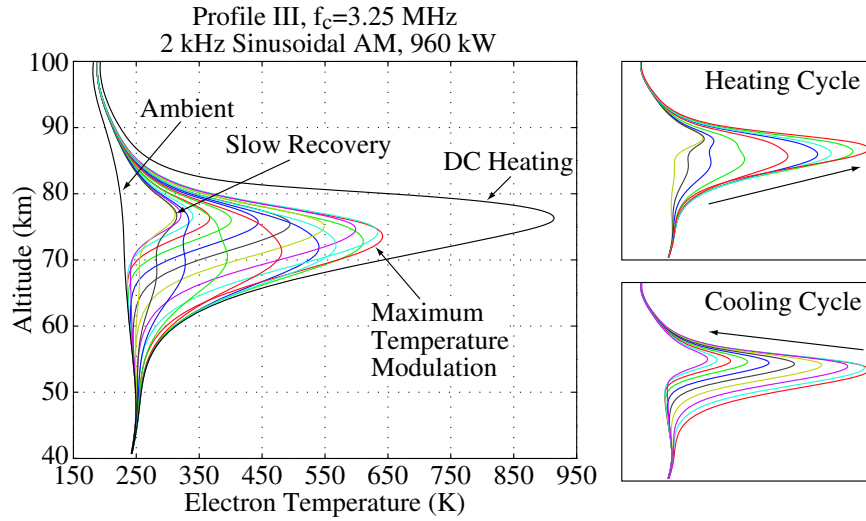


Figure 2.5: Model electron temperature variations for HF heating at 3.25 MHz, 960 kW, 2 kHz sinusoidal AM. Electron density Profile III is employed.

to the point that the electron temperature does not recover fully during the cooling period (see the altitudes labelled ‘Slow Recovery’). It is also evident from Figure 2.5 that the effect of modulating the HF wave limits the maximum electron temperature at each altitude to that attained during the unmodulated (DC) heating case. In fact, at altitudes above  $\sim 70$  km, modified temperatures achieved during modulated heating are significantly lower than those reached during DC heating. Having accounted for each of these effects, we now calculate the variation in conductivity as a function of time and space that results from the modulation of electron temperature.

### 2.3 Modulated Ionospheric Conductivity

The conductivity of the ionosphere depends on both the ambient as well as the modified ionospheric parameters. In an isotropic lossy medium, the conduction current density is in the direction of the electric field, i.e.,  $\mathbf{J} = \sigma\mathbf{E}$ , where the conductivity,  $\sigma$ , is scalar. In a magnetized plasma, such as the  $D$ -region ionosphere, the direction and magnitude of the current densities generated depend on the direction of the electric field relative to that of the ambient magnetic field. In such a case, the conductivity

$\overline{\overline{\sigma}}$  is a tensor quantity, as indicated by the double bars. The result is that an electric field in one direction may generate a conduction current in a different direction. If we align our system so that the  $\hat{\mathbf{z}}$  direction is along the Earth's magnetic field, the conductivity tensor may be expressed as:

$$\overline{\overline{\sigma}}_e = \begin{bmatrix} \sigma_P & -\sigma_H & 0 \\ \sigma_H & \sigma_P & 0 \\ 0 & 0 & \sigma_{\parallel} \end{bmatrix} \quad (2.29)$$

where  $\sigma_P$  is known as the Pedersen conductivity,  $\sigma_H$  is known as the Hall conductivity, and  $\sigma_{\parallel}$  is known as the Parallel conductivity [Bittencourt, 1995, p. 246]. Expressions for each of the Hall, Pedersen, and Parallel conductivities may be found by solving a linearized momentum transfer equation [Bittencourt, 1995, p. 634]. These solutions are well-known in the case that the effective electron-neutral collision frequency is independent of the electron velocity [e.g., see Bittencourt, 1995, p. 639]:

$$\sigma_P = \frac{N_e q_e^2}{m_e} \left[ \frac{\nu + j\omega}{(\nu + j\omega)^2 + \omega_{ce}^2} \right] \quad (2.30)$$

$$\sigma_H = \frac{N_e q_e^2}{m_e} \left[ \frac{\omega_{ce}}{(\nu + j\omega)^2 + \omega_{ce}^2} \right] \quad (2.31)$$

$$\sigma_{\parallel} = \frac{N_e q_e^2}{m_e} \left[ \frac{1}{\nu + j\omega} \right] \quad (2.32)$$

where  $q_e$  is the charge of an electron,  $m_e$  is the mass of an electron, and  $\omega$  is the angular frequency of the wave, which in our case is zero for the essentially constant electrojet electric field,  $\mathbf{E}_0$ .

HF heating of the ionosphere, however, relies on the fact that the electron-neutral collision frequency is temperature-dependent, and thereby electron velocity-dependent. *Tomko* [1981] presents an excellent derivation of the conductivity expressions for this case:

$$\sigma_{\text{P}} = \frac{4\pi}{3} j \frac{q_e^2}{m_e \omega} \int_0^\infty \frac{U}{U^2 - Y^2} v_e^3 \frac{\partial f_{e,0}}{\partial v_e} dv_e \quad (2.33)$$

$$\sigma_{\text{H}} = \frac{-4\pi}{3} \frac{q_e^2}{m_e \omega} \int_0^\infty \frac{Y}{U^2 - Y^2} v_e^3 \frac{\partial f_{e,0}}{\partial v_e} dv_e \quad (2.34)$$

$$\sigma_{\parallel} = \frac{4\pi}{3} j \frac{q_e^2}{m_e \omega} \int_0^\infty \frac{1}{U} v_e^3 \frac{\partial f_{e,0}}{\partial v_e} dv_e \quad (2.35)$$

where  $U = 1 - jZ$  and  $v_e$  is the electron thermal velocity. The conductivity equations above may be evaluated using the following expression for the electron energy distribution function, which is assumed to remain Maxwellian throughout the HF heating process:

$$f_{e,0} = N_e \left( \frac{m_e}{2\pi\kappa_B T_e} \right)^{3/2} \exp\left( \frac{-m_e v_e^2}{2\kappa_B T_e} \right) \quad (2.36)$$

For the constant  $\nu$  case, Equations (2.34)-(2.35) may be evaluated directly and reduce to Equations (2.31)-(2.32). For the case where  $\nu$  is proportional to  $v_e^2$ , Equations (2.34)-(2.35) may be solved numerically given the ambient ionospheric parameters and the electron temperature. Using electron density Profile III, the Hall, Pedersen, and Parallel conductivities at an altitude of 76 km are shown (for both the standard, constant  $\nu$ , case and the kinetic,  $\nu(v) \propto v_e^2$ , case) as a function of electron temperature in Figure 2.6. Although the two cases are not dramatically different for the temperature ranges encountered in this dissertation (i.e.,  $< \sim 1000$  K), we will use the kinetic expressions for conductivity, assuming  $\nu(v) \propto v_e^2$ , in order to be consistent with our calculation of HF absorption rates using the same assumption.

It is readily apparent from Figure 2.6 that each of the three conductivities is a nonlinear function of electron temperature. In Chapters 3 and 4 of this dissertation, we analyze the effects of the nonlinear temperature dependence of the conductivity equations. Instead of linearizing the conductivity equations, however, we fully linearize Equation (2.5) and attribute the nonlinearities which persist to the conductivity

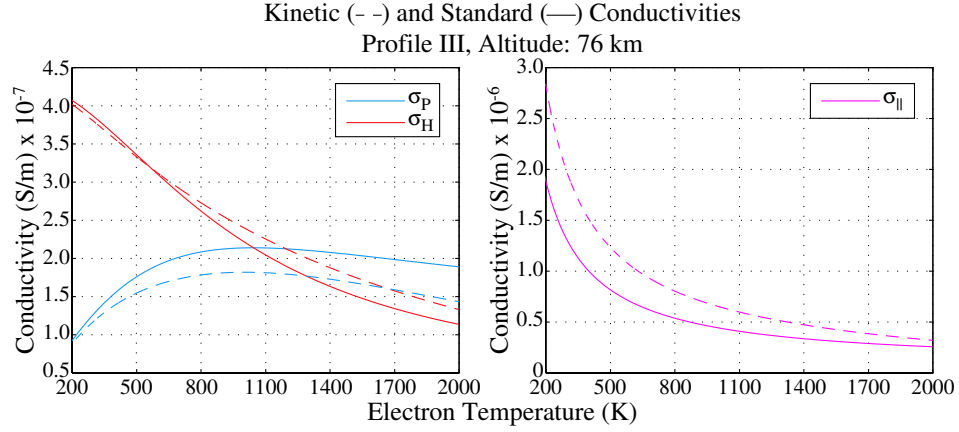


Figure 2.6: Dependence of Hall, Pedersen, and Parallel conductivities on electron temperature at an altitude of 76 km using electron density Profile III.

equations:

$$\frac{3}{2}N_e\kappa_B\frac{dT_e}{dt} = 2k\overline{\chi(T_e)}S - \overline{L(T_e, T_0)}(T_e - T_0) \quad (2.37)$$

Equation (2.37) enacts a scenario in which the recovery of the modified electron temperature depends linearly on the deviation of the electron temperature from the ambient value. In addition, the rate of absorption at each altitude is taken to be constant with time. Forcing an entirely linear variation in temperature allows for the delineation of the nonlinearities associated with the conductivity equations.

## 2.4 ELF/VLF Wave Generation

It is well-known in classical electrodynamic theory that a time-varying current density  $\mathbf{J}$  produces a magnetic field,  $\mathbf{B}$ , at a receiver distant from the source location. The magnetic field may be derived from the so-called vector potential  $\mathbf{A}$  which, for time-harmonic wave propagation in free-space may be expressed as [*Balanis*, 1982, p. 87]:

$$\mathbf{A}(\mathbf{r}) = \frac{\mu}{4\pi} \int_{V'} \mathbf{J}(\mathbf{r}') \frac{e^{-jkR}}{R} dv' \quad (2.38)$$

where  $\mathbf{r}$  is the location of the receiver,  $\mathbf{r}'$  is the location of the infinitesimal element,  $dv'$ , within the radiating volume,  $V'$ ,  $k$  is the free-space propagation constant of the wave ( $\omega/c$ ), and  $R = |\mathbf{r} - \mathbf{r}'|$ . The magnetic field measured at the receiver may then simply be calculated from the vector potential:

$$\mathbf{B}(\mathbf{r}) = \nabla_r \times \mathbf{A}(\mathbf{r}) = \frac{\mu}{4\pi} \int_{V'} |\mathbf{J}(\mathbf{r}')| \left( \nabla_r \times \frac{e^{-j\beta|\mathbf{r}-\mathbf{r}'|}}{|\mathbf{r}-\mathbf{r}'|} \hat{\mathbf{J}}(\mathbf{r}') \right) dv' \quad (2.39)$$

where  $\hat{\mathbf{J}}(\mathbf{r}')$  is the unit vector in the direction of the current density  $\mathbf{J}(\mathbf{r}')$ .

The curl expression in Equation (2.39) is a Green's function for wave propagation in free-space. This portion of the  $\mathbf{B}$ -field expression may be altered to account for the boundary conditions of specific scenarios. In our case, the electromagnetic boundaries of the system consist of the lossy Earth at the base of the Earth-ionosphere waveguide and the anisotropic, lossy ionospheric plasma at the top of the waveguide ( $\sim 60$ - $100$  km altitude). The Green's function for this situation is quite complex and is not modeled in this dissertation. The Green's function for propagation in the Earth-ionosphere waveguide depends on the altitude and orientation of the radiating element, the distance to the receiver, and the plasma parameters between the radiating element and the receiver. For receivers relatively close to the source region (e.g.,  $< 200$  km), this Green's function must also account for the effect of multiple reflections between the Earth and ionosphere, such as those pulses observed by *Rietveld and Stubbe* [1987] and *Papadopoulos et al.* [2003]. At farther distances, the Green's function must account for the excitation of propagating waveguide modes, such as those directly observed by *Barr et al.* [1986] at a ground-distance of  $\sim 500$  km. It is not the purpose of this work to express this Green's function describing wave propagation within the Earth-ionosphere waveguide, but we instead label this nebulous function  $G_{\text{EI}}(\mathbf{r}, \mathbf{r}')$  and examine the resulting  $\mathbf{B}$ -field as a function of HF power. The time-harmonic expression for the magnetic flux density then becomes:

$$\mathbf{B}(\mathbf{r}) = \frac{\mu}{4\pi} \int_{V'} |\mathbf{J}(\mathbf{r}')| G_{\text{EI}}(\mathbf{r}, \mathbf{r}') dv' \quad (2.40)$$

where  $\mathbf{J}(\mathbf{r}') = \overline{\sigma_e}(\mathbf{r}') \cdot \mathbf{E}_0$ .

In order to study the generation of ELF/VLF waves as a function of HF power level, we assume that  $G_{\text{EI}}$  depends only on the ambient ionospheric parameters (i.e., that it is unaffected by HF heating). Variations in the amplitude of the received **B**-field  $\mathbf{B}(\mathbf{r})$ , as a function of HF power level may thus be attributed to variations in the amplitude of the current density  $\mathbf{J}(\mathbf{r}')$  as a function of HF power. Furthermore, because we cannot explicitly evaluate Equation (2.40) without knowledge of  $G_{\text{EI}}$ , we instead calculate the time-variation of the conductivity as a function of space and evaluate the amplitude of that variation as a function of HF power. We assume there to be a single point within the HF-heated region that dominates the variation in amplitude as a function of power. This point need not coincide with the altitude of the maximum conductivity modulation amplitude; for example, waveguide excitation factors, which are sensitive to the altitude and orientation of the source, may be less than maximum at the peak conductivity modulation altitude [*Barr and Stubbe*, 1984a]. We then seek to find a variation in the amplitude of the conductivity modulation with HF power that matches observations of the **B**-field on the ground, and that is within several kilometers of the altitude with the maximum conductivity modulation amplitude. For the observations presented in this dissertation, it suffices to calculate the conductivity modulation as a function of altitude in the vertical direction only. However, the dominant variation in conductivity amplitude should be evaluated over the entire 3-dimensional HF-heated region.

## Chapter 3

# ELF/VLF Amplitude Saturation

In this chapter, we present detailed observations of the onset of amplitude saturation in ELF/VLF waves generated by modulated HF heating of the auroral electrojet current system. Broadband ELF/VLF measurements at a ground-based receiver located near the HAARP HF transmitter exhibit variations in signal amplitude which are qualitatively consistent with a hard-limiting approximation of the saturation process. A method to approximate the saturation curve as a function of HF power from experimental data is presented, and the results indicate that a  $\sim 5\text{-}10\%$  reduction in generated ELF signal amplitude is typical at the maximum radiated HF power level (771 kW) for modulation frequencies between 1225 Hz and 3365 Hz. For HF transmissions using sinusoidal amplitude modulation, the saturation dominantly affects the second harmonic of the generated ELF/VLF signal, with amplitudes on average 16% lower than expected at the maximum HF power level. Observations are compared with the predictions of the HF heating model described in Chapter 2 in order to attribute the observations to physical processes. The observations and results presented in Sections 3.1, 3.2, and 3.3 have been previously published in [Moore *et al.*, 2006].

### 3.1 Description of the Experiment

The experiment reported herein was conducted at the HAARP facility between July 30 and August 2, 2004, under both daytime and nighttime ionospheric conditions. Quiet geomagnetic conditions persisted throughout the majority of the campaign: the  $K_p$  index varied between 1 and 2<sup>+</sup> during transmission hours, and the absolute value of any component of the fluxgate magnetometer located in Gakona, AK exceeded 50 nT during only three of the thirty-two hours of transmission. The HAARP HF transmitter broadcast at 3.25 MHz with X-mode polarization five twelve-second-long sinusoidal amplitude modulation periods at each of the frequencies, 1225, 1875, 2125, 2375, and 3365 Hz, while stepping the modulated HF power linearly from 0 W to 771 kW (radiated power) in twelve one-second long steps, as shown in Figure 3.1. This sequence was repeated eight times per hour for eight hours per day. The HF beam was directed vertically for all transmissions. The input HF power at the HAARP facility (960 kW) is similar to the total power available for the Tromsø experiments (1.08 MW) [Barr and Stubbe, 1991a]. The equipment and system related nonlinear characteristics associated with the transmission of a sinusoidally-modulated HF signal have been directly measured at the HAARP HF transmitter and are accounted for in this analysis.

The data presented in this chapter were acquired using an ELF/VLF receiver located in Chistochina, Alaska ( $\sim 36$  km from the HAARP facility at  $62.61^\circ$  N,  $144.62^\circ$  W). The receiver utilizes two orthogonal  $4.8 \times 4.8$  m<sup>2</sup> air-core loop antennas oriented to detect the horizontal components of the wave magnetic field on the ground, a preamplifier located near the antennas, and a line-receiver and data recording system located  $\sim 600$  meters from the antennas in order to reduce the effects of electromagnetic noise associated with 60 Hz hum and its harmonics. Both receiver channel inputs have RFI-suppression units to reduce interference from differential signals at frequencies above 100 kHz, including the HF band. The analog receiver channel outputs are anti-alias filtered at 40 kHz (using an 8-pole Chebyshev filter) and sampled at 100 kHz with 16-bit resolution. In post processing, the amplitude values associated with individual frequencies are extracted using a 10-Hz bandwidth FIR

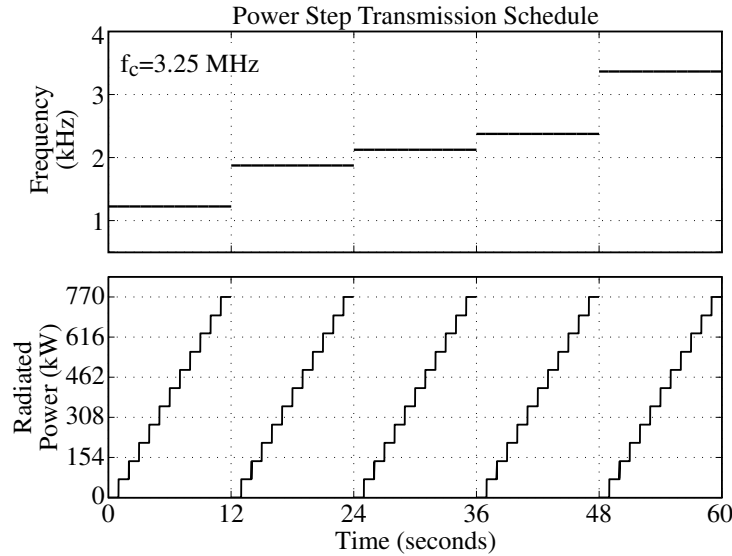


Figure 3.1: HAARP transmission schedule for the power-step experiment.

filter and decimated to 20 ms resolution. The amplitude values associated with each power step are extracted by taking the median value over the period of transmission in order to mitigate the effects of impulsive ‘noise’ signals, such as those introduced by lightning strokes in the form of radio atmospherics.

The Stanford University ELF/VLF receiver equipment used at Chistochina and other sites has been rigorously tested in order to establish that the ELF/VLF signals received were not artificially created in the receivers by non-linear demodulation of the HF sky wave arriving at the site. Two possible electronic couplings are of particular interest: coupling via common-mode signals, and coupling via differential-mode signals. While injected common-mode signals at 1.6 MHz were reduced by 40 dB compared to signals at 1 kHz, common-mode signals at higher frequencies were too small to be measured. Additionally, differential-mode signals measured at 1 MHz were reduced by 40 dB from the 1 kHz value. Higher frequency differential-mode signals were also too small to measure accurately.

The nature of the ELF/VLF data collected using these systems also suggests that nonlinear demodulation of the HAARP HF sky wave signal does not significantly contribute to the ELF/VLF signals received. For example, no modulation

sidebands are observed to be produced by any of the strong VLF transmitting stations (in the 15-25 kHz range) recorded in the data, although these signals are well inside the flat-response region of our preamplifiers and their intensities are typically much stronger (by  $\sim 10$  dB or more) compared to the HAARP generated ELF/VLF signals. Similarly, natural signals (whistlers and strong emissions) observed during times of observations of HAARP ELF/VLF signals (often at intensities well above the HAARP-generated signals) do not exhibit any harmonic content or any evidence for receiver saturation or other nonlinearities.

Together, these considerations strongly suggest that the ELF/VLF signals observed at each ELF/VLF receiver are indeed generated by modulated heating of the auroral electrojet currents, rather than by nonlinear demodulation of the HF sky wave in the receiver electronics.

## 3.2 ELF/VLF Amplitude Saturation at 1225 Hz

The 12-second-long power-step transmission pattern was repeated a total of 256 times for each modulation frequency over the four-day period of the experiment. We first report observations at 1225 Hz due to the generally higher signal-to-noise ratio (SNR) available for each of the first three harmonics.

### 3.2.1 Experimental Observations

Figure 3.2 shows the ELF/VLF signal amplitude at 1225 Hz and its second and third harmonics during three successive power-step periods with good (i.e.,  $> 10$  dB) signal-to-noise ratio (SNR) at all three frequencies. The variation of amplitude with radiated power shown in Figure 3.2 holds throughout the data set when the signal amplitudes are observed to be above the noise floor; i.e., the amplitude of the fundamental component (first harmonic) approximately conforms to a power-law dependence on radiated HF power; the amplitude of the second harmonic also appears to follow a power-law variation until it reaches a peak and subsequently begins to decrease with increasing radiated HF power; and the amplitude of the third harmonic rises above the

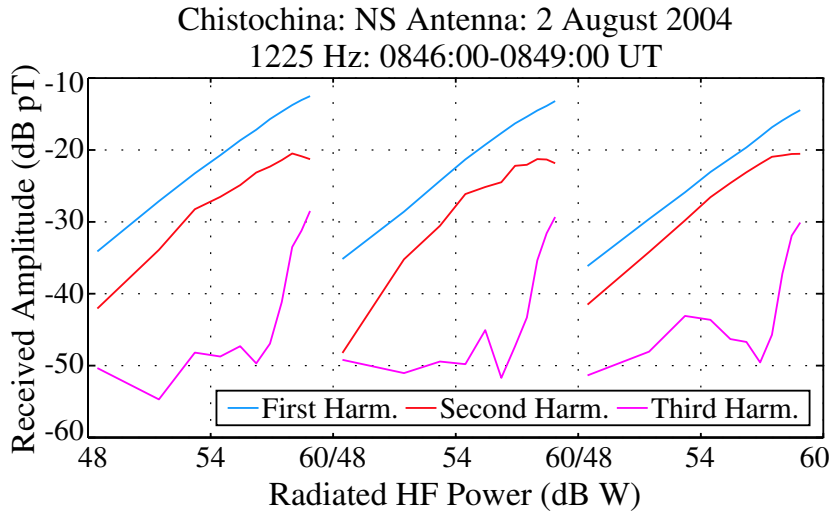


Figure 3.2: Amplitude of the first, second, and third harmonics observed during three successive power step transmissions on 2 August 2004.

noise when the amplitude of the second harmonic begins to significantly deviate from a power-law variation. In all cases where the third harmonic amplitude is observed with  $\text{SNR} > 10$  dB, it emerges from the noise ( $\approx -50$  dB pT) with a slope significantly larger than the first and second harmonics, as shown in Figure 3.2. However, the third harmonic is only observed with significant SNR for modulation frequencies of 1225 and 1875 Hz, due to the generally higher noise floors (primarily due to radio atmospherics) at the third harmonics of the higher modulation frequencies. It should be noted that our observations are not inconsistent with those of *Stubbe et al.* [1982], who show that a 0-50% power modulated waveform generates more ELF signal than a 50-100% power modulated waveform, despite having the same modulation depth.

Although the amplitudes of the third harmonics during this 4-day data set seldom exhibit SNR levels  $> 10$  dB, the first and second harmonic amplitudes are observable at high SNR levels on a regular basis. The panels of Figure 3.3 show the campaign-averaged signal levels (i.e., signal levels simply averaged over more than 250 cases of individual observations without regard to local time) observed on the North-South antenna at Chistochina for each modulation frequency and its second harmonic. The second harmonic of the 3365 Hz tone is the only signal whose amplitude does not

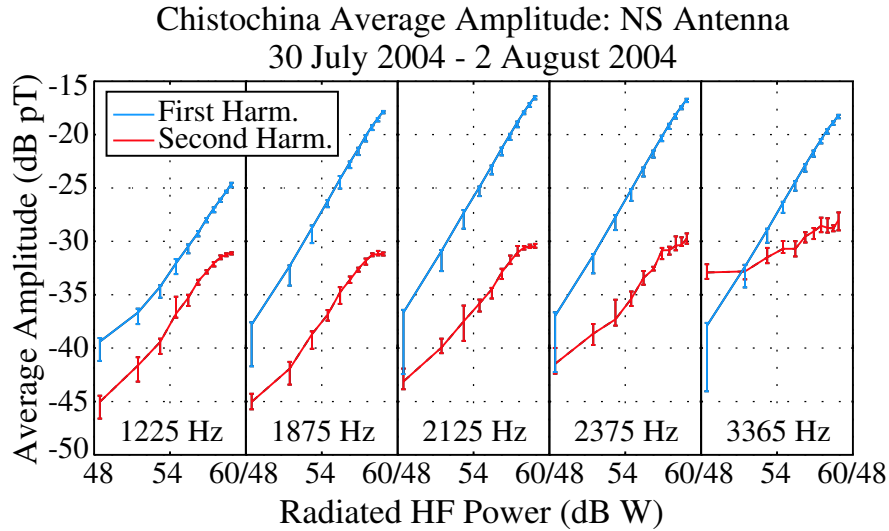


Figure 3.3: The campaign-averaged amplitude variations at each modulation frequency and second harmonic.

rise significantly ( $> 10$  dB) above the noise floor on average. Similar variations are observed on the East-West antenna. It is evident from Figure 3.3 that the variations observed under high SNR conditions shown in Figure 3.2 are generally representative of the variation of ELF/VLF amplitude with radiated HF power.

### 3.2.2 Hard-Cap Approximation

The power-law relationship between the amplitude of the observed ELF/VLF signal,  $A_{\text{ELF}}$ , and the radiated HF power has been previously noted by *Papadopoulos et al.* [1990] and *Barr and Stubbe* [1991a] and expressed as:

$$A_{\text{ELF}} \propto A^{n-1} (\overline{P_{\text{HF}}})^n \quad (3.1)$$

where  $A$  is the area of the HF heated region,  $\overline{P_{\text{HF}}}$  is the peak HF power, and  $n$  is an empirically determined power factor. In previous work, the value of  $n$  has been determined to vary between 0.5 and 1.1 [*Barr and Stubbe*, 1991a, and references therein]. While the value of  $n$  may be greater than or less than 1, the term ‘saturation’ is used herein to describe only the circumstance when experimentally observed ELF/VLF

amplitudes are *less than* that predicted by this power-law variation.

Equation (3.1) may be generalized in the following manner to account for a time-varying  $P_{\text{HF}}(t)$  and to provide the amplitudes of all frequencies of interest at the same time:

$$A_{\text{ELF}}(\omega) = k(\omega) |\text{DFT}\{(P_{\text{HF}}(t))^n\}| \quad (3.2)$$

where  $\omega$  is the angular ELF/VLF frequency,  $\text{DFT}\{\cdot\}$  is the Discrete Fourier Transform operator, and  $k(\omega)$  is a factor that here incorporates the dependence of the ELF amplitude on the area of the heated ionospheric region and that is expected to vary with frequency due to the dependence of the ELF amplitude on such factors as the ionospheric heating and cooling time constants [*Papadopoulos et al.*, 2003].

For the specific case of ideal sinusoidal amplitude modulation with a modulation depth of 100% and with a radiated HF power normalized to 1 W, Equation (3.2) may be re-expressed in the following manner:

$$A_{\text{HF}}(t) = \frac{1}{2} + \frac{1}{2} \cos(\omega t) \quad (3.3)$$

$$P_{\text{HF}}(t) \propto \left[ \frac{1}{2} + \frac{1}{2} \cos(\omega t) \right]^2 = \frac{3}{8} + \frac{1}{2} \cos \omega t + \frac{1}{8} \cos 2\omega t \quad (3.4)$$

$$A_{\text{ELF}}(\omega) = k(\omega) \left| \text{DFT} \left\{ \left[ \frac{3}{8} + \frac{1}{2} \cos \omega t + \frac{1}{8} \cos 2\omega t \right]^n \right\} \right| \quad (3.5)$$

The time variation of the normalized HF power waveform, expressed in Equation (3.4), varies as the square of the sinusoidal amplitude modulation envelope, expressed in Equation (3.3). It can be seen from Equations (3.4) and (3.5) that the second modulation frequency harmonic is present in the radiated HF power waveform, equivalent, in this sense, to the role of the odd modulation frequency harmonics in the case of square-wave modulation. In our numerical analysis, we have accounted for the equipment and system related nonlinearities associated with the HAARP HF transmission as well as the 95% depth of the modulation.

The variations in amplitude that result from the application of Equation (3.5) to the transmitted power-step sequence for  $n = 0.9$  and  $k(\omega) = 1$  are shown in the left panel of Figure 3.4. In this example, the nonlinearities present in the modulation envelope of the transmitted HF waveform are apparent in the deviation from

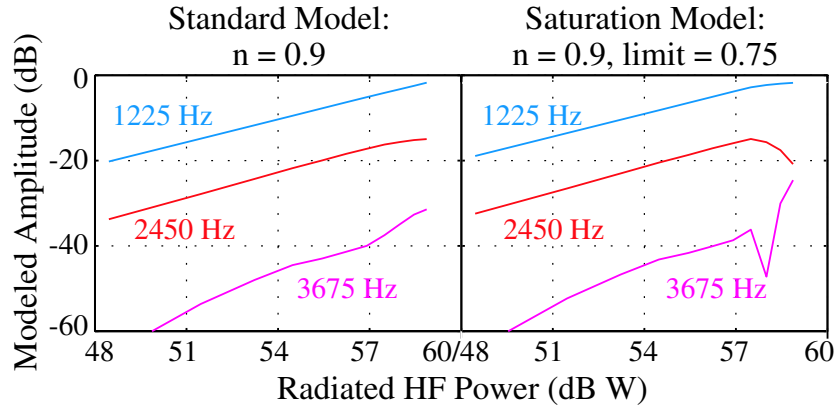


Figure 3.4: Modeled amplitude variation for the first, second, and third harmonics. Left Panel: Saturation effects are omitted. Right Panel: a hard-limiting saturation effect is included.

strictly power-law behavior. The variations in amplitude that result from employing a  $0^{th}$ -order (hard-limiting) saturation process to limit the HF power at 75% of the maximum value of  $[P_{\text{HF}}(t)]^n$  are shown in the right panel of Figure 3.4. Comparing the experimental observations shown in Figure 3.2 with the strong deviation of the second harmonic from power-law behavior and the abrupt increase in third harmonic amplitude at high HF power levels in Figure 3.4 leads to the conclusion that our simple model which accounts for a saturation process (i.e., deviation from the power-law variation) produces results which qualitatively agree with observations.

### 3.2.3 Extraction of the Saturation Function

Although a  $0^{th}$ -order (hard-limiting) saturation process appears to qualitatively match the observations, it is unlikely that ionospheric HF absorption physically entails such hard-limiting saturation. In this section, we approximate the saturation function based on experimental data. The expression for the ELF/VLF amplitude resulting from a given radiated HF power variation, incorporating the saturation model is:

$$A_{\text{ELF}}(\omega) = k(\omega) |\text{DFT}\{(P_{\text{HF}}(t))^n f_{\text{sat}}[P_{\text{HF}}(t)]\}| \quad (3.6)$$

where  $f_{\text{sat}}(\cdot)$  is the saturation function to be determined.

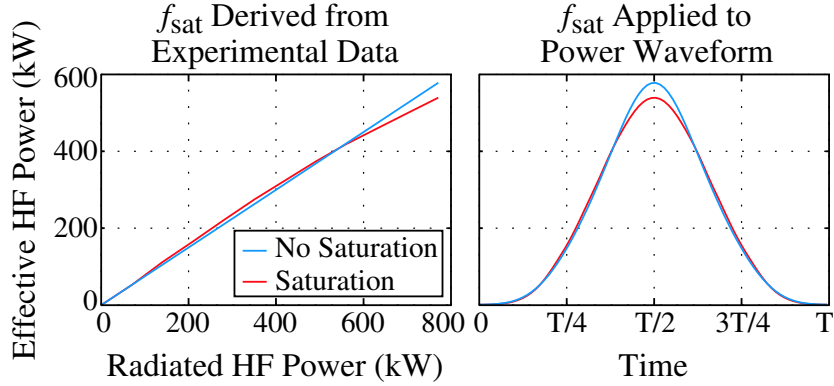


Figure 3.5: Left Panel: The saturation function derived from experimental data and the variation expected from omitting saturation effects. Right Panel: One period,  $T$ , of the instantaneous HF power waveform before and after the application of the saturation function.

In order to find an empirical form for  $f_{\text{sat}}(\cdot)$ , we first determine the value of  $n$  which best fits the variation in amplitude of the first harmonic in a least-square-error sense. The comparison of the modeled first harmonic amplitudes shown in Figure 3.4 indicates that the first harmonic is largely unaffected by the saturation process until the last two power steps and thus provides our best measurement of  $n$ . By neglecting the amplitudes observed during the last two power steps, we may extract  $n$  from the observed variation of the amplitude of the first harmonic. Using this technique, 64% of the  $n$ 's calculated for the 256 different observations at each of the five ELF/VLF modulation frequencies throughout the campaign fell between .95 and 1.05. It should be noted that neglecting the amplitudes observed during the last two power steps produces higher values of  $n$  more than 95% of the time. With an approximation of  $n$  in hand, we then determine the saturation function,  $f_{\text{sat}}(\cdot)$ . We assume that the slight deviation of the first harmonic amplitude from a power-law dependence on HF power may be attributed to the saturation function:

$$f_{\text{sat}}(m+1) = \left[ \frac{A_{\text{ELF}}(m+1) \overline{P_{\text{HF}}(m)}^n}{A_{\text{ELF}}(m) \overline{P_{\text{HF}}(m+1)}^n} \right] f_{\text{sat}}(m) \quad (3.7)$$

where  $m$  is the index of the power step sequence. The values determined for  $f_{\text{sat}}$ ,

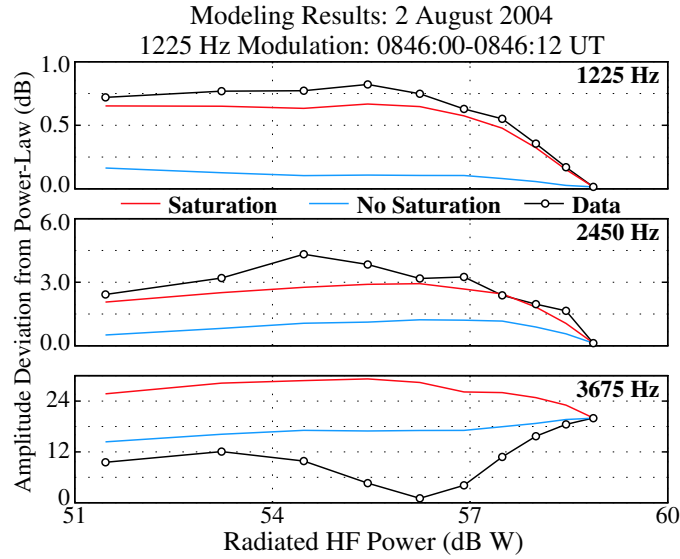


Figure 3.6: Comparison of the modeling results including and omitting saturation effects against the example data set. The calculated power-law variation has been divided out of each trace in order to show the deviation from power-law.

assuming that the first (lowest) HF power step does not yet lead to saturation (i.e., deviation from the power-law variation), are then used to model the variation of the first, second, and third harmonic amplitudes using Equation (3.6).

For the first power-step series shown in Figure 3.2, the effective HF power (i.e., the quantity,  $[P_{\text{HF}}(t)]^n f_{\text{sat}}[P_{\text{HF}}(t)]$ ) resulting from the analysis described above is shown in Figure 3.5 as a function of HF power and time. Although the values of the saturation function are allowed to take values above unity, they tend to values less than 1 at high HF power densities, consistent with ‘saturation’, i.e., ELF/VLF values less than those predicted by the power-law dependence.

The resulting variation in amplitude at each frequency is then used to calculate the least-square-error values of  $k(\omega)$ . Figure 3.6 shows the modeled variation in amplitude for our example using both the method described in connection with Equation (3.5) and the method accounting for saturation described by Equation (3.6). In these panels, the calculated power-law variation with HF power has been divided out from each trace to allow for a more detailed inspection of the deviation from power-law behavior. Although amplitude measurements of the second harmonic were not included in

the determination of the saturation function, the middle panel of Figure 3.6 shows a  $\sim 3$  dB decrease in the modeled second harmonic amplitude at high HF power levels, closely matching observations. The bottom panel of Figure 3.6 shows that neither Equation (3.5) nor Equation (3.6) can account for the observed variation of the third harmonic amplitude. However, our model clearly captures the slight deviation from power-law variation in the first harmonic amplitude along with the decrease in second harmonic amplitude at high radiated HF power levels.

For sinusoidal amplitude modulation, the ability to predict the variation of the second harmonic amplitude from the variation of the first harmonic amplitude indicates that the first and second harmonics are produced by the same physical process and that this physical process entails a saturating effect at high HF power levels. The inability of this formulation to predict the third harmonic amplitude variation does not necessarily indicate that the third harmonic is generated by a different physical process than the first two harmonics, however. The formulation of saturation presented herein assumes that the saturation function  $f_{\text{sat}}$  has a one-to-one correspondence with  $P_{\text{HF}}$ . Considering the different ionospheric heating and cooling rates observed, for instance, by *Rietveld et al.* [1986], it is not likely that a one-to-one correspondence encapsulates the physical process that produces high amplitudes at the third harmonic frequency. Nevertheless, this observation is not inconsistent with previous observations, such as those by *Barr et al.* [1999], whose experiments using square-wave modulation indicated that the even harmonics were generated at different altitudes than were the fundamental and the odd harmonics (which for square-wave modulation are present in the transmission waveform).

### 3.3 Average Saturation Levels

The campaign-averaged saturation functions extracted from the entire data set are shown in Figure 3.7 as a function of radiated HF power. Comparing the average daytime and average nighttime curves, the effects of saturation at high HF power levels do not appear to depend on local time, indicating that the saturation process does not strongly depend on the ambient conductivity of the overlying ionosphere which

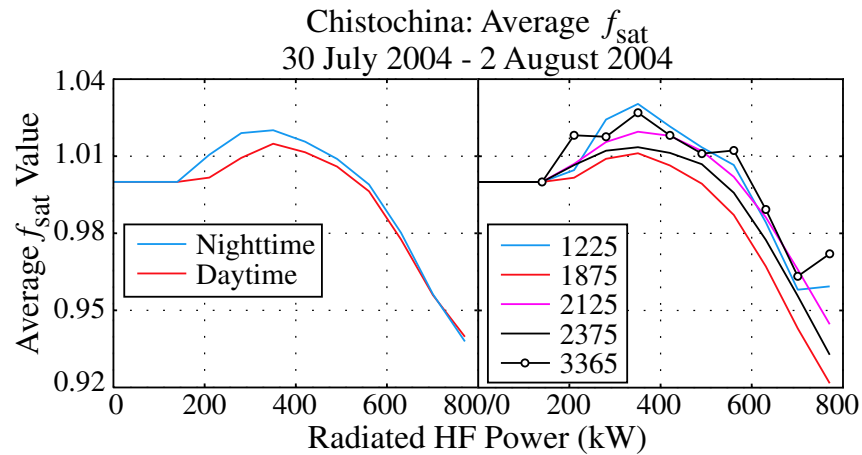


Figure 3.7: Average saturation functions. Left Panel: Average daytime saturation versus average nighttime saturation. Right Panel: A comparison of saturation as a function of modulation frequency.

varies significantly between nighttime and daytime. At the same time, differences between the daytime and nighttime saturation functions exist at lower HF power levels, indicating that low-power probing may possibly reveal evidence on the ambient ionospheric conditions. The right-hand panel of Figure 3.7 shows that, on average, saturation effects reduce the total generated ELF/VLF signal level for all modulation frequencies by 5-10% at the highest radiated HF power level. While the general shape of the saturation function remains the same for all modulation frequencies, there exist small differences between the curves as a function of modulation frequency. Inspection of the saturation function using a larger number of modulation frequencies may reveal more detail. These two panels, together with the fact that the saturation model produces lower total errors than the standard power-law model 93% of the time, indicate that saturation occurs on a regular basis at all modulation frequencies and under both daytime and nighttime conditions. The analysis presented in Chapter 5 further expands on the occurrence rate of ELF/VLF amplitude saturation using much larger data sets.

At the present maximum power level of HAARP and at a carrier frequency of 3.25 MHz with sinusoidal amplitude modulation, the saturation effect typically leads to a second harmonic amplitude which is 16% less than that expected with a power-law

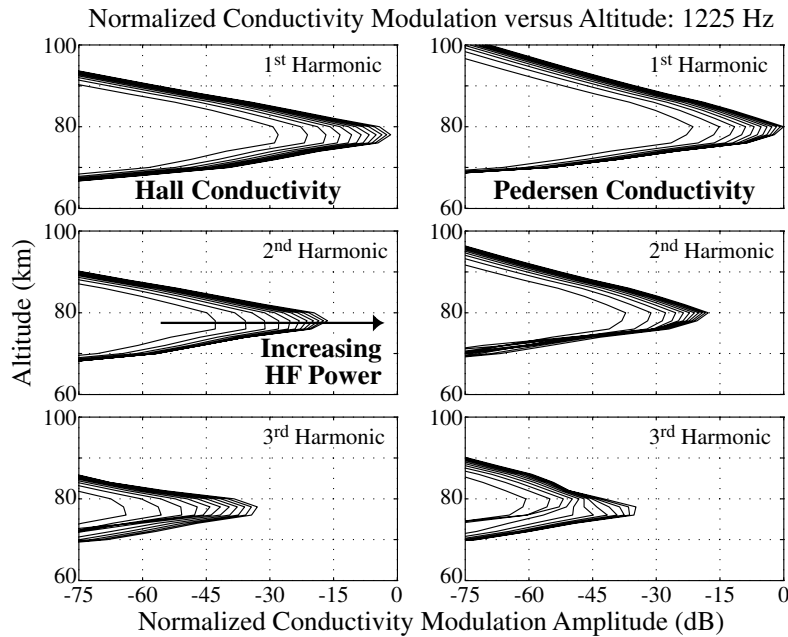


Figure 3.8: Amplitude of model Hall and Pedersen conductivity modulation versus altitude for each of the peak HF power levels employed. The variation of the first three harmonics are modeled using sinusoidal amplitude modulation at 1225 Hz and electron density Profile III.

dependence (of radiated ELF/VLF intensity on HF power) and a sharp 15 dB jump in the amplitude of the third harmonic. An empirical saturation function derived from measurements of the first harmonic amplitude produces results quantitatively consistent with amplitudes of the first and second harmonic frequencies. While a hard-cap saturation process qualitatively agrees with the variation of the third harmonic amplitude, this effect is not reproduced by the smoothly-varying empirical saturation function. For this reason, we now turn our attention to the HF heating model described in Chapter 2 of this work to inspect the first, second, and third modulation frequency harmonics generated as a function of HF power level.

### 3.4 Comparison with HF Heating Model

In this section, we investigate, in the context of the theoretical HF heating model described in Chapter 2, the variation of the Hall and Pedersen conductivity components as a function of HF power and compare the modeled variations with observations. The amplitude of the calculated Hall and Pedersen conductivity modulation resulting from HF heating with a 3.25 MHz X-mode polarized carrier signal, sinusoidally amplitude modulated at 1225 Hz and aimed in the vertical direction is shown in Figure 3.8 as a function of altitude for each HF power level. The conductivity modulation resulting from model runs using ambient electron density Profile III (see Figure 2.1), such as those shown in Figure 3.8 for each HF power level, are consistent in nature with the results of model runs performed using ambient electron density Profiles I and II, although the altitude of maximum conductivity modulation depends on the ambient parameters. In this analysis, we consider the results of the HF heating model using ambient electron density Profile III to be generally representative of the HF power dependence of the physical processes involved in the HF-induced modulation of the ionospheric conductivity. Figure 3.8 shows that for Profile III, the altitude of the maximum Hall conductivity modulation varies between 76 and 78 km, depending on the HF power level, whereas the altitude of the maximum Pedersen conductivity modulation varies between 78 and 80 km. We now investigate the dependence of the amplitude of the conductivity modulation on HF power within  $\sim 5$  km of these altitudes.

The variation in amplitude of the modulated ionospheric conductivity as a function of HF power is shown in Figure 3.9. As was discussed in Chapter 2, the variation of the amplitude of the conductivity modulation at the dominant altitude and dominant radius within the HF-heated region is directly related to the variation in the amplitude of the ELF/VLF signal detected at the receiver. The variations with HF power level in the first, second, and third harmonic amplitudes of the modeled conductivity modulation shown in Figure 3.9 were selected because they roughly match the variations with HF power level in the first, second, and third harmonic amplitude of the observed ELF/VLF signals and because they are located at altitudes within

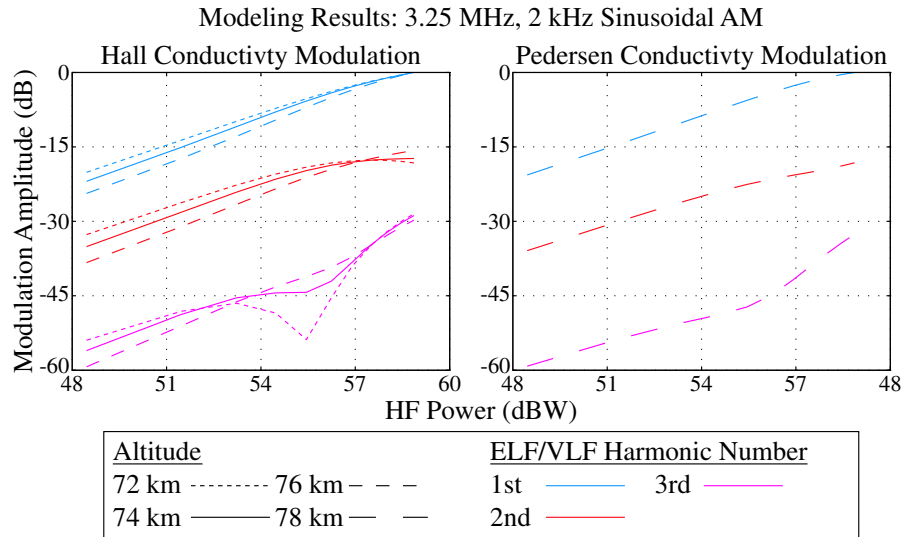


Figure 3.9: Hall and Pedersen conductivity variations with HF power that match observations.

~5 km of the altitude of the maximum modeled conductivity modulation. The left-hand panel of Figure 3.9 shows matching Hall conductivity variations for the first, second, and third harmonic amplitudes. The right-hand panel shows the Pedersen conductivity variation at the one altitude (78 km) that yields conductivity variations matching observations. While only one altitude yields matching Pedersen conductivity variations, several altitudes yield matching Hall conductivity variations, possibly indicating that the Hall conductivity may dominate the Pedersen conductivity in terms of the variations observed at ground-based receivers (due to the larger integration volume). Figure 3.10 provides a side-by-side comparison of the Hall conductivity variation, the Pedersen conductivity variation, and the power-law variation, plotted together with data from Figure 3.2. In this figure, only the conductivity variations that matched observations best are included. It is evident from Figure 3.10 that both the Hall and Pedersen conductivity variations match observations of all three harmonic amplitudes better than the simple power-law variation. In addition, the Hall conductivity variation follows the curve of the second harmonic amplitude at high power levels better than the Pedersen conductivity variation does. Furthermore, it is clear that the sharp increase in third harmonic amplitude is best modeled by the

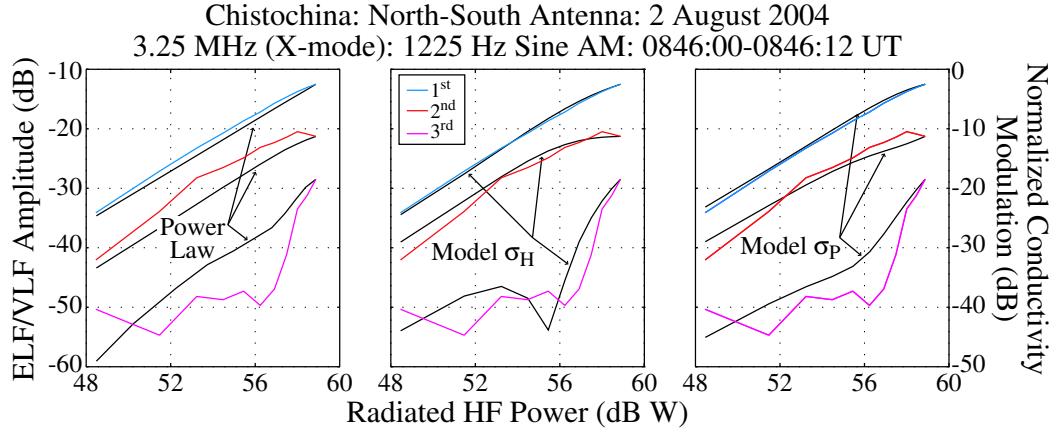


Figure 3.10: Comparison of power-law variations with modeled Hall and Pedersen conductivity variations as a function of HF power level.

Hall conductivity variation. Together, these model runs indicate that the observed ELF/VLF amplitude saturation at ground-based receivers is best modeled by the variation of the Hall conductivity with HF power. We therefore concentrate on the Hall conductivity modulation for the remainder of this analysis.

In order to investigate the physical mechanisms responsible for the onset of ELF/VLF amplitude saturation, we concentrate on the Hall conductivity variation with HF power in the 72-76 km altitude range. As has been shown in the preceding analysis, the Hall conductivity variation in this altitude range matches observations successfully at each of the first three modulation frequency harmonics. We inspect the amplitude variations predicted by the model at both low and high power levels and evaluate the physical processes responsible for the observed variations of each harmonic in turn.

### 3.4.1 The First Harmonic Amplitude

We first examine the variation of the first harmonic amplitude by linearizing, in turn, the effects of self-absorption and the effects of the electron energy loss rates, as described in Chapter 2. By linearizing both effects at the same time, we are able to evaluate the ELF/VLF amplitude dependence on the nonlinear relationship between

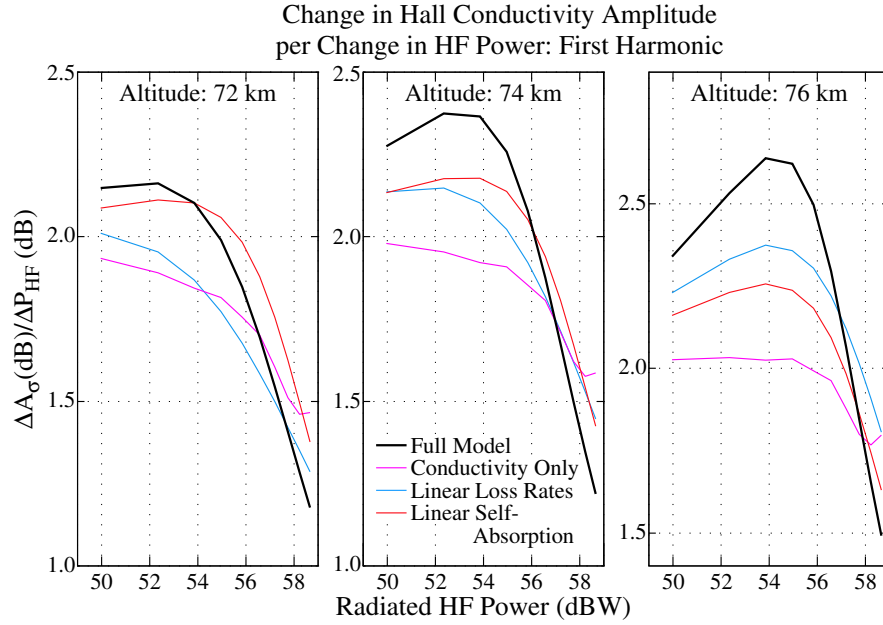


Figure 3.11: dB-change in the first harmonic amplitude of the Hall conductivity per dB-change in HF power.

electron temperature and the Hall conductivity. For each case, we use the change in harmonic amplitude per change in HF power as an indicator for the physical process that is dominant at each HF power level.

Figure 3.11 shows the modeled change in first harmonic amplitude (in dB) divided by the change in HF power (in dB) at 72, 74, and 76 km altitude. This derivative essentially represents the localized (in HF power) value of the power-law parameter,  $n$ , as defined in Equation (3.1). The model results for linearized HF self-absorption and linearized electron energy loss rates are plotted together with the model output for both processes being linearized. These variations may be compared with the results of the full HF heating model to determine the dominant effect at each HF power level. We first evaluate the dependence of the full model output on the conductivity nonlinearity. When both self-absorption and the electron energy loss rates are linearized, the nonlinearities remaining can be attributed to the conductivity expression. When the resulting trace matches the full model run, the full model run is deemed to be dominated by the conductivity relationship with electron temperature. It is evident

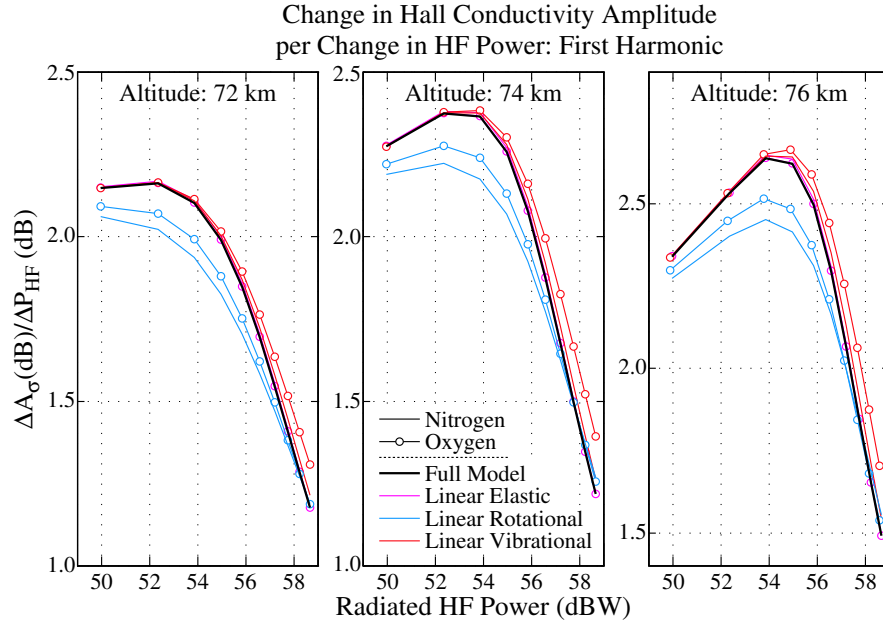


Figure 3.12: dB-change in the first harmonic amplitude of the Hall conductivity per dB-change in HF power. Each loss rate is linearized individually.

from Figure 3.11 that the conductivity dependence on temperature does not dominate the variation of the Hall conductivity first harmonic at any of the three altitudes.

The results shown in Figure 3.11 can also be used to evaluate the relative dominance of the self-absorption effect versus that of the electron energy loss rates. For instance, if the effect of self-absorption is linearized, and the output closely follows the full model result, then the nonlinearities associated with the self-absorption effect do not have a great impact on the overall output. Similarly, when model results for the case of linearized electron energy loss rates deviate from the full scale model the most, the nonlinear electron energy loss rates are the dominant nonlinear factor. In Figure 3.11, the dominant factor in the variation of the first harmonic amplitude as a function of HF power changes with altitude. We must, therefore, conclude that the effect of the saturation process on the first harmonic amplitude results from the combination of HF self-absorption and the electron energy loss rates.

Although we are unable to fully decouple the effects of self-absorption from those of the electron energy loss rates in this case, we can further examine the relative

importance of the different electron energy loss rates. Figure 3.12 is similar to Figure 3.11, except that each electron energy loss rate has been singularly linearized in turn. In this case, the linearized electron energy loss rate that results in the largest deviation from the full model result can be deduced to be the dominant factor at each power level. At each of the three altitudes shown in Figure 3.12, it is evident that at lower power levels (i.e.,  $<56$  dBW), the dominant electron energy loss rate is the rotational excitation of molecular nitrogen. It is also clear that the rotational excitation of molecular oxygen plays a secondary, but significant, role at these power levels. When it comes to higher HF power levels (i.e.,  $>56$  dBW), however, the dominant electron energy loss rate at all three altitudes is the vibrational excitation of molecular oxygen.

It thus appears that the slight deviation from power-law in the first harmonic amplitude at high HF power levels results from the growing importance of the vibrational excitation of molecular oxygen at relatively high electron temperatures. We cannot fully decouple the effect of the electron energy loss rates from that of the self-absorption mechanism, however, and it is likely that self-absorption also plays a role in the observed first harmonic deviation. At low HF power levels, it is clear from these modeling results that the power-law variation of the first harmonic amplitude results dominantly from the combined effects of the rotational excitation of molecular nitrogen and those of self-absorption.

We now perform a similar analysis on the second harmonic amplitude variation with HF power.

### 3.4.2 The Second Harmonic Amplitude

An analysis similar to that performed for the first harmonic amplitude may also be used to examine the variation of the second harmonic amplitude with HF power. Figure 3.13 shows the modeled change in second harmonic amplitude (in dB) divided by the change in HF power (in dB) at 72, 74, and 76 km altitude. As in the analysis of the first harmonic, HF self-absorption and electron energy loss rate effects are selectively and singularly linearized in order to bring out the dominant nonlinear physical

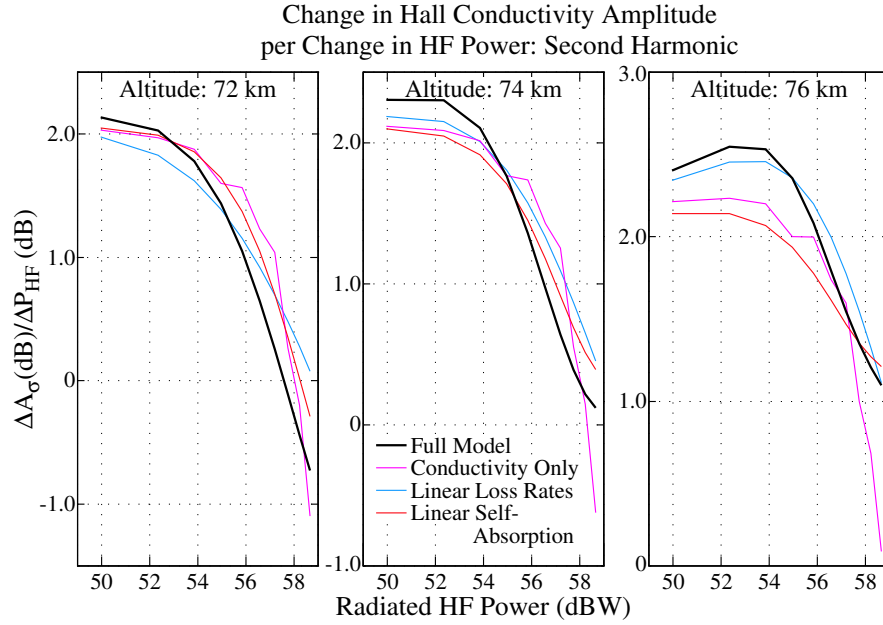


Figure 3.13: dB-change in the second harmonic amplitude of the Hall conductivity per dB-change in HF power.

mechanism. Inspecting the dependence of the full HF heating model output on the nonlinear nature of the Hall conductivity, it is evident from Figure 3.13 that the nonlinear dependence of the conductivity on electron temperature does not dominate at any of the three altitudes. In fact, at high HF power levels, the conductivity-only trace appears to significantly deviate from the full HF model output at all three altitudes. This lack of dominance by the Hall conductivity nonlinearity is similar to the model results for the first harmonic amplitude variation. The fact that neither the first nor the second harmonic amplitude variation matches the conductivity nonlinearity indicates that the observed saturation process does not result from the nonlinear relationship between conductivity and temperature.

Similar to the results of the first harmonic amplitude analysis, it is not clear from Figure 3.13 if any physical process consistently dominates the full scale model output at low HF power levels. For instance, HF self-absorption appears to dominate at low HF power levels at 74 and 76 km altitude, but not at 72 km altitude. At higher HF power levels, however, the results are different: the electron energy loss rates

consistently dominate the full model variation at high HF power levels at all three altitudes. At the same time, the nonlinear effects of HF self-absorption also have a significant impact on the full model output. Similar to the first harmonic analysis, we must conclude that the saturation of the second harmonic amplitude results from the combination of HF self-absorption effects and electron energy loss rate variations. It is not surprising that such is the case for the second harmonic amplitude variation, since a similar result was obtained in the analysis of the first harmonic amplitude. The fact that the variation of the second harmonic amplitude may be predicted from that of the first harmonic amplitude (as shown in Section 2.3 of this chapter), was an early indicator that the variation of the amplitude of the two harmonics may result from the same physical mechanism.

While decoupling the effects of self-absorption from the effects of the electron energy loss rates remains an elusive goal in the case of the second harmonic amplitude variation, as it was for the first harmonic amplitude variation, we may further examine the relative importance of the different electron energy loss rates. Figure 3.14 is similar to Figure 3.13, with the exception that each electron energy loss rate has been linearized in turn. At each altitude shown in Figure 3.14, the dominant electron energy loss rates at low power levels (i.e.,  $<56$  dBW) are the rotational excitation of molecular nitrogen and to a lesser extent the rotational excitation of molecular oxygen. In this case, the deviation from the full HF heating model curve is much smaller than in the case of the first harmonic, however, indicating that HF self-absorption plays a relatively larger role in the generation of the second harmonic at low power levels. At high HF power levels, the dominant electron energy loss rate switches to the vibrational excitation of molecular oxygen at 74 and 76 km altitude. This dependence on the vibrational excitation of molecular oxygen at high HF power levels is the same as observed in the case of the first harmonic.

The variation of the first and second harmonic amplitudes thus appear to result from the same physical process. Although we cannot decouple the effects of HF self-absorption from the effects resulting from the nonlinear electron energy loss rates, we are able to identify the dominant electron energy loss rates at both low and high power levels. For both the first and second harmonic amplitude, the dominant electron

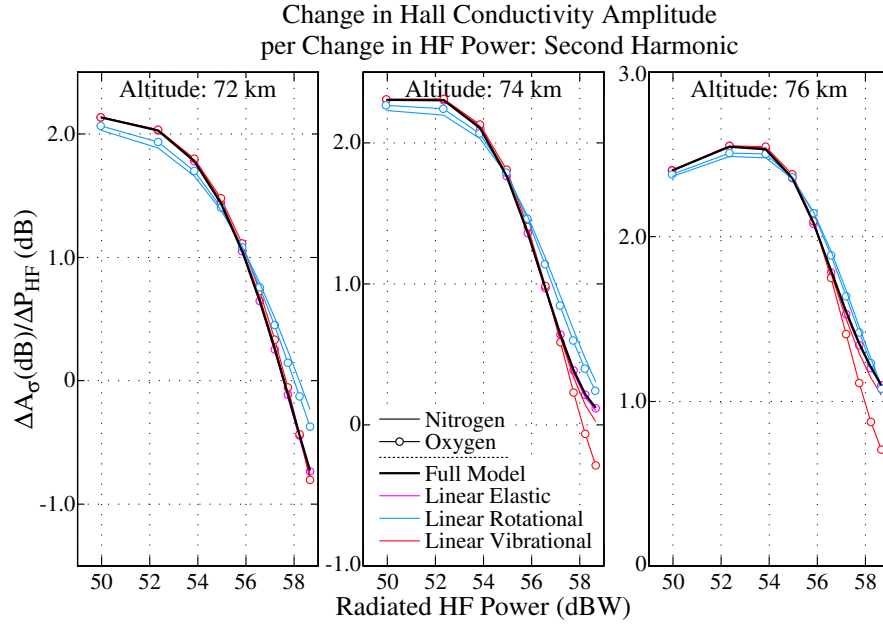


Figure 3.14: dB-change in the second harmonic amplitude of the Hall conductivity per dB-change in HF power. Each loss rate is linearized individually.

energy loss rate at high power levels is the vibrational excitation of molecular oxygen whereas the dominant electron energy loss rate at low power levels is the rotational excitation of molecular nitrogen.

In the following section, we inspect the variation of the third harmonic amplitude with HF power using the same techniques applied to the first two harmonics.

### 3.4.3 The Third Harmonic Amplitude

We now inspect the variation of the third harmonic amplitude by repeating the analysis performed for the first two harmonic amplitude variations. Figure 3.15 shows the modeled change in third harmonic amplitude (in dB) divided by the change in HF power (in dB) at 72, 74, and 76 km altitude. It is evident from Figure 3.15 that the Hall conductivity does not dominate the full model output at any of the three altitudes: the nonlinear dependence of the Hall conductivity on electron temperature does not match the variation of the full HF heating model. This result is consistent with the analyses of the first two harmonics and further indicates that the observed

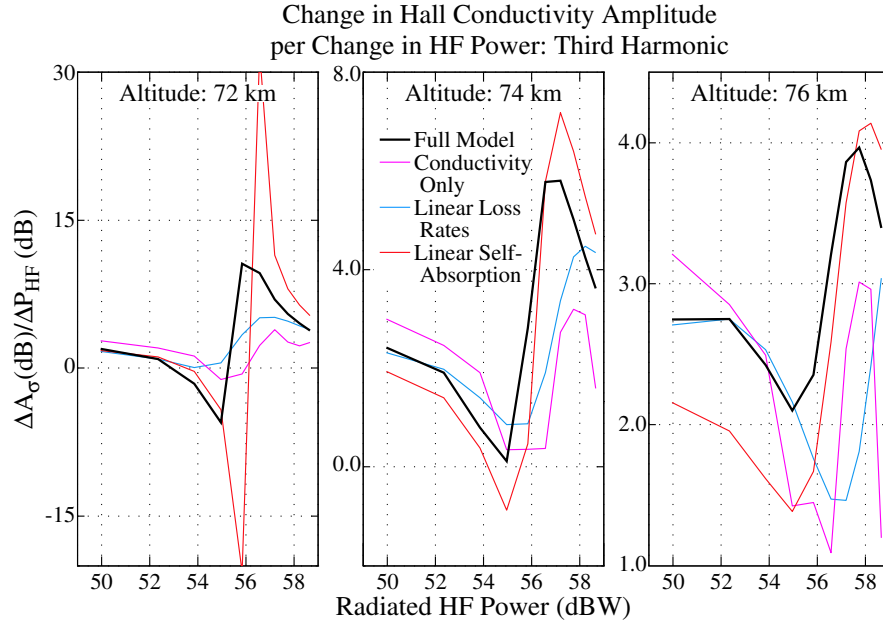


Figure 3.15: dB-change in the third harmonic amplitude of the Hall conductivity per dB-change in HF power.

saturation process does not result directly from the nonlinear dependence of the Hall conductivity on electron temperature.

Unlike the case of the first and second harmonic amplitude variations, however, it is clear from Figure 3.15 that self-absorption dominates the low-power amplitude of the third harmonic. At the same time, it should be noted that observations of the third harmonic amplitude are typically below the noise floor at low HF power levels. At high HF power levels, it becomes unclear which physical process dominates the variation of the third harmonic amplitude. On the one hand, the variations at 74 and 76 km indicate that the nonlinear electron energy loss rates dominate. On the other hand, the variation at 72 km indicates a much higher contribution of the HF self-absorption process at high HF power levels. Most importantly, the variation at 72 km, shown in Figure 3.9, most closely matches observations. We can thus conclude that at high power levels, the saturation process results from the combined effects of HF self-absorption and the electron energy loss rates.

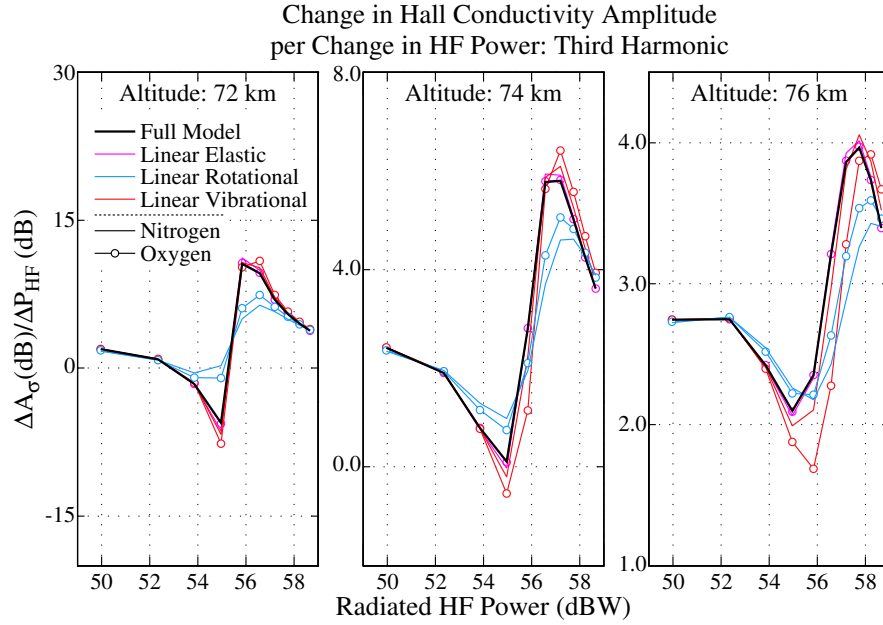


Figure 3.16: dB-change in the third harmonic amplitude of the Hall conductivity per dB-change in HF power. Each loss rate is linearized individually.

For the third harmonic, as for the first and second harmonics, we cannot fully decouple self-absorption from the electron energy loss rates at high power levels. Similar to the previous analyses, however, we may further examine the relative importance of the different electron energy loss rates in determining the variation of the third harmonic amplitude with HF power. Figure 3.16 shows a similar plot to Figure 3.15, except that each electron energy loss rate has been selectively and singularly linearized in turn. At all three altitudes shown in Figure 3.16, it is evident that at low power levels none of the electron energy loss rates dominate. This result is consistent with the conclusion that the dominant effect at low HF power levels is HF self-absorption. At high HF power levels (e.g.,  $>56$  dBW), however, the rotational excitation of molecular nitrogen clearly dominates the electron energy loss rates. The rotational excitation of molecular oxygen is also an important (although secondary) effect at high HF power levels.

Unlike the analyses of the first and second harmonics, the variation of the third harmonic amplitude does not appear to be dominated by the vibrational excitation

of molecular oxygen at high HF power levels. This result implies that the physical mechanism generating a third harmonic is different than that involved in the generation of the first and second harmonics. This conclusion is consistent with the analysis presented in Section 2.3 of this chapter. The variation in the third harmonic amplitude was not reproduced by incorporating the saturation function  $f_{\text{sat}}$  into the analysis, although the variation of the second harmonic was successfully predicted. Together, the full HF heating model results and the saturation function analysis of Section 2.3 indicate that, for sinusoidal amplitude modulation, the third harmonic is likely generated through a different physical process than the first and second harmonics.

It thus appears that the sharp jump from the noise floor in observations of the the third harmonic amplitude results from the combined effects of HF self-absorption and the rotational excitation of nitrogen and oxygen.

In this chapter, we have identified ELF/VLF amplitude saturation experimentally. Using an HF heating model, we have associated amplitude variations observed at low HF power levels with HF self-absorption and the electron energy loss rates due to the excitation of rotational states in molecular nitrogen. The identified saturation effect at high HF power levels is dominantly associated with the vibrational excitation of molecular oxygen through theoretical analysis of the first two harmonics. At the same time, the saturation effects on the third harmonic amplitude appear to be dominated by the rotational excitation of molecular nitrogen. It is possible that the variation of the first and second harmonic amplitudes results from a saturation process while the variation of the third harmonic amplitude results from an imbalance between the heating- and cooling-rates. Nonetheless, the variation of the third harmonic appears to be directly linked to the saturation process. The fact that the sharp rise from the noise of the third harmonic coincides with the onset of amplitude saturation in the first and second harmonics will be used in Chapter 5 of this dissertation to bound the occurrence rate of amplitude saturation using rather large data sets.

## Chapter 4

# An Optimal HF Power Level ( $<100\%$ Modulation Depth)

In this chapter, we explore another nonlinearity of the ELF/VLF wave generation process and identify an optimal average HF power level maximizing the observed ELF/VLF amplitude for modulation depths less than 100%. Within the context of the power-law system described by *Papadopoulos et al.* [1990] and *Barr and Stubbe* [1991a] [i.e., Equation (3.1)], the generated ELF/VLF amplitude would be purely monotonic with increasing average HF power. Instead, experimental results show a rising ELF/VLF amplitude at low average HF power levels and a falling ELF/VLF amplitude at high average HF power levels. The result is an optimal HF power level maximizing the amplitude of the generated ELF/VLF waves. Experimental evidence shows that the positive slope of the generated ELF/VLF amplitude versus HF power at low power levels and the negative slope at high power levels depend on the modulation depth, the modulation frequency, and the modulation waveform employed. Observations are compared against the predictions of the theoretical HF heating model described in Chapter 2 in order to attribute the observed behavior to physical processes.

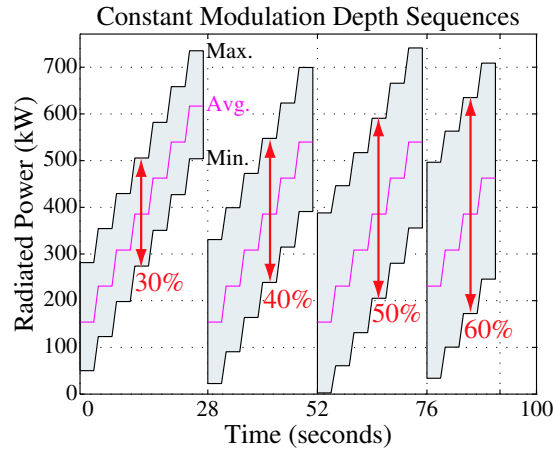


Figure 4.1: HAARP transmission schedule for the constant modulation depth experiment. During each 4-second-long power setting shown, the modulation frequency ramped linearly from 1 kHz to 4 kHz. The radiated power levels shown are for the 3.25 MHz carrier frequency employed during this experiment. The average levels shown here assume square wave amplitude modulation.

## 4.1 Description of the Experiment

The experiment reported herein was conducted during the course of one hour at the HAARP facility between 0700 and 0800 UT on August 8, 2006. Geomagnetic conditions were moderately disturbed during the transmission hour, with a  $K_p$  index of  $3^+$ . The absolute value of all magnetic field components measured by the fluxgate magnetometer located in Gakona, AK, remained below 60 nT during the transmission. The previous hour showed absolute magnetometer readings over 100 nT, while the subsequent hour reached a level greater than 200 nT. The HAARP HF transmitter broadcast at 3.25 MHz with X-mode polarization and with the power sequence shown in Figure 4.1. During each 4-second-long power setting, the modulation frequency was ramped linearly from 1 kHz to 4 kHz. The sequence was repeated seven times over the course of the hour using both sinusoidal amplitude modulation and square-wave amplitude modulation. The HF beam was directed vertically for all transmissions. The data presented in this Chapter were acquired using the Chistochina ELF/VLF receiver described in Chapter 3.

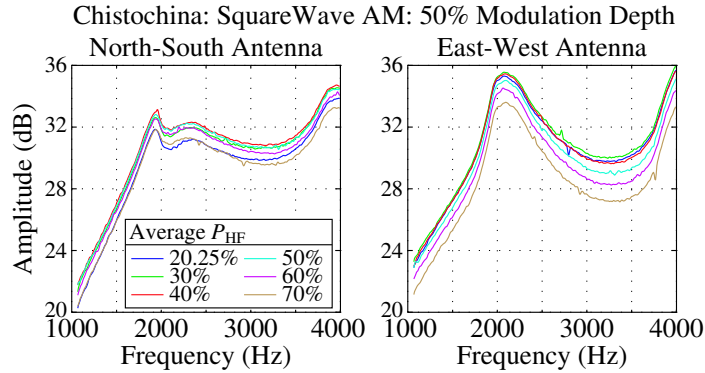


Figure 4.2: ELF/VLF amplitude variations observed on the North-South and East-West antennas at Chistochina during the 50% modulation depth, square-wave AM transmissions. The average HF power is expressed as a percentage of the maximum 771 kW radiated HF power.

## 4.2 Experimental Observations

Excellent ELF/VLF signal levels were observed over the course of the one-hour transmission sequence. In order to mitigate the effects of impulsive signals, such as the radio atmospherics emanating from lightning, the average amplitude over the course of the hour is used to investigate the properties of the ELF/VLF waves generated using each power setting and modulation format. Figure 4.2 shows the variation in ELF/VLF amplitude observed on the North-South and East-West antennas as a function of modulation frequency for the 50% modulation depth sequence performed using square-wave amplitude modulation. The observed variations in the amplitude of the received magnetic field as a function of modulation frequency are quite similar among the traces for each of the different HF power level settings. In fact, the variations in ELF/VLF amplitude as a function of modulation frequency are quite similar regardless of the power setting used and the modulation waveform employed, although we do not show all of the variations here. These variations are likely dominated by the effects of the Earth-ionosphere waveguide boundaries [Stubbe *et al.*, 1982]; in particular, they exhibit localized amplitude peaks at modulation frequencies similar to the well-known Earth-ionosphere waveguide resonances at multiples of  $\sim 2$  kHz [Porrat *et al.*, 2001]. The variation of the amplitude as a function of modulation

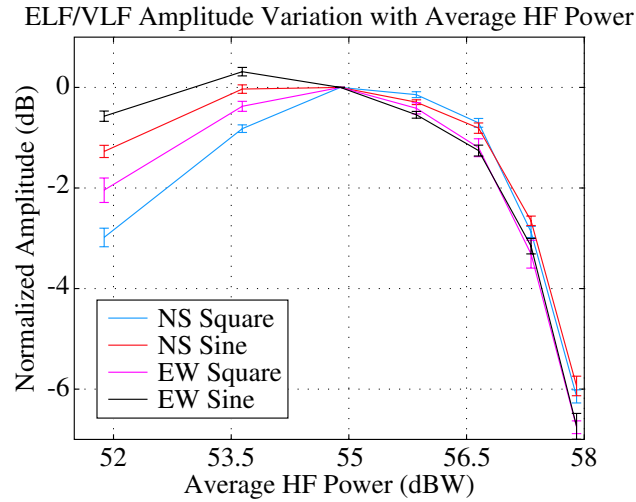


Figure 4.3: Average ELF/VLF amplitude, normalized by that of the 40% average HF power run, as a function of average HF power. In each case, the ELF/VLF amplitude is observed to rise at low power levels and fall at high power levels.

frequency is notably different on the North-South and East-West antennas, however. This difference is also likely dominated by the Earth-ionosphere waveguide boundary effects, which have been shown to be significantly different for the modulated Hall and Pedersen currents [Barr and Stubbe, 1984a], which would thus couple differently to the two orthogonal horizontal loop antennas. At the same time, the attenuation of the ELF/VLF wave generated in the lower ionosphere may experience different amounts of ionospheric attenuation, depending on the polarization of the wave, prior to coupling to the waveguide [Carroll, 1986], contributing to the difference between the North-South and East-West antenna measurements.

Regardless of the modulation frequency, however, the amplitude as a function of average HF power setting tends to increase at low power levels and decrease at high power levels, resulting in an optimal HF power level that maximizes the ELF/VLF amplitude. While this trend in ELF/VLF amplitude may be inferred from the various traces shown in Figure 4.2, this variation is clearly depicted in Figure 4.3, which shows the average ELF/VLF amplitude, normalized by that of the 40% average HF power run, as a function of average HF power. The variation is shown for each antenna (North-South and East-West) and for each modulation waveform (sinusoidal

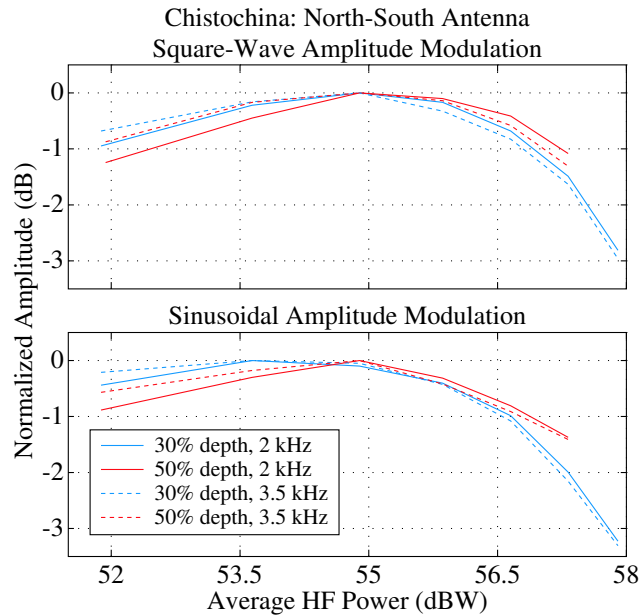


Figure 4.4: Observed amplitude variation on the North-South antenna as a function of average HF power for square-wave and sinusoidal amplitude modulation at 2.0 and 3.5 kHz.

AM and square-wave AM). The primary trend is the same for each trace: a rising ELF/VLF amplitude at low HF power and a falling ELF/VLF amplitude at high HF power. While the dominant trend for each of the traces is similar, there exist minor secondary differences among them. For instance, at high HF power levels, the ELF/VLF amplitude decreases faster as a function of average HF power on the East-West antenna than on the North-South antenna. In addition, at low HF power levels, the ELF/VLF amplitude generated by square-wave amplitude modulation increases faster with average HF power than does that produced by sinusoidal amplitude modulation. In addition to the small differences in the amplitude variation that depend on antenna orientation and modulation waveform, there are also small differences that depend on the modulation frequency and the modulation depth. We now examine the amplitude variations observed at individual frequencies and specific modulation depths.

Although the average ELF/VLF amplitude tends to rise with average HF power at low power levels and fall at high power levels, the dependencies of ELF/VLF

amplitude on average HF power for individual frequencies or for specific modulation depths may be different. In Figure 4.4, we compare the amplitudes observed at two modulation frequencies (2.0 and 3.5 kHz) generated using each of two modulation depths (30% and 50%) and observed on the North-South antenna. In the cases shown, the amplitude variations follow the average amplitude variations shown in Figure 4.3. However, the traces in Figure 4.4 indicate that, at low power levels, the ELF/VLF amplitude increases (with increasing HF power) at a slower rate for the higher modulation frequency. At high power levels, this slope is also lower for the higher modulation frequency. This behavior is apparent for both sinusoidal amplitude modulation and for square-wave amplitude modulation, as well as for both 30% and 50% modulation depths. From Figure 4.4, it is also apparent that the ELF/VLF amplitude exhibits the same behavior around the optimal HF power level as a function of modulation depth: the slope is lower for lower modulation depths, on both sides of the peak. In some cases, the optimal HF power level may, in fact, be lower for sinusoidal amplitude modulation than for square-wave amplitude modulation, as shown in the 30% modulation depth traces in Figure 4.4.

On the East-West channel, observations at the same modulation frequencies and the same modulation depths are somewhat different in character, as shown in Figure 4.5. The *average* ELF/VLF amplitude generated as a function of average HF power, shown in Figure 4.3, increases at low HF power levels and decreases at high HF power levels, and this amplitude variation with HF power may be taken to be typical for *each* antenna orientation and for *each* modulation waveform. The dependence of ELF/VLF amplitude on average HF power at the specific modulation frequencies chosen for Figure 4.5 are therefore atypical in that they do not show a significant rise in ELF/VLF amplitude at low HF power levels. Compared to the ELF/VLF amplitude observed on the North-South antenna as a function of average HF power, the ELF/VLF amplitude observed on the East-West antenna as a function of average HF power tends to reduce to a relatively lower (by  $\sim 1$  dB) amplitude than that observed on the North-South antenna at high average HF power levels. The modulation depth has a much more significant impact on the amplitude variation observed on the East-West antenna than on the North-South antenna. The relationship between 30% and

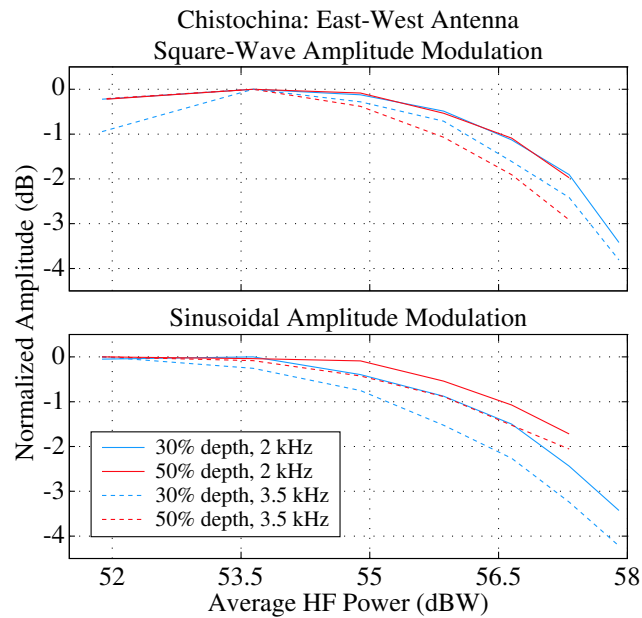


Figure 4.5: Observed amplitude variation on the East-West antenna as a function of average HF power for square-wave and sinusoidal amplitude modulation at 2.0 and 3.5 kHz.

50% modulation depths is also more complicated than observed on the North-South antenna. While the amplitude variation observed at 2 kHz using square-wave amplitude modulation does not appear to significantly depend on modulation depth, it is readily apparent from the other traces that the modulation depth is an important parameter. For instance, at 3.5 kHz, observations of ELF/VLF signals generated using square-wave modulation indicate that for a 50% modulation depth, the ELF/VLF amplitude decreases faster than that for a 30% modulation depth at high average HF power levels. For sinusoidal amplitude modulation, however, this relationship is exactly reversed, as can be seen from the lower panel of Figure 4.5.

While there exist differences between the amplitude variations observed on the North-South and East-West antennas, the overall dominant characteristic of the constant modulation depth transmission sequence is the increasing amplitude at low average HF power levels and the decreasing amplitude at high average HF power levels. This variation yields an optimal average HF power level that maximizes the ELF/VLF amplitude, as shown in Figure 4.3. The significant differences between the

amplitude variations observed on the North-South and East-West antennas, such as those shown in Figures 4.4 and 4.5, may be attributed to the selective sensitivity of each antenna to only one of either the modulated Hall or the modulated Pedersen currents. While this division may appear to be serendipitous, we point out that the significant differences only occur for certain modulation frequencies and that the average variation in amplitude on the East-West antenna is similar to that observed on the North-South antenna, as shown in Figure 4.3.

The observations presented herein as a function of HF power level are inconsistent with a power law dependence of ELF/VLF amplitude on HF power. In particular, the existence of an optimal average HF power level maximizing the ELF/VLF amplitude cannot be explained using the simple power-law relationship given by *Papadopoulos et al.* [1990] and *Barr and Stubbe* [1991a]. We now examine this variation in ELF/VLF amplitude in detail using the ionospheric HF heating model described in Chapter 2.

### 4.3 Comparison with Full HF Heating Model

The numerical analysis presented in this section follows a progression similar to that of the numerical analysis presented in Chapter 3. The primary purpose of this section is to reproduce the observed variation of ELF/VLF amplitude with average HF power and to examine the physical mechanisms responsible for the behavior. We accomplish this task by linearizing, selectively and in turn, each of the physical processes accounted for by the HF heating model and comparing the results with observations.

Figure 4.6 shows the amplitude of the Hall and Pedersen conductivity modulation as a function of altitude resulting from model calculations using a 3.25 MHz, X-mode carrier signal, square-wave amplitude modulated at 2 kHz. Electron density Profile III was used. Similar to the ELF/VLF amplitude saturation runs presented in Chapter 3, the altitude of the maximum Hall conductivity modulation is  $\sim 78$  km, whereas the altitude of the maximum Pedersen modulation is  $\sim 80$  km. As can be seen from Figure 4.6, these altitudes do not change as a function of the HF power setting. We now investigate the dependence of the amplitude of the conductivity modulation on HF power within  $\sim 5$  km of these maximum conductivity modulation

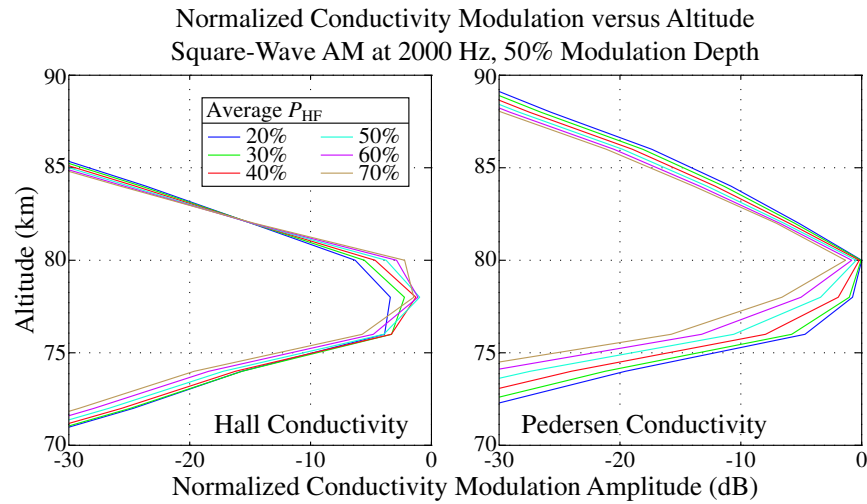


Figure 4.6: Amplitude of the Hall and Pedersen conductivity modulation as a function of altitude. The model results were calculated using a 3.25 MHz, X-mode carrier signal, square-wave amplitude modulated at 2 kHz. Electron density Profile III was used.

altitudes.

The variation in amplitude of the modulated ionospheric conductivity as a function of average HF power is shown in Figure 4.7. The variations shown were selected because they approximately match observations and because they are at altitudes within  $\sim 5$  km of the altitude of maximum conductivity modulation. In fact, in this case, each of the traces is within 2 km of the altitude of the maximum conductivity modulation. The left-hand panel of Figure 4.7 shows the matching Hall conductivity variations at 76 and 78 km altitude. It is evident that the variation of the Hall conductivity, which may rise and fall by as much as 2 dB, matches the rising as well as the falling nature of the majority of our ground-based ELF/VLF observations.

The right-hand panel of Figure 4.7 shows the Pedersen conductivity variation at three altitudes surrounding the altitude of maximum conductivity modulation. None of these variations increase with average HF power at low power levels. As a result, it does not appear as though the Pedersen variation matches the majority of our ground-based observations. The fact that the Hall conductivity modulation provides the best match for the ground-based observations is consistent with the results

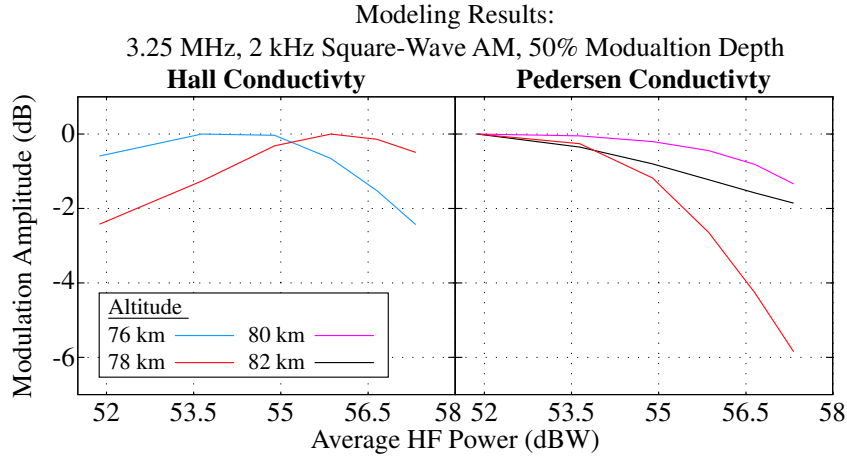


Figure 4.7: The Hall and Pedersen amplitude variations with average HF power that best match observations. The Hall conductivity modulation maximum is at 78 km, whereas the Pedersen conductivity modulation maximum is at 80 km.

of Chapter 3, in which we determined that the Hall conductivity best matched our observations of ELF/VLF amplitude saturation on the ground. At the same time, however, the amplitude of the Pedersen conductivity modulation, which drops by as much as 6 dB at high average HF power levels, matches the few cases in which the variation on the East-West antenna is completely different from that observed on the North-South antenna. It thus appears that the Hall conductivity variation may dominate the received signal amplitude on one antenna while the Pedersen conductivity modulation dominates the received signal in the other. Although observations on the ground sometimes match the variation in the amplitude of the Pedersen conductivity modulation, we analyze only the Hall conductivity modulation as a function of average HF power because we are primarily interested in the physical mechanisms which together result in an optimal average HF power level.

We inspect the Hall-like variation of the first harmonic amplitude using the same method as Chapter 3: by linearizing, in turn, the effects of self-absorption and the effects of the electron energy loss rates. By linearizing both effects at the same time, we are able to evaluate the ELF/VLF amplitude dependence on the nonlinear relationship between electron temperature and the Hall conductivity. For each case, we use the change in ELF/VLF amplitude per change in HF power as an indicator for

the physical process that is dominant at each HF power level. In order to investigate the relative importance of the physical mechanisms responsible for the observed variation of ELF/VLF amplitude with average HF power, we concentrate on the Hall conductivity variation at 76-78 km altitude, which is the altitude range of maximum Hall conductivity modulation.

Figure 4.8 shows the modeled change in first harmonic amplitude (in dB) divided by the change in HF power (in dB) at 76 and 78 km altitude. The model output for linearized HF self-absorption and linearized electron energy loss rates are plotted together with the model output for both processes being linearized. We compare these variations with the results of the full HF heating model to determine the dominant effect at each HF power level. We first evaluate the dependence of the full model output on the conductivity nonlinearity. When both self-absorption and the electron energy loss rates are linearized, the nonlinearities remaining are attributed to the conductivity expression. If the resulting trace matches the full model run, the full model run is deemed to be dominated by the conductivity relationship with electron temperature. It is evident from Figure 4.8 that, for the first harmonic, the conductivity dependence on temperature does not dominate the variation of the Hall conductivity for any HF power setting. Furthermore, as explained in Chapter 3, the linearized physical process that results in the amplitude trace which is farthest from the full model trace is likely the one which dominates the nonlinearities at that average HF power level. In Figure 4.8, it is evident that at both 76 and 78 km altitude, the self-absorption process dominates at low average HF power levels, whereas the electron energy loss rates dominate the amplitude variation above  $\sim 55$ -56 dBW.

We can further examine the relative importance of the different electron energy loss rates at both low and high average HF power levels. As seen from Figure 4.8, at low power levels, the loss rates are dominated by the HF self-absorption process. Figure 4.9 is similar to Figure 4.8, except that each electron energy loss rate has been selectively linearized in turn. In this case, the linearized electron energy loss rate that results in the largest deviation from the full model output is likely the dominant factor at each power level. At both altitudes shown in Figure 4.9, it is evident that at lower power levels (i.e.,  $< 54.5$  dBW), the dominant electron energy loss rate is

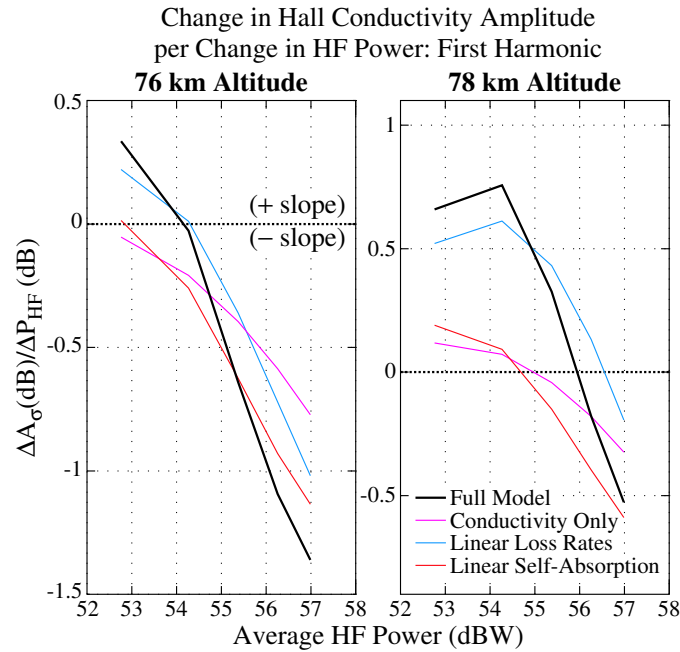


Figure 4.8: dB-change in the first harmonic amplitude of the Hall conductivity per dB-change in HF power.

the rotational excitation of molecular nitrogen (although at these power levels, HF self-absorption dominates electron energy loss). It is also clear that the rotational excitation of molecular oxygen plays a secondary but significant role at these power levels. At mid-range average HF power levels (54.5-56 dBW), the vibrational excitation of molecular oxygen has the dominant effect. This power range is the one in which the full model output is maximized (with approximately zero slope). At the highest HF power levels (i.e., >56 dBW), however, the rotational excitation of molecular nitrogen dominates the amplitude variation. The rotational excitation of molecular oxygen plays a secondary role at these HF power levels, as well.

It thus appears that the optimal HF power level results from the competing effects of self-absorption at low average HF power levels and the electron energy loss rates at high average HF power levels. At low average HF power levels, the margin between the maximum and minimum temperature attained over the course of a heating cycle increases with increasing average HF power, due to the more effective absorption of HF energy with increasing electron temperature. At middle-range average HF power

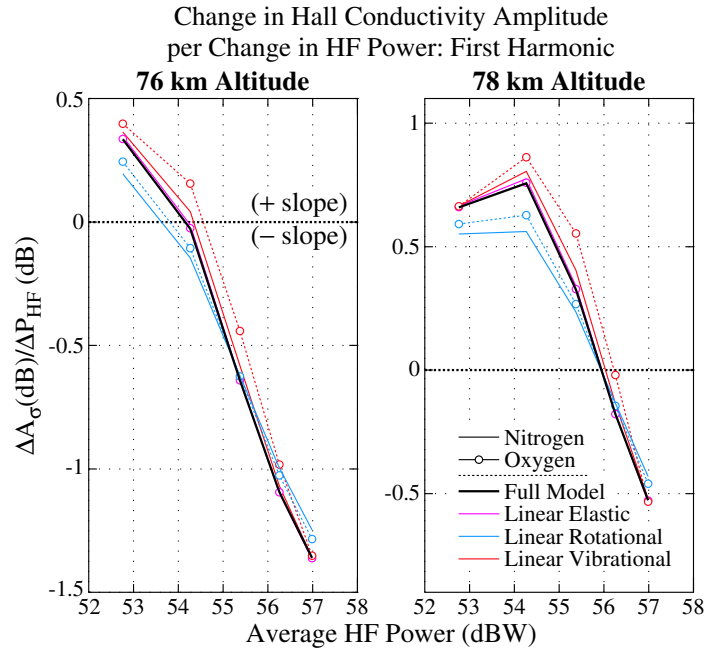


Figure 4.9: dB-change in the first harmonic amplitude of the Hall conductivity per dB-change in HF power. Each loss rate is linearized individually.

levels, the maximum temperature attained is such that the vibrational excitation of molecular oxygen becomes important. As shown in Chapter 3 of this dissertation, the vibrational excitation of molecular oxygen is dominantly responsible for the onset of ELF/VLF amplitude saturation. Thus, as the average HF power is increased within the middle power range, the maximum temperature attained begins to increase at a slower rate due to the higher electron energy losses associated with the vibrational excitation of molecular oxygen. As a result, the observed variation in ELF/VLF amplitude is strongly associated with the vibrational excitation of molecular oxygen at these middle HF power levels. At high average HF power levels, the ELF/VLF amplitude decreases significantly due to the increase of the minimum electron temperature attained while the maximum electron temperature remains in a saturated regime. For this reason, the loss rate that dominates the variation of the minimum electron temperature dominates the variation of the received ELF/VLF amplitude. In this case, the rotational excitation of molecular nitrogen emerges as the dominant factor.

In this chapter, we have identified an optimal average HF power level maximizing the ELF/VLF amplitude observed at ground-based receivers for modulation depths less than 100%. We have associated the observed amplitude variation with the variation of the Hall conductivity modulation with average HF power. Using an HF heating model, the Hall conductivity modulation at low average HF power levels was shown to be dominated by the HF self-absorption process. The ELF/VLF amplitude thus increases as a result of the increasing rate of absorption at higher electron temperatures. At mid-power ranges, the vibrational excitation of molecular oxygen was shown to become an important factor working against the effectiveness of the Hall conductivity modulation. At high average HF power levels, the rotational excitation of molecular nitrogen and oxygen were shown to become the dominant effects. It is not intuitive that the amplitude variation at high average HF power levels should be dominated by the electron energy loss rate which is dominant primarily at lower HF power levels. At the same time, this electron energy loss rate is the dominant factor determining the minimum electron temperature attained during the heating process.

# Chapter 5

## Statistical Analysis of ELF/VLF Amplitude Saturation

In this chapter, we use long-term experimental data sets to establish the fact that the nonlinearity associated with ELF/VLF amplitude saturation, as defined in Chapter 3, occurs on a regular basis and under varying geomagnetic conditions. Long-term observations of amplitude saturation for ELF/VLF waves generated using two different HF frequencies imply that saturation effects are observed more often at lower HF frequencies. Furthermore, the ability to detect the nonlinearities associated with ELF/VLF amplitude saturation at ground-based receivers is shown to depend on the location of the HF-heated region (or equivalently, the direction of the HF beam) relative to the location of the ELF/VLF receiver. This detectable spatial effect is interpreted herein as another manifestation of the described ELF/VLF amplitude saturation.

### 5.1 Description of the Long-Term Experiments

The long-term data sets shown in this chapter were acquired in two different experimental ELF/VLF wave-generation campaigns conducted with the HAARP facility described earlier in this dissertation. The first campaign lasted for fourteen days from March 16 to March 29, 2002. ELF/VLF receivers were situated at 36 and

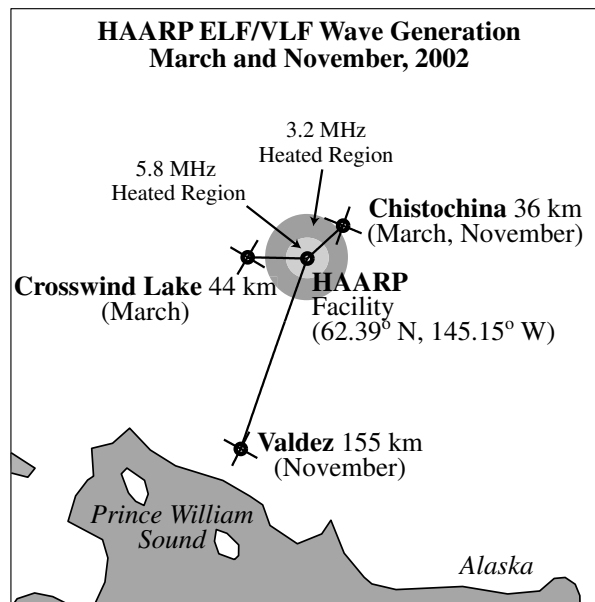


Figure 5.1: Map of ELF/VLF receivers in relation to the HAARP facility. The half-power heated regions expected for 3.2 MHz and 5.8 MHz transmissions at 75 km altitude are superimposed on the map.

45 km ground distance from the HAARP facility at Chistochina and Crosswind Lake, Alaska, respectively, as depicted in Figure 5.1. The HAARP HF transmitter operated continuously for ten hours each day of the campaign, between 0400 and 1400 UT, alternating between a vertical-beam transmission hour and a swept-beam transmission hour. During each day, the time periods 0530-0600, 0800-0830, and 1130-1200 UT were reserved for other experiments. For the first half-hour of each transmission hour an HF frequency of 3.2 MHz with X-mode polarization (Radiated Power: 771 kW; ERP: 18 MW; Main Lobe 3 dB width:  $37 \times 53 \text{ km}^2$  at 75 km altitude) was used, while for the second half hour the HF frequency was 5.8 MHz with X-mode polarization (Radiated Power: 936 kW; ERP: 91 MW; Main Lobe 3 dB width:  $20 \times 29 \text{ km}^2$  at 75 km altitude). During the vertical beam transmission hour, the central heating lobe of the HF beam was pointed directly toward the zenith over the HAARP facility. During the swept-beam transmission hour, the main lobe was directed  $30^\circ$  from the vertical in each of the cardinal and ordinal directions, rotating clockwise from North and spending ninety seconds in each of the eight positions before returning

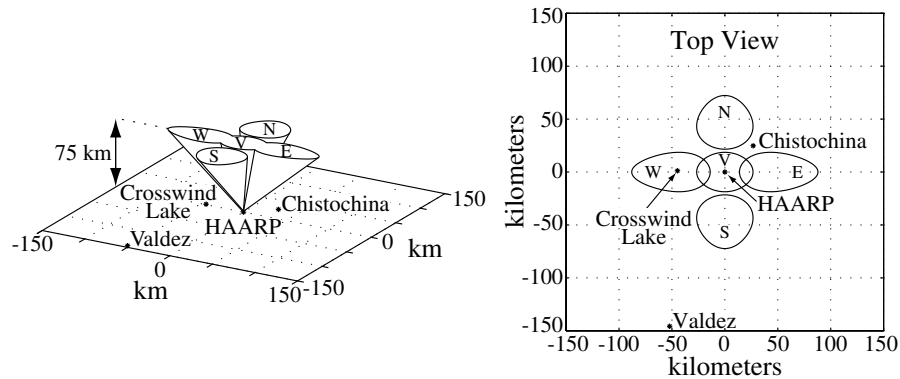


Figure 5.2: The approximate lateral area (at 75 km altitude) heated by the 3.2 MHz beam aimed vertically and  $30^\circ$  from the vertical in each of the four cardinal directions is shown in relation to the ground-based ELF/VLF receivers.

to the vertical. The lateral area (at 75 km altitude) heated by the 3.2 MHz beam aimed vertically and  $30^\circ$  from the vertical in each of the four cardinal directions is approximated in Figure 5.2 and shown in relation to the ground-based receivers. The sweeping pattern was implemented for each HF frequency during the corresponding half-hour periods. For all transmission hours, the amplitude of each carrier frequency was sinusoidally modulated at ELF/VLF frequencies varying between  $\sim 1$  and 4 kHz. The sixty-second long modulation pattern, shown in Figure 5.3, was repeated throughout the campaign. The statistics presented herein are based on the signal properties extracted from each of the single frequency tones shown in Figure 5.3.

For the second campaign, lasting 24 days from November 2 to November 25, 2002, HAARP transmitted with the same transmission scheme, replacing the 3.2 MHz carrier frequency with 3.25 MHz. In the analyses presented here, we consider the two frequencies to be essentially equivalent. No time blocks were reserved for other experiments on a daily basis during this November 2002 campaign, during which the ELF/VLF receivers were located at ground distances of 36 and 155 km from the HAARP facility at Chistochina and Valdez, Alaska, respectively, as shown in Figure 5.1.

Each of the three ELF/VLF receivers used to acquire the data reported herein

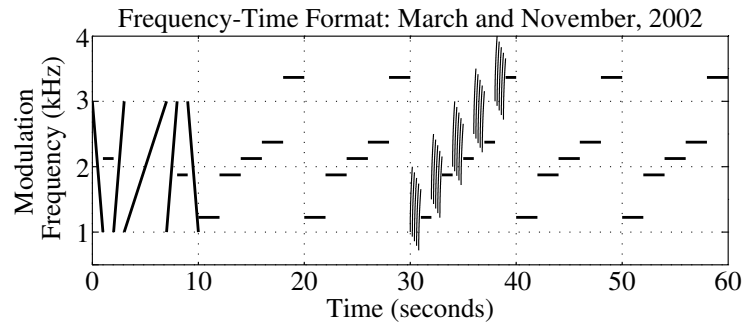


Figure 5.3: The 60-second duration modulation frequency-time transmission format, including ramps (0-10 sec), tones (10-30 and 40-60 sec), and chirps (30-40 sec).

utilizes  $4.8 \times 4.8 \text{ m}^2$ , air-core loop antennas oriented to detect the horizontal components of the wave magnetic field on the ground. The analog electronics used in the receivers at Crosswind Lake and Valdez are similar to that described in Chapter 3 for the Chistochina receiver. At each receiver, the 100 kHz digital data stream was digitally filtered to a 5625 Hz bandwidth, decimated to a sampling rate of 12.5 kHz, and saved to disk in real-time. Hardware upgrades to the ELF/VLF receiver at Chistochina in 2003 allowed for continuous archiving of the 100 kHz data without digital filtering and decimation during the subsequent experimental campaigns, some of which are reported in the earlier chapters of this dissertation.

The two long-term ELF/VLF wave-generation campaigns discussed herein cover over 350 hours of transmission time and over 350,000 individual transmissions (in the form of 2-second long pulses) at five individual ELF/VLF frequencies (ranging from 1225 to 3365 Hz). Artificially generated ELF/VLF signals at all modulation frequencies were observed at detectable levels ( $>10 \text{ dB SNR}$ ) every night of operation at receivers within 50 km of the HAARP facility, while the ELF/VLF receiver at Valdez observed discernible signals on only 80% of the nights. ELF/VLF signal generation was observed under varying geomagnetic conditions, although the strongest signal levels were observed during geomagnetically active periods. Geomagnetic conditions are assessed using the  $K_p$  index, which reached values as high as 6 on several occasions during each campaign. While strong natural ELF/VLF signals, such as hiss, chorus, and lightning-generated whistlers, were observed at times during the March

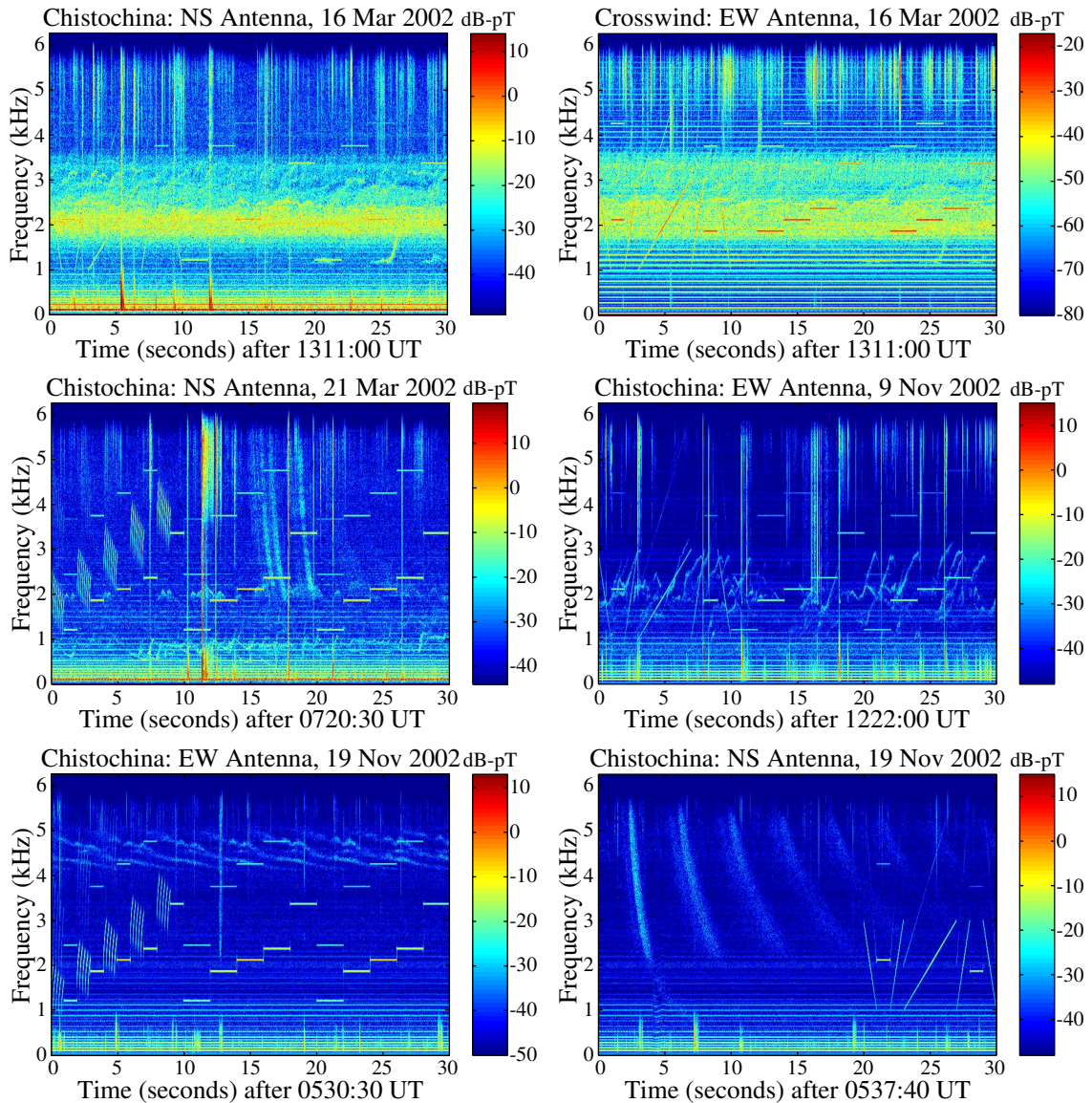


Figure 5.4: Various examples of natural activity observed in the ELF and VLF bands during March and November 2002, at Chistochina and Crosswind Lake. Chistochina and Crosswind Lake observe a  $\sim 2$  kHz bandwidth ELF/VLF hiss structure at the same time on March 16. Chorus emissions and whistler activity are observed at Chistochina on March 21 and November 9. Quasi-periodic emissions in the 4-5 kHz band were recorded at Chistochina on November 19. Lastly, a 30-second duration whistler echo train was observed at Chistochina on November 19.

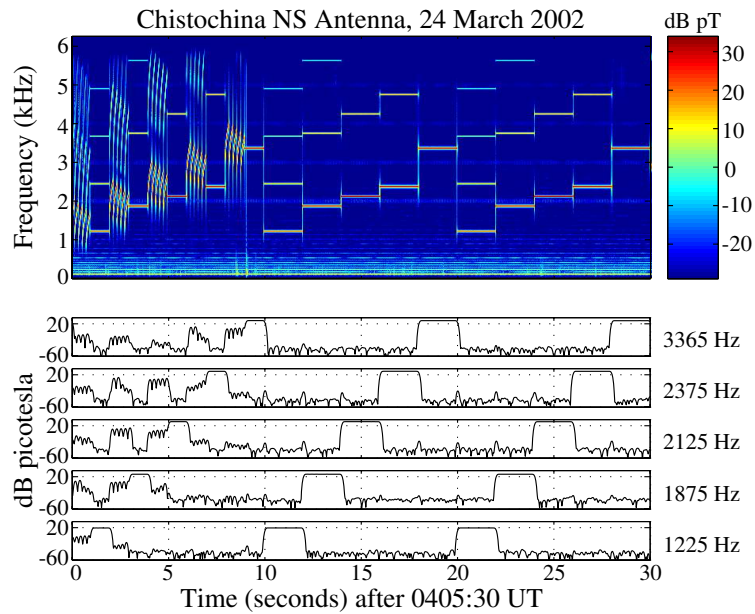


Figure 5.5: Large-amplitude ELF/VLF signal generation observed for all modulation frequencies at Chistochina on March 24, 2002. The bottom panels show the 15-Hz bandwidth narrowband amplitude for each modulation frequency extracted via digital filtering.

and November 2002 transmissions (e.g., see Figure 5.4), strong ELF/VLF signal generation by HAARP was also observed at times during periods without any natural ELF/VLF wave activity (e.g., see Figure 5.5). In general, the observations seem to indicate that modulated HF heating with the HAARP HF transmitter leads to robust generation of detectable ELF/VLF signals under virtually all geomagnetic conditions.

We now use the data sets collected during these two long-duration ELF/VLF wave-generation campaigns to assess the occurrence rate of ELF/VLF amplitude saturation, given the observations presented in Chapter 3.

## 5.2 Occurrence of ELF/VLF Amplitude Saturation

The experimental campaigns performed in March and November 2002 were conducted using only the maximum HF power level, complicating the positive identification of ELF/VLF amplitude saturation during these transmissions. We therefore rely on the observations presented in Chapter 3 to identify occurrences of the identified ELF/VLF amplitude saturation. In particular, Figure 3.2 presents observations of the third harmonic amplitude as a function of radiated HF power. The sharp increase in the third harmonic amplitude at high HF power levels coincides with the deviation of the second harmonic amplitude from a power-law variation, i.e. the ELF/VLF amplitude saturation effect described in Chapter 3. We therefore define a positive occurrence of ELF/VLF amplitude saturation at maximum HF power as an event in which the third harmonic amplitude is observed with an SNR greater than or equal to a threshold value, which we arbitrarily set to be 10 dB. We further limit our observations to transmissions during which the first harmonic amplitude is also generated with an SNR  $\geq 10$  dB. This condition excludes the cases when ELF/VLF wave generation is generally poor. Altogether, the occurrence rate of ELF/VLF amplitude saturation at maximum HF power is defined herein as the conditional probability that the third harmonic SNR is greater than or equal to 10 dB, given that the first harmonic SNR is greater than or equal to 10 dB.

In Chapters 3 and 4 of this dissertation, we presented observations of ELF/VLF waves generated using a 3.25 MHz carrier frequency and detected on the ground at Chistochina, Alaska. In this section, we inspect the occurrence rate of ELF/VLF amplitude saturation at two receivers (Chistochina and Crosswind Lake, see Figure 5.1) within 50 km of the HAARP transmitter and for ELF/VLF waves generated using two different HF carrier frequencies (3.2 and 5.8 MHz). Tables 5.1 and 5.2 show the statistical occurrence rates observed during the March 2002 HAARP campaign for the 1225 Hz modulation frequency. The relatively lower noise floor observed at the third harmonic of the 1225 Hz signal makes it ideal for the detection of ELF/VLF

Table 5.1: March 2002: 1225 Hz amplitude statistics at Chistochina

$f_{\text{HF}}$ (MHz)	Total Count	1 <sup>st</sup> harm. > 10 dB SNR	3 <sup>rd</sup> harm. > 10 dB SNR	3 <sup>rd</sup> , given 1 <sup>st</sup> > 10 dB SNR
3.2	3528	2985 (85%)	1945 (55%)	1893 (63%)
5.8	4410	3603 (82%)	1645 (37%)	1612 (45%)

Table 5.2: March 2002: 1225 Hz amplitude statistics at Crosswind Lake

$f_{\text{HF}}$ (MHz)	Total Count	1 <sup>st</sup> harm. > 10 dB SNR	3 <sup>rd</sup> harm. > 10 dB SNR	3 <sup>rd</sup> , given 1 <sup>st</sup> > 10 dB SNR
3.2	5390	4465 (83%)	2389 (44%)	2308 (52%)
5.8	6860	4477 (65%)	1287 (19%)	1175 (26%)

amplitude saturation onset. Because the observations presented in Chapter 3 indicate that the ELF/VLF amplitude saturation effect occurs approximately equally at each of the modulation frequencies inspected in the  $\sim 1\text{-}4$  kHz range, we take the third harmonic of the 1225 Hz signal as generally representative of the third harmonic production for signals with modulation frequencies in the  $\sim 1\text{-}4$  kHz range. We first note that the total number of detected 2-second-long 1225 Hz transmissions at 3.2 and 5.8 MHz (designated at ‘Total Count’ in Tables 5.1-5.4) are different due to the different number of half-hour periods reserved for other experiments during this campaign. In addition, a different total number of received transmissions are shown for the two receivers due to the different lengths of receiver down-time. For instance, the Chistochina receiver was down for several days at the end of the campaign while Stanford personnel ensured the proper operation of the Crosswind Lake receiver, some 75 km away.

It is evident from Table 5.1 that at Chistochina, ELF/VLF amplitude saturation is detected often: 63% of the time at 3.2 MHz and 45% of the time at 5.8 MHz. While the lower saturation rate at 5.8 MHz may be due to the lower rate of absorption at higher HF frequencies, it may also result from the generally lower ELF/VLF signal strengths observed for waves generated using the higher HF frequency, essentially

indicating a lower *detection* rate rather than a lower *occurrence* rate. As is shown later in this chapter, the lower rate of observation may also result from the reduced horizontal extent of the HF beam at higher frequencies.

At Crosswind Lake, the saturation rate observed using 3.2 MHz is lower by  $\sim 10\%$  compared to that measured at Chistochina, whereas the saturation rate observed using 5.8 MHz is lower by  $\sim 20\%$ . The fact that the saturation rates observed at the two receiver sites decrease by significantly different amounts at the two HF frequencies cannot be explained using a simple HF absorption argument. However, the difference may be explained if the higher HF frequency results in an effective ELF/VLF dipole at a higher altitude. In this case, the difference in propagation distance to Chistochina and to Crosswind Lake is larger for the ELF/VLF signals generated using the higher HF frequency. The relatively larger propagation distance may thereby result in a relatively lower SNR for signals generated using the higher HF frequency, creating relatively fewer saturation ‘events’ at the higher HF frequency at Crosswind Lake. At the same time, however, Crosswind Lake, being about 10 km farther from HAARP than Chistochina, may be simply more sensitive to portions of the heated region farther from the center of the HF beam (and therefore not saturated to the same extent as the portions dominating the received field at Chistochina). In this case, the portion of the ELF/VLF source region that dominates ground-based observations may experience less saturation for 5.8 MHz heating than the portion that dominates signal reception for 3.2 MHz heating, due to the smaller lateral dimension of the 5.8 MHz beam.

Regardless of the physical explanation, ELF/VLF amplitude saturation is detected often at Chistochina,  $\sim 36$  km from HAARP, and less often at Crosswind Lake,  $\sim 45$  km from HAARP. At both receivers, ELF/VLF amplitude saturation occurs more than 50% of the time for signals generated using a carrier frequency of 3.2 MHz. Considering the range of geomagnetic conditions encountered over the course of the experiments ( $K_p$  varying from 0 to 6), it is fair to say that ELF/VLF saturation occurs under all geomagnetic conditions for transmissions using a 3.2 MHz carrier. The saturation occurrence rate using 5.8 MHz, however, tends to be significantly (18-26%) lower than that observed using 3.2 MHz.

We now turn our attention to the occurrence of saturation observed during the November 2002 campaign as shown in Tables 5.3 and 5.4. Firstly, Table 5.3 indicates that observations of ELF/VLF amplitude saturation at Chistochina occur more often (79%) for 3.25 MHz transmissions during this campaign than for 3.2 MHz transmissions during the March 2002 campaign. At the same time, saturation onset is observed significantly less often (18% versus 45%) for 5.8 MHz transmissions during this campaign. The differences in occurrence rates between the March and November campaigns may result from different geomagnetic and/or ambient ionospheric conditions during the two campaigns. More important, however, is the difference between observations at Chistochina, 36 km northeast of HAARP, and those at Valdez, 155 km south-southwest of HAARP. At Valdez, observations of ELF/VLF amplitude saturation are almost nonexistent (3% and 2% at 3.2 and 5.8 MHz, respectively; see Table 5.4). On the one hand, the attenuation of the third harmonic within the Earth-ionosphere waveguide may be higher than that of the first harmonic [e.g., see *Wait*, 1957], leading to a lower detection rate of the third harmonic via a lower SNR. On the other hand, significant Earth-ionosphere waveguide effects have been shown to become dominant at distances of  $\sim 500$  km [*Barr et al.*, 1986], indicating that Earth-ionosphere waveguide effects are likely not responsible for such a significant lack of saturation observations at Valdez, which is only  $\sim 155$  km from the HAARP facility. The significant lack of observations of ELF/VLF amplitude saturation onset at Valdez may instead result from the distributed nature of the ELF/VLF source region. The receiver at Valdez, located more than 100 km farther from the HAARP transmitter than Chistochina, may simply be dominated by the ELF/VLF waves generated near the outer edge of the HF-heated region, where the effects of saturation may be less significant.

In the end, Tables 5.1-5.4 indicate that the onset of ELF/VLF amplitude saturation occurs at least  $\sim 20\%$  of the time and that this effect is detectable at ground-based ELF/VLF receivers located within  $\sim 50$  km of the HAARP facility. At 3.2/3.25 MHz, saturation onset occurs most of the time, regardless of the geomagnetic conditions. The observations listed in Tables 5.1-5.4 imply that the rate of occurrence of ELF/VLF amplitude saturation onset decreases with distance from the center of the HF

Table 5.3: November 2002: 1225 Hz amplitude statistics at Chistochina

$f_{\text{HF}}$ (MHz)	Total Count	1 <sup>st</sup> harm. > 10 dB SNR	3 <sup>rd</sup> harm. > 10 dB SNR	3 <sup>rd</sup> , given 1 <sup>st</sup> > 10 dB SNR
3.25	11760	10345 (88%)	8232 (70%)	8201 (79%)
5.8	11760	9402 (80%)	1756 (15%)	1700 (18%)

Table 5.4: November 2002: 1225 Hz amplitude statistics at Valdez

$f_{\text{HF}}$ (MHz)	Total Count	1 <sup>st</sup> harm. > 10 dB SNR	3 <sup>rd</sup> harm. > 10 dB SNR	3 <sup>rd</sup> , given 1 <sup>st</sup> > 10 dB SNR
3.2	12740	4376 (34%)	172 (1%)	128 (3%)
5.8	12740	1585 (12%)	73 (1%)	25 (2%)

beam and decreases with increasing HF frequency. However, it is possible that small changes in the noise levels at the third harmonic could change these relationships. For instance, with a decrease in the third harmonic noise level, there would likely be an increase in the detection of the third harmonic generated using 5.8 MHz, and this increase may be more than the increase observed for signals generated using 3.2 MHz. At the same time, it should be noted that the listed occurrence rates are minimal occurrence rates, i.e., the number of positive third harmonic detections can only increase.

Throughout this section, we have suggested that the spatial distribution of the ELF/VLF source region affects our observations, while allowing for other physical explanations of the observations. In the following section, we more directly address this issue using the results of an HF heating experiment during which the size and location of the HF-heated region were varied.

### 5.3 Spatial Distribution of the Source Region

In the previous section, observations of the first and third harmonic amplitudes were used to imply that the observed occurrence rate of ELF/VLF amplitude saturation

onset decreases with receiver distance from the center of the HF beam and, in addition, decreases with increasing HF frequency. In this section, we use observations at the same three ground-based ELF/VLF receivers during the swept-beam transmission hours of the March and November 2002 campaigns to demonstrate the dependence of saturation observations on the location of the HF-heated region in relation to that of the receiver. The results of this analysis indicate that the variations observed at each of the three receivers result from the dependence of the observed ELF/VLF amplitude on the spatial distribution of the conductivity modulation within HF-heated region.

During the swept-beam transmission hours of the March and November 2002 campaigns, the location of the ELF/VLF source region was varied using eight different HF beam headings. In this section, we compare the saturation levels observed at each of these eight headings in order to evaluate whether the observed ELF/VLF amplitude saturation onset depends on the ELF/VLF source region location in relation to that of the receiver. The comparison of ELF/VLF signals at different frequencies and with different source locations is further complicated by the effects of the Earth-ionosphere waveguide, which not only depend on the frequency of the signal, but also depend on the propagation characteristics of the signal path. Due to this complication, the statistical analysis presented in the previous section cannot be used in this section to assess the occurrence rate of ELF/VLF amplitude saturation onset for each HF beam heading in such a way that the numbers can be meaningfully compared. Instead, we use another observation from Chapter 3 together with the observations presented by *Barr and Stubbe* [1993] in order to analyze the dependence of ELF/VLF amplitude saturation on the location of the ELF/VLF source region.

Observations presented by *Barr and Stubbe* [1993] indicate that HF heating effects can be detected and evaluated in the ELF/VLF frequency range by dividing the harmonic amplitude by the fundamental amplitude. In the case presented by *Barr and Stubbe* [1993], square-wave amplitude modulation was employed, and the ratio of the odd harmonic amplitudes to the first harmonic amplitude was directly examined. However, the odd harmonics needed to be generated at the same frequency as the first harmonic in order to cancel the effects of the Earth-ionosphere waveguide (to a first approximation). This constraint was satisfied, in their case for instance, by

transmitting alternately using a 502 Hz modulation frequency and using a  $502 \times n$  Hz modulation frequency, where  $n$  varied from 2 to 13. As an example, the third harmonic amplitude (of the 502 Hz transmission) at 1506 Hz could then be divided by the first harmonic amplitude from the 1506 Hz transmission in order to obtain the proper ratio. The results indicated that the relative magnitude of the ratios were as expected for the Fourier components of a square-wave modulation scheme and a power-law dependence of ELF/VLF amplitude on HF power. In the case of sinusoidal amplitude modulation, the HF power density varies at both the first and second harmonic of the modulation frequency. We therefore examine the second-to-first harmonic amplitude ratio as a function of ELF/VLF source region location, using ELF/VLF frequencies as close to another as possible in order to best negate the source location-dependent effects of the Earth-ionosphere waveguide.

In the context of the ELF/VLF amplitude saturation onset presented in Chapter 3, we expect that the second-to-first harmonic amplitude ratio decreases as the effects of saturation increase, and we expect that the ratio increases as the effects of saturation decrease. That this is the case can be seen from Figure 3.2: the second harmonic amplitude turns over and may even begin decreasing at high HF power levels, whereas the first harmonic amplitude continues to increase, almost unaffected, at high HF power levels. Therefore, the HF beam heading at which the second-to-first harmonic amplitude ratio is dominant is the HF beam direction in which saturation effects (as observed at the receiver) are minimized. This dominant HF beam heading  $\theta$  may be expressed as:

$$\tan \theta = \frac{\sum_{n=0}^7 R(n) \sin(\frac{\pi}{4}n)}{\sum_{n=0}^7 R(n) \cos(\frac{\pi}{4}n)} \quad (5.1)$$

where  $R(n)$  is the second-to-first harmonic amplitude ratio, as defined above, for an HF beam heading of  $n(\frac{\pi}{4})$  radians, clockwise from North.

In the case of the March and November 2002 campaigns, the requirements for this measurement are only reasonably satisfied for one frequency: 2450 Hz. The second harmonic of the 1225 Hz transmission (2450 Hz) is reasonably close in frequency to the first harmonic transmission at 2375 Hz (within 75 Hz). We therefore make the assumption that the second-to-first harmonic amplitude ratio for transmissions at

2450 Hz (second harmonic of 1225 Hz) and at 2375 Hz effectively negate the source location-dependent differences due to the Earth-ionosphere waveguide. In this section, we only use this ratio to determine whether or not saturation effects increase when the HF beam is directed toward the receiver. The approximation employed should be sufficient for this purpose. Future transmissions directly examining the effects of ionospheric HF heating should use modulation frequencies at exact multiples of the fundamental modulation frequency of interest.

The dominant HF beam directions observed during both the March and November 2002 campaigns are summarized in Figure 5.6. In general, the dominant HF beam direction, as defined above, is directed away from the receiving system, whether that receiver system is located at Chistochina, at Crosswind Lake, or at Valdez. At 3.2/3.25 MHz, the HF beam is wide enough to result in confusing dominant HF beam directions at Chistochina, which is the receiver closest to the HAARP facility. At both Crosswind Lake and at Valdez, however, the 3.2/3.25 MHz beam yields a dominant HF beam direction directed away from each respective receiver. At 5.8 MHz, the results are consistent: all three receivers yield a dominant HF beam direction with the HF beam directed away from each respective receiver. As discussed above, the fact that the dominant HF beam direction is directed away from each receiver indicates that each receiver detects saturation effects to a greater extent when the center of the HF heating beam is closest to the location of the receiver.

The fact that observations at each receiver support the same conclusion indicates that this effect depends on the location of the receiver as well as the location of the ELF/VLF source region. We interpret this result as a dependence of the received ELF/VLF signal on the spatial distribution of the HF-heated region. This effect can be visualized with the help of the cartoon shown in Figure 5.7, where the ELF/VLF signal observed at the receiver is dominated by different parts (saturated and unsaturated) of the HF heated region, depending on the spatial relationship between the ELF/VLF source region and the receiver. When the HF beam is directed away from the receiver, the received ELF/VLF signal is relatively less saturated than when the HF beam is directed toward the receiver, consistent with the conductivity variation in

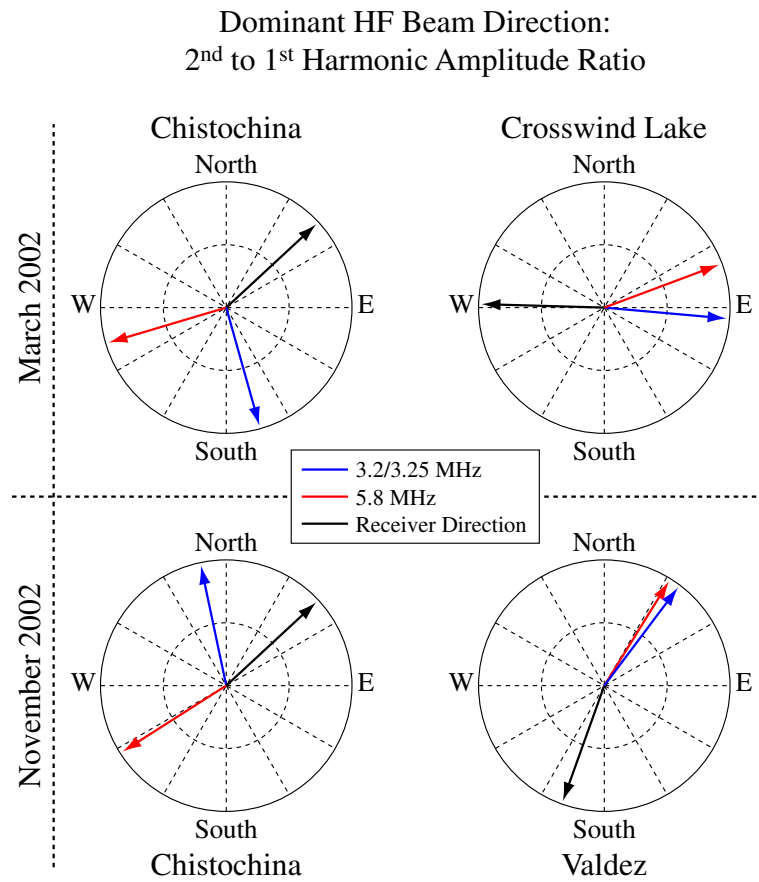


Figure 5.6: Average HF beam directions yielding the dominant second-to-first harmonic amplitude ratio.

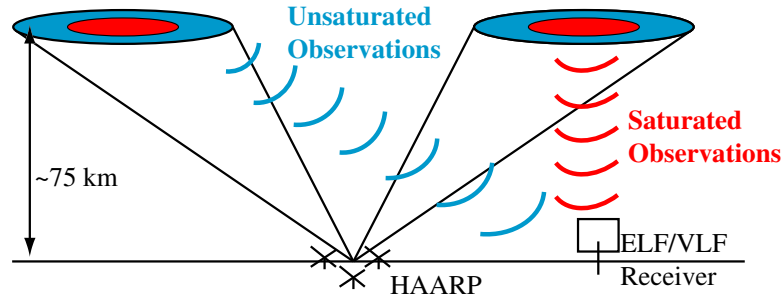


Figure 5.7: A cartoon depicting the dependence of ELF/VLF amplitude saturation observations on the location of the ELF/VLF source region. When the HF beam is directed farther from the receiver, the received amplitude is relatively less saturated than when the HF beam is directed toward the receiver.

the central portion of the HF-heated region being dominated by the nonlinear saturation effects described in Chapter 3. At the same time, our results are consistent with the portions of the HF-heated region farther from the center not being dominated by the saturation process, due primarily to the relatively lower amount of HF energy that reaches these areas. The magnitude of the ELF/VLF wave detected at the receiver depends on the propagation distance between the ELF/VLF source and the receiver. Thus, depending on the location of the ELF/VLF receiver in relation to the center of the HF-heated region, the amplitude of the received ELF/VLF wave may be dominated by either the saturated regions or the unsaturated regions. Varying the location of the HF-heated ionospheric spot in relation to the receivers enables us to detect this spatial dependence on the ELF/VLF amplitude saturation process.

The implication of this result for vertical HF beam orientations is depicted in Figure 5.8. Depending on the location of the ELF/VLF receiver, the conductivity modulation at a radius  $r$  from the center of the HF heating beam dominates the received ELF/VLF signal. This ‘dominant radius’ is necessarily different for receivers located at different distances from the HF-heating facility. Thus, the effects of saturation are best observed at receivers closest to the center of the HF-heating beam. This interpretation is consistent with the observations presented earlier in this chapter, showing that the receiver at Chistochina detected ELF/VLF amplitude saturation

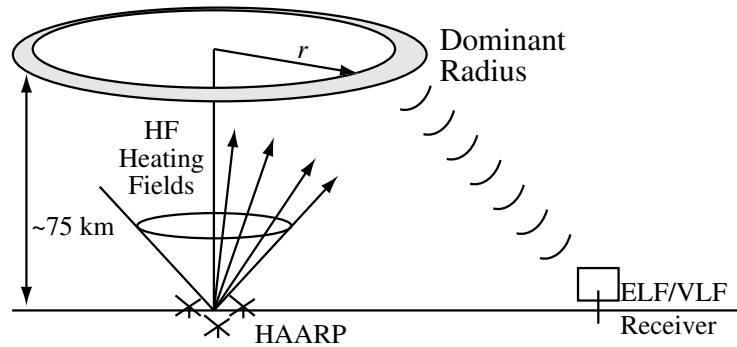


Figure 5.8: Spatial HF heating effects.

more often than the receiver at Crosswind Lake as well as the receiver at Valdez. However, this interpretation does not only affect the analysis of ELF/VLF amplitude observations as a function of distance from HF heating facility. The analysis of ELF/VLF amplitude observations as a function of HF frequency is also affected because the HF beamwidth decreases with increasing frequency. Observations at the same receiver for transmissions using different HF frequencies may thus result in different observed levels of saturation. Under this interpretation, the smaller number of observations of ELF/VLF amplitude saturation at 5.8 MHz versus 3.2/3.25 MHz, presented earlier in this chapter, may simply result from the dependence of the received ELF/VLF signal on the spatial distribution of the source region.

In this chapter, we have used long-term observations of ELF/VLF waves generated using sinusoidal amplitude modulation to show that ELF/VLF amplitude saturation occurs on a regular basis. We have shown strong indications that observations of ELF/VLF amplitude saturation decrease with increasing HF frequency as well as with increasing distance from the center of the HF beam. Lastly, we showed that the ELF/VLF amplitude saturation process results in an ionospheric conductivity modulation with a spatial distribution that is detectable at ground-based ELF/VLF receivers, through the dependence of the ground-based observations on HF beam angle.

# Chapter 6

## Summary and Suggestions for Future Work

### 6.1 Summary of Contributions

In this dissertation, we have addressed the nonlinear generation of ELF/VLF waves by modulated HF heating of the auroral electrojet. All of the results reported herein pertain specifically to the HAARP HF facility operating at its peak radiated power of 960 kW. Using experimental data, we identified an ELF/VLF amplitude saturation effect. A numerical model was employed to show that this ELF/VLF amplitude saturation effect does not result from the nonlinear dependence of conductivity on electron temperature, but instead results from what appears to be a limit on the extent to which the electron temperature may be modulated. At high HF power levels, the saturation effect was shown to be dominantly associated with the vibrational excitation of molecular oxygen through theoretical analysis of the first two harmonic amplitudes. However, the saturation effect on the third harmonic amplitude appears to be dominated by the rotational excitation of molecular nitrogen. We therefore concluded that while the variation of the first and second harmonic amplitudes results from a saturation process, the variation of the third harmonic amplitude results from an imbalance between the heating- and cooling-rates. Nevertheless, the variation of the third harmonic was shown to be directly associated with the onset of the

saturation process. Because this effect does not result from the saturation of the ionospheric conductivity at high HF power levels, modulated HF heating at higher power levels may still effectively generate higher intensity ELF/VLF waves, depending on the dominant electron energy loss rates at the electron temperatures achieved.

In addition to observations of ELF/VLF amplitude saturation onset, we presented observations indicating the existence of an optimal average HF power level maximizing the ELF/VLF amplitude observed at ground-based receivers for modulation depths less than 100%. Using a numerical model, the conductivity modulation at low average HF power levels was shown to be dominated by the HF self-absorption process. The ELF/VLF amplitude thus increases as a result of the increasing rate of absorption at higher electron temperatures. At mid-power ranges, the vibrational excitation of molecular oxygen was shown to become an important factor working against the effectiveness of the Hall conductivity modulation. At high average HF power levels, the rotational excitation of molecular nitrogen and oxygen were shown to become the dominant effects. It is not intuitive that the amplitude variation at high average HF power levels should be dominated by the electron energy loss rate which is dominant primarily at lower HF power levels. This electron energy loss rate dominates the ELF/VLF radiation at the highest HF power levels because it is the dominant factor determining the minimum electron temperature attained during the heating process.

In Chapter 5, long-term observations of ELF/VLF waves generated using sinusoidal amplitude modulation were used to show that ELF/VLF amplitude saturation occurs on a regular basis. Observations of ELF/VLF amplitude saturation were shown to decrease with increasing HF frequency as well as with increasing receiver distance from the center of the HF beam. In addition, the relative harmonic content of the observed ELF/VLF waveform was shown to depend on the direction of the HF beam, or alternatively, on the location of the ELF/VLF source region with respect to the receiver location. Each of these results is consistent with an ELF/VLF amplitude dependence on the spatial distribution of ionospheric conductivity modulation within the HF-heated region. Furthermore, this spatial distribution appears to be detectable using ground-based observations of the horizontal component of the generated ELF/VLF magnetic fields.

## 6.2 Suggestions for Future Research

The theories presented in this dissertation have several implications that may be directly tested by future experiments. In particular, at the time of writing of this chapter, HAARP has just completed an upgrade to full power (3600 kW). The HAARP HF transmitter is now significantly more capable than it was during the experiments presented in this dissertation. In this final section, we describe three experiments that should prove to be enlightening in regard to the nonlinearities reported in this dissertation.

### 6.2.1 Experiment: Same HF Beamwidth, Higher HF Power

We first recommend an extension to higher HF power levels of the HF power-step experiment described in Chapter 3 of this dissertation. Because the spatial distribution of the HF-heated region has been shown (in Chapter 5) to affect observations of the ELF/VLF signals at the receiver, it is important that future experiments capable of reaching higher HF power levels also use approximately the same HF beamwidths for comparison with the result presented in Chapter 3. The newly-upgraded HAARP HF transmitter array is essentially four times the size of the previous array. Although the maximum power density is achieved by fully coupling the entire array, maximizing the power density results in a significant reduction in the HF beamwidth. However, we may also use the HAARP system as if it consisted of four smaller ‘sub-arrays’, each of which would be roughly equivalent to the HAARP HF transmitter array used for this work, and thus has approximately the same beamwidth. We may then aim each of these four sub-arrays overlapping vertically and intersecting at the same point at  $\sim 75$  km altitude. The radiated HF power may then be stepped from minimum to maximum. In this manner, we are able to experimentally extend our ELF/VLF amplitude saturation traces to higher HF power levels, while keeping the HF beamwidth essentially constant.

### 6.2.2 Experiment: Optimal HF Power versus HF Frequency

The new results presented in Chapter 4 indicating an optimal HF power level maximizing the received ELF/VLF amplitude should be explored in greater detail. One way to further explore this phenomenon is to repeat the experiment, as described in Chapter 4, using several different HF frequencies. The rate of HF absorption in the ionosphere directly depends on the HF frequency. Thus, the variation in ELF/VLF amplitude during the lower power HF transmissions, which has been shown in Chapter 4 to be dominated by the HF self-absorption process, may change as a function of HF frequency. The altitude of maximum HF heating also depends on the HF frequency. The electron energy loss rates, which dominate the amplitude variation at high HF power levels, are also altitude-dependent. Therefore, we may expect that the rate of change in ELF/VLF amplitude at both high and low HF power levels will be different as a function of HF frequency. It will be interesting to see whether these two effects result in the same optimal average HF power levels as a function of HF frequency.

### 6.2.3 Experiment: Saturation versus HF Beam Direction

One implication of the work presented in this dissertation is that ground-based ELF/VLF amplitude observations are affected by the spatial distribution of the conductivity modulation within the HF-heated ionospheric region. One way to show that this spatial distribution directly affects ground-based observations is to perform the HF power-step experiment described in Chapter 3, alternately directing the HF beam  $30^\circ$  off-vertical in the direction of the receiver and  $30^\circ$  off-vertical away from the receiver. As the statistical measurements presented in Chapter 5 indicate, we expect the effects of ELF/VLF amplitude saturation to increase when the HF beam is directed toward the receiver. Intermediate off-vertical angles ( $< 30^\circ$ ) may also be used to investigate the extent of the observed amplitude saturation as a function of HF beam angle. Such observations may be used to assess the relative sizes of saturated and unsaturated areas within the HF-heated ionospheric region.

# Bibliography

- Appleton, E. V. (1932), Wireless studies of the ionosphere, *J. Inst. Elec. Engrs.*, *71*, 642–650.
- Balanis, C. A. (1982), *Antenna theory: Analysis and design*. Harper and Row, Publishers, New York, New York.
- Barr, R. (1998), The generation of ELF and VLF radio waves in the ionosphere using powerful HF transmitters, *Adv. Space Res.*, *21*, 677–687.
- Barr, R. and P. Stubbe (1984a), ELF and VLF radiation from the “polar electrojet antenna”, *Radio Sci.*, *19*, 1111–1122.
- Barr, R. and P. Stubbe (1984b), The ‘polar electrojet antenna’ as a source of ELF radiation in the Earth-ionosphere waveguide, *J. Atmos. Terr. Phys.*, *46*, 315–320.
- Barr, R. and P. Stubbe (1991a), ELF radiation from the Tromsø “Super Heater” facility, *Geophys. Res. Lett.*, *18*, 1035–1038.
- Barr, R. and P. Stubbe (1991b), On the ELF generation efficiency of the Tromsø heater facility, *Geophys. Res. Lett.*, *18*, 1971–1974.
- Barr, R. and P. Stubbe (1993), ELF harmonic radiation from the Tromsø heating facility, *Geophys. Res. Lett.*, *20*, 2243–2246.
- Barr, R., M. T. Rietveld, H. Kopka, P. Stubbe, and E. Nielsen (1985), Extra-low-frequency radiation from the polar electrojet antenna, *Nature*, *317*, 155–157.

- Barr, R., P. Stubbe, M. T. Rietveld, and H. Kopka (1986), ELF and VLF signals radiated by the “polar electrojet antenna”: experimental results, *J. Geophys. Res.*, *91*, 4451–4459.
- Barr, R., P. Stubbe, and H. Kopka (1991), Long-range detection of VLF radiation produced by heating the auroral electrojet, *Radio Sci.*, *26*, 871–879.
- Barr, R., P. Stubbe, and M. T. Rietveld (1999), ELF wave generation in the ionosphere using pulse modulated HF heating: initial tests of a technique for increasing ELF wave generation efficiency, *Ann. Geophysicae*, *17*, 759–769.
- Bittencourt, J. A. (1995), *Fundamentals of Plasma Physics*, 676 pp., São José dos Campos, SP., Brazil.
- Budden, K. G. (1965), Effect of electron collisions on the formulas of magneto-ionic theory, *Radio Sci.*, *69D*, 191–211.
- Budden, K. G. (1985), *The Propagation of Radio Waves: The Theory of Radio Waves of Low Power in the Ionosphere and Magnetosphere*, 669 pp., Cambridge University Press, Cambridge and New York.
- Carroll, K. J. (1986), *Theoretical investigation of the coupling and propagation of ionospheric ELF/VLF radiation into the earth-ionosphere waveguide*, Ph.D. thesis, Pennsylvania State University, University Park, Pennsylvania.
- Cotton, P. D. and A. J. Smith (1991), Signature of burst particle precipitation on VLF signals propagating in the Antarctic Earth-ionosphere waveguide, *J. Geophys. Res.*, *96*, 19375–19387.
- Cummer, S. A., T. F. Bell, U. S. Inan, and L. J. Zanetti (1996), VLF remote sensing of the auroral electrojet, *J. Geophys. Res.*, *101*, 5381–5390.
- Ferraro, A. J., H. S. Lee, R. Allshouse, K. Carroll, A. A. Tomko, F. J. Kelly, and R. G. Joiner (1982), VLF/ELF radiation from the ionospheric dynamo current system modulated by powerful HF signals, *J. Atmos. Terr. Phys.*, *44*, 1113–1122.

- Ferraro, A. J., H. S. Lee, R. Allshouse, K. Carroll, R. Lunnen, and T. Collins (1984), Characteristics of ionospheric ELF radiation generated by HF heating, *J. Atmos. Terr. Phys.*, *46*, 855–865.
- Getmantsev, C. G., N. A. Zuikov, D. S. Kotik, L. F. Mironenko, N. A. Mityakov, V. O. Rapoport, Y. A. Sazonov, V. Y. Trakhtengerts, and V. Y. Eidman (1974), Combination frequencies in the interaction between high-power short-wave radiation and ionospheric plasma, *JETP Lett.*, *20*, 101–102.
- Huxley, L. G. H. and J. A. Ratcliffe (1949), A survey of ionospheric cross-modulation, *Proc. Inst. Elec. Eng.*, *96*, 433–440.
- Inan, U. S., M. Golkowski, D. L. Carpenter, N. Reddell, R. C. Moore, T. F. Bell, E. Paschal, P. Kossey, E. Kennedy, and S. Z. Meth (2004), Multi-hop whistler-mode ELF/VLF signals and triggered emissions excited by the HAARP HF heater, *Geophys. Res. Lett.*, *31*, L24805.
- James, H., U. S. Inan, and M. T. Rietveld (1990), Observations on the DE-1 spacecraft of ELF/VLF waves generated by an ionospheric heater, *J. Geophys. Res.*, *95*, 12187–12195.
- James, H. G. (1985), The ELF spectrum of artificially modulated D/E-region conductivity, *J. Atmos. Terr. Phys.*, *47*, 1129–1142.
- James, H. G., R. L. Dowden, M. T. Rietveld, P. Stubbe, and H. Kopka (1984), Simultaneous observations of ELF waves from an artificially modulated auroral electrojet in space and on the ground, *J. Geophys. Res.*, *89*, 1655–1666.
- Kimura, I., A. Wong, B. Chouinard, M. McCarrick, and T. Okada (1991), Satellite and ground observations of HIPAS VLF modulation, *Geophys. Res. Lett.*, *18*, 309–312.
- Kimura, I., P. Stubbe, M. T. Rietveld, R. Barr, K. Ishida, Y. Kasahara, S. Yagitani, and I. Nagano (1994), Collaborative experiments by Akebono satellite, Tromsø ionospheric heater, and European incoherent scatter radar, *Radio Sci.*, *29*, 23–37.

- Lee, H. S., A. J. Ferraro, and J. V. Olson (1990), Detection and characterization of geomagnetic pulsations using HF ionospheric heating, *Radio Sci.*, *25*, 1429–1438.
- Lev-Tov, S. J., U. S. Inan, and T. F. Bell (1995), Altitude profiles of localized *D* region density disturbances produced in lightning-induced electron precipitation events, *J. Geophys. Res. A—Space Physics*, *100*, 21375–21383.
- Li, P. J. and A. J. Ferraro (1990), Determination of *D*-region electron densities from the ELF frequency stepping experiment, *Radio Sci.*, *25*, 1387–1395.
- Maslin, N. M. (1974), Theory of energy flux and polarization changes of a radio wave with two magnetoionic components undergoing self demodulation in the ionosphere, *Royal Society of London Proceedings Series A*, *341*, 361–381.
- McCarrick, M. J., D. D. Sentman, A. Y. Wong, R. F. Wuerker, and B. Chouinard (1990), Excitation of ELF waves in the Schumann resonance range by modulated HF heating of the polar electrojet, *Radio Sci.*, *25*, 1291–1298.
- Mentzoni, M. H. and R. V. Row (1963), Rotational excitation and electron relaxation in nitrogen, *Phys. Rev.*, *130*, 2312–2316.
- Milikh, G. M., K. Papadopoulos, M. McMarrick, and J. Preston (1999), ELF emission generated by the HAARP HF-heater using varying frequency and polarization, *Izvestiya Vysshikh Uchebnykh Zavedenii, Radiofizika*, *42*, 728–735.
- Moore, R. C., C. P. Barrington-Leigh, U. S. Inan, and T. F. Bell (2003), Early/fast VLF events produced by electron density changes associated with sprite halos, *J. Geophys. Res.*, *108*, 1363.
- Moore, R. C., U. S. Inan, and T. F. Bell (2006), Observations of amplitude saturation in ELF/VLF wave generation by modulated HF heating of the auroral electrojet, *Geophys. Res. Lett.*, *33*, L12106, doi:10.1029/2006GL025934.
- Moore, R. C., U. S. Inan, T. F. Bell, and E. J. Kennedy (2007), ELF waves generated by modulated HF heating of the auroral electrojet and observed at a ground distance of ~4400 km, *J. Geophys. Res.*, *In press*.

- Papadopoulos, K., C. L. Chang, P. Vitello, and A. Drobot (1990), On the efficiency of ionospheric ELF generation, *Radio Sci.*, *25*, 1311–1320.
- Papadopoulos, K., T. Wallace, M. McCarrick, G. M. Milikh, and X. Yang (2003), On the efficiency of ELF/VLF generation using HF heating of the auroral electrojet, *Plasma Phys. Rep.*, *29*, 561–565.
- Papadopoulos, K., T. Wallace, G. M. Milikh, W. Peter, and M. McCarrick (2005), The magnetic response of the ionosphere to pulsed HF heating, *Geophys. Res. Lett.*, *32*, L13101.
- Platino, M., U. S. Inan, T. F. Bell, M. Parrot, and E. J. Kennedy (2006), DEMETER observations of ELF waves injected with the HAARP HF transmitter, *Geophys. Res. Lett.*, *33*, L16101.
- Porrat, D., P. R. Bannister, and A. C. Fraser-Smith (2001), Modal phenomena in the natural electromagnetic spectrum below 5 kHz, *Radio Sci.*, *36*, 499–506.
- Ratcliffe, J. A. (1959), *The Magneto-Ionic Theory and its Applications to the Ionosphere*, 206 pp., Cambridge University Press, Cambridge.
- Rietveld, M. T. and P. Stubbe (1987), Ionospheric demodulation of powerful pulsed radio waves - A potential new diagnostic for radars suggested by Tromsø heater results, *Radio Science*, *22*, 1084–1090.
- Rietveld, M. T. and P. Stubbe (2006), Comment on “The magnetic response of the ionosphere to pulsed HF heating” by K. Papadopoulos, T. Wallace, G. M. Milikh, W. Peter, and M. McCarrick, *Geophys. Res. Lett.*, *33*, L07102.
- Rietveld, M. T., H. Kopka, E. Nielsen, P. Stubbe, and R. L. Dowden (1983), Ionospheric electric field pulsations: A comparison between VLF results from an ionospheric heating experiment and STARE, *J. Geophys. Res.*, *88*, 2140–2146.
- Rietveld, M. T., H. Kopka, and P. Stubbe (1986), D-region characteristics deduced from pulsed ionospheric heating under auroral electrojet conditions, *J. Atmos. Terr. Phys.*, *48*, 311–326.

- Rietveld, M. T., P. Stubbe, and H. Kopka (1989), On the frequency dependence of ELF/VLF waves produced by modulated ionospheric heating, *Radio Sci.*, *24*, 270–278.
- Rodriguez, J. V. (1994), *Modification of the Earth's ionosphere by very-low-frequency transmitters*, Ph.D. thesis, Stanford University, Stanford, California.
- Rowland, H., M. J. Keskinen, J. S. Villaseñor, and A. Y. Wong (1996), Observations and simulations of VLF harmonic generation with the high-power auroral simulation array, *J. Geophys. Res.*, *101*, 27027–27033.
- Rowland, H. L. (1999), Simulations of ELF radiation generated by heating the high-latitude D region, *J. Geophys. Res.*, *104*, 4319–4328.
- Sen, H. K. and A. A. Wyller (1960), On the Generalization of the Appleton-Hartree Magnetoionic Formulas, *J. Geophys. Res.*, *65*, 3931–3950.
- Stubbe, P., H. Kopka, and R. L. Dowden (1977), Generation of ELF and VLF waves by polar electrojet modulation: Experimental results, *J. Geophys. Res.*, *86*, 9073–9078.
- Stubbe, P., H. Kopka, M. T. Rietveld, and R. L. Dowden (1982), ELF and VLF generation by modulated HF heating of the current carrying lower ionosphere, *J. Atmos. Terr. Phys.*, *44*, 1123–1135.
- Tomko, A. A. (1981), Nonlinear phenomena arising from radio wave heating of the lower ionosphere, Technical Report PSU-IRL-SCI-470, Ionosphere Research Laboratory, Pennsylvania State University, University Park, Pennsylvania.
- Tomko, A. A., A. J. Ferraro, and H. S. Lee (1980), D region absorption effects during high-power radio wave heating, *Radio Sci.*, *15*, 675–682.
- Tripathi, V.K., C. L. Chang, and K. Papadopoulos (1982), Excitation of the earth-ionosphere waveguide by an ELF source in the ionosphere, *Radio Sci.*, *17*, 1321–1326.

- Villaseñor, J., A. Y. Wong, B. Song, J. Pau, M. McCarrick, and D. Sentman (1996), Comparison of ELF/VLF generation modes in the ionosphere by the HIPAS heater array, *Radio Sci.*, *31*, 211–226.
- Wait, J. R. (1957), The attenuation vs frequency characteristics of VLF radio waves, *Proc, IRE*, *45*, 768–771.
- Willis, J. W. and J. R. Davis (1973), Radio frequency heating effects on electron density in the lower E region, *J. Geophys. Res.*, *78*, 5710–5717.
- Zhou, H. B., K. Papadopoulos, A. S. Sharma, and C. L. Chang (1996), Electromagnetohydrodynamic response of a plasma to an external current pulse, *Physics of Plasmas*, *3*, 1484–1494.